# On a Modification of the Boundary-State Formalism in Off-Shell String Theory¶

## E. T. Akhmedov[1, 2], M. Laidlaw[1], and G. W. Semenoff[1]

[1] *Department of Physics and Astronomy, University of British Columbia, Vancouver, British Columbia, V6T 1Z1 Canada*
[2] *Institute of Theoretical and Experimental Physics, Moscow, 117259 Russia*
Received November 28, 2002

We examine the application of boundary states in computing amplitudes in off-shell open string theory. We find a straightforward generalization of a boundary state which produces the correct matrix elements with on-shell closed string states. © 2003 MAIK "Nauka/Interperiodica".

PACS numbers: 11.25.Uv

**1.** Background independent string field theory [1–5] is an interesting approach to the problem of defining string theory off-shell. It has recently received a lot of attention, particularly as an approach to understanding the properties of unstable D-branes [6–8].

A concrete problem in the study of off-shell string theory in this formalism has been to understand its behavior in the background tachyon field, which is a quadratic function of the coordinates. This gives a tractable model where one can study phenomena such as tachyon condensation and D-brane–anti-D-brane annihilation [6–18]. In this context, the concept of the boundary state, which describes the coupling of string world-sheets to a D-brane, has been used by several authors [19–23].

The boundary-state formalism could be useful in many circumstances: in computing D-brane tensions and cylinder amplitudes, as well as in looking for the gravity counterparts of D-branes [24, 25]. This formalism was originally used to factorize open-string amplitudes in terms of closed-string states. This could be valuable in understanding the relationship between closed and open strings, which is one of the central problems in uncovering the underlying symmetry of string theory. In the operator approach to string-perturbation theory, the boundary state contains the coupling of closed strings to a D-brane.

In this letter, we suggest a generalization of boundary states to be applied to the problem of computing off-shell amplitudes of an open bosonic string. We consider the boundary state for a D-brane with a tachyon condensate and take the special case where the tachyon has a quadratic profile.

Then, we will examine the coupling of massless closed string states to the boundary state. There are two ways of analyzing this coupling. The first uses a sigma-model approach. In that case, we insert the vertex oper-

ator for a graviton into the sigma-model path integral with disc geometry and compute the expectation value. In the second approach, we construct a boundary state for the D-brane with tachyon condensate and consider the inner product of this state with the on-shell closed string graviton. We find that the result does not agree with the sigma-model computation.

We then explain the reason for this disagreement and invent a modified boundary state that has the property that its inner products with all massless closed-string states agree with the amplitudes computed by inserting vertex operators for massless states into the sigma-model path integral.

**2.** First, consider the sigma model, which defines background independent string field theory. We will use the functional integral representation of the partition function of the bosonic string. The world-sheet is the unit disc and the target space is 26-dimensional Euclidean space. The bosonic string action is supplemented by a boundary term that contains the quadratic open-string tachyon background:

$$
Z(g, F, T_0, U) = (2\pi\alpha')^{13}\int \mathcal{D}X e^{-S(X, g, F, T_0, U)}
$$

$$
= (2\pi\alpha')^{13}\int \mathcal{D}X
$$

$$
\times \exp\left\{-\frac{1}{2}\int_D d^2\sigma\, g_{\mu\nu}\partial^a X^\mu(\sigma)\partial^a X^\nu(\sigma)\right. \tag{1}
$$

$$
-\oint_{\partial D} d\theta\left(\pi\alpha' F_{\mu\nu}X^\mu(\theta)\partial_\theta X^\nu(\theta)\right.
$$

$$
\left.\left. +\frac{1}{2\pi}T_0 + \frac{\alpha'}{4}U_{\mu\nu}X^\mu(\theta)X^\nu(\theta)\right)\right\}.
$$

---

¶ This article was submitted by the authors in English.

Here, $\alpha'$ is the inverse string tension. The world-sheet is a disc, $D$, for which we use complex coordinates $z = e^{-\sigma_1 - i\sigma_2}$ with $0 < \sigma_1 < \infty$, and $0 \le \sigma_2 \le 2\pi$ is the parameterization of the disc $D$ (or of the infinitely long half-cylinder). We also sometimes use the coordinate $z = \rho e^{-i\theta}$. $0 \le \theta \le 2\pi$ is the parameterization of the boundary of the disc $\partial D$. $X^\mu(\sigma)$, $\mu = 1, \ldots, 26$ are maps of the string onto the target space with the constant metric $g_{\mu\nu}$, $T(X) = T_0 + \dfrac{\pi\alpha'}{2} U_{\mu\nu} X^\mu X^\nu$ is the tachyon profile with constant $T_0$ and constant matrix $U_{\mu\nu}$ of some rank, and $F_{\mu\nu}$ is constant gauge field strength. This functional integral is taken with boundary conditions

$$g_{\mu\nu}\partial_n X^\nu(\theta) + 2\pi\alpha' F_{\mu\nu}\partial_t X^\nu(\theta) + \frac{\alpha'}{2} U_{\mu\nu} X^\nu(\theta) = 0, \quad (2)$$

where $\partial_n$ and $\partial_t$ are the normal and tangential derivatives to the boundary $\partial D$. We use a nonstandard normalization of $X$ as in [26]. It is related to the standard one via the rescaling by $\sqrt{2\pi\alpha'}$.

The theory (1) is not conformally invariant and represents a special example of the background independent string field theory [1–4]. Because of the conformal anomaly, this theory explicitly depends on the conformal factor of the world-sheet metric. The convention is to consider the theory on the unit disc with flat metric. The main advantage of the case of (1) is that the theory is gaussian and therefore is exactly solvable [1–3, 8–10]. For example, the renormalization group flow of the parameters $U_{\mu\nu}$ in the functional integral (1) describes the annihilation of a D25-brane in bosonic string theory [8]. If the rank of the initial matrix $U_{\mu\nu}$ is $26 - p$, what is left after the annihilation of the D25-brane is a D$p$-brane. This arises from the fact that the $\beta$ function for $U$ is $\beta_U = -U$, and, hence, $U$ goes to zero in the ultraviolet and to infinity in the infrared limits. Thus, we see from (2) that (if $F = 0$) the Neumann boundary conditions present in the UV limit, where $U \sim 0$, evolve to Dirichlet boundary conditions in $26 - p$ coordinates, with the rest of the coordinates still obeying Newman boundary conditions. These final boundary conditions describe a D$p$-brane.

The functional integral (1) is readily computed [1–3]:

$$Z(g, F, T_0, U) = (2\pi\alpha')^{13} e^{-T_0}$$

$$\times \prod_{m=1}^{\infty} \frac{1}{\det\left(g + 2\pi\alpha' F + \dfrac{\alpha'}{2}\dfrac{U}{m}\right)}$$

$$\times \int dx_0 e^{-\pi\alpha' \frac{U_{\mu\nu}}{2} x_0^\mu x_0^\nu} = (2\pi\alpha')^{13} \frac{1}{\sqrt{\pi\alpha'\det(U)}} e^{-T_0} \quad (3)$$

$$\times \prod_{m=1}^{\infty} \frac{1}{\det\left(g + 2\pi\alpha' F + \dfrac{\alpha'}{2}\dfrac{U}{m}\right)},$$

where $x_0$ is the zero mode of $X$ and the determinant is taken over the $\mu$ and $\nu$ indexes.

The expression (3) is divergent. Using $\zeta$-function regularization [11], one finds

$$Z(g, F, T_0, U) \propto e^{-T_0} \sqrt{\det\left(\frac{g + 2\pi\alpha' F}{\pi\alpha' U}\right)}$$

$$\times \det\Gamma\left(1 + \frac{\alpha' U/2}{g + 2\pi\alpha' F}\right), \quad (4)$$

where $\Gamma(g)$ is the $\Gamma$ function. The dependence of the transcendental functions on the matrix $U$ is assumed to be defined by their Taylor expansion. The divergence in (4) as $U \longrightarrow 0$ is due to the infinite volume of the D-brane (and becomes a volume factor in that limit).

We would like to consider interactions of the D25-brane (1) with massless closed-string fields. For example, the D25-brane tension can be extracted from the expectation value of the graviton vertex operator. Consider the correlator

$$\left\langle \int_D d^2\sigma\, h_{\mu\nu}\partial^a X^\mu(\sigma)\partial^a X^\nu(\sigma) \right\rangle_{F, T_0, U}, \quad (5)$$

where the averaging is taken in the functional integral (1). $h_{\mu\nu}$ is a constant traceless matrix that defines the polarization of the graviton, and we could consider in exactly the same manner correlators corresponding to the antisymmetric tensor field $B$ or to the dilaton.

It is easy to see that (5) is given by

$$\left\langle \int_D d^2\sigma\, h_{\mu\nu}\partial^a X^\mu(\sigma)\partial^a X^\nu(\sigma) \right\rangle_{F, T_0, U}$$

$$= h_{\mu\nu}\left(\frac{\delta Z(g + h', F, T_0, U)}{\partial h'_{\mu\nu}}\right)_{h'=0} \quad (6)$$

$$= -Z(g, F, T_0, U) \sum_{m=1}^{\infty} \mathrm{Tr}\left[\frac{h}{g + 2\pi\alpha' F + \dfrac{\alpha'}{2}\dfrac{U}{m}}\right],$$

where the trace is taken over the $\mu$ and $\nu$ indices.

**3.** We can compare this computation with a naive application of the boundary-state formalism.

The boundary state $|B\rangle$ is a quantum state of closed-string theory that obeys boundary condition (2):

$$\left( g_{\mu\nu}\partial_n \hat{X}^\nu(\theta) + 2\pi\alpha' F_{\mu\nu}\partial_\theta X^\nu(\theta) \right.$$
$$\left. + \frac{\alpha'}{2}U_{\mu\nu}\hat{X}^\nu(\theta) \right)|B\rangle = 0, \qquad (7)$$

where $\hat{X}(\theta)$ is the operator corresponding to the boundary value of the map $X$ with the following closed-string mode expansion:

$$\hat{X}^\mu(z, \bar{z}) = x_0^\mu + p^\mu \log z + \sum_{n \neq 0}\left[ \frac{\alpha_n^\mu}{n}z^n + \frac{\tilde{\alpha}_n^\mu}{n}\bar{z}^n \right]. \qquad (8)$$

In this formula, $z = e^{-\sigma_1 - i\sigma_2} = \rho e^{-i\theta}$, $0 \leq \rho \leq 1$ is the complex coordinate on the disc, $x_0$ and $p$ are the coordinate and momentum of the string center of mass, the sum runs over $n$ from minus infinity to plus infinity except zero, and the generators $\alpha$ and $\tilde{\alpha}$ obey certain conditions to make $\hat{X}$ hermitian, as well as the standard commutation relations (see, e.g., [24, 25]).

The solution to (7) is

$$|B\rangle = \mathcal{N}$$

$$\times \prod_{n \geq 1}\exp\left\{ -\left[ \frac{g - 2\pi\alpha' F - \frac{\alpha'}{2}\frac{U}{n}}{g + 2\pi\alpha' F + \frac{\alpha'}{2}\frac{U}{n}} \right]_{\mu\nu} \frac{\alpha_{-n}^\mu \tilde{\alpha}_{-n}^\nu}{n} \right\}|0\rangle, \qquad (9)$$

where $|0\rangle$ is the vacuum state, which is annihilated by all creation operators $\alpha_n$ and $\tilde{\alpha}_n$ with $n > 0$, and $\mathcal{N}$ is a normalization constant.

The normalization is fixed by considering the coupling of the off-shell (momentum zero) closed-string tachyon whose coupling to the boundary state should be equal to a trivial perturbation of the sigma model partition function,

$$\mathcal{N} = \langle 0|B\rangle = Z(g, F, T_0, U). \qquad (10)$$

Now we would like to find (along the lines of [24, 25]) the reaction of the background closed-string fields on the state $|B\rangle$. For this, we consider the correlator

$$\langle h|B\rangle = \langle 0|\alpha_1^\mu \tilde{\alpha}_1^\nu h_{\mu\nu}|B\rangle, \qquad (11)$$

which should be compared with the correlator (5). However, we obtain

$$\langle h|B\rangle = -Z(g, F, T_0, U)$$

$$\times \left[ \frac{g - 2\pi\alpha' F - \frac{\alpha'}{2}U}{g + 2\pi\alpha' F + \frac{\alpha'}{2}U} \right]^{\mu\nu} h_{\mu\nu} \qquad (12)$$

$$= -2Z(g, F, T_0, U)\mathrm{Tr}\left[ \frac{h}{g + 2\pi\alpha' F + \frac{\alpha'}{2}U} \right],$$

where at the last step we used the fact that $h$ is traceless.

The formula (6) clearly does not agree with (12). Note that they would agree if $U = 0, \infty$ [24, 25]. In fact, these two expressions agree up to a (infinite) normalization factor at the fixed points of the renormalization group flow, $U \longrightarrow 0$ and $U \longrightarrow \infty$. As we will see below, the infinite factor will turn out to be the volume of the noncompact group PSL(2, R) [27].

**4.** The apparent paradox that we have arrived at should not be surprising. The application of the boundary-state formalism to the computation of the expectation value of a closed-string vertex operator in open-string theory requires a conformal mapping of the punctured disc, which is the world-sheet of open strings, to the semi-infinite cylinder, which is the world-sheet of closed strings. In the conformally non-invariant theory that we are considering here, it is natural to expect that this mapping is blocked by the conformal anomaly.

The global conformal group of the disc is PSL(2, R).[1] If the PSL(2, R) symmetry were *not* broken, it would be possible to use it to fix the position at one point on the disc and one point on its boundary (or three points on the boundary). This could be used to get rid of integration over $\sigma$ in (5). This means that

$$\left\langle \int_D d^2\sigma\, h_{\mu\nu}\partial^a X^\mu(\sigma)\partial^a X^\nu(\sigma) \right\rangle_{F, T_0, U = 0} \qquad (13)$$

$$= \pi\langle h_{\mu\nu}\partial^a X^\mu(\sigma')\partial^a X^\nu(\sigma')\rangle_{F, T_0, U = 0}.$$

Here, $\sigma'$ is some particular point on the disc, say 0. We expect that this will occur when $U = 0$ or $U = \infty$. However, since the conformal symmetry is broken when $U$ does not have these values, the matrix element depends on the position, and the integration is important.

The conformal mapping of a point $z$ on the disc to a point $\eta$ in the cylinder is $z = e^{-\eta}$. In this mapping, the center of the disc, at point $z = 0$, is mapped to the cap of the cylinder at infinity, $\mathrm{Re}\,\eta = \infty$. In the boundary-state computation that leads to (11), it is assumed that the boundary state is at one cap of the cylinder, where $\mathrm{Re}\,\eta = 0$, and the graviton $|h\rangle$ is at the other cap, which

---

[1]The relevance of PSL(2, R) in a similar context was previously noticed in [4, 12].

is located at $\mathrm{Re}\,\eta = \infty$, which is the image of the center of the disc. For this reason, we expect the boundary-state computation to produce the expectation value of the graviton vertex operator inserted at the center of the disc.

In the sigma model, it is straightforward to compute the correlator

$$\langle h_{\mu\nu}\partial^a X^\mu \partial^a X^\nu(\rho, \theta)\rangle_{F, T_0, U} \tag{14}$$

by summing the perturbation expansion for $U$, similar to computations in [26, 28]. In the course of the calculation, we use the boundary-to-disc propagator with Neuman boundary conditions:

$$G(\rho e^{i\theta}, e^{i\theta'}) = \frac{1}{\pi}\sum_{m=1}^{\infty}\frac{\rho^m}{m}\cos[m(\theta - \theta')], \tag{15}$$

which also gives the boundary-to-boundary propagator in the limit $\rho \longrightarrow 1$. Explicitly, the contribution to the correlator from $n$ interactions with the background $U$ is

$$Z(g, F, T_0, U)\mathrm{Tr}\left(\frac{-\alpha' U}{2}\right)^n$$

$$\times \frac{1}{\pi^n}\int d\phi_1\dots d\phi_n\left(\partial_\rho\hat{\rho} + \frac{1}{\rho}\partial_\phi\hat{\phi}\right)$$

$$\times \sum_{m=1}^{\infty}\frac{\rho^m\cos[m(\phi - \phi_1)]}{m} \tag{16}$$

$$\times \sum_{m_1=1}^{\infty}\frac{\cos[m_1(\phi_1 - \phi_2)]}{m_1}\dots\left(\partial_\rho\hat{\rho} + \frac{1}{\rho}\partial_\phi\hat{\phi}\right)$$

$$\times \sum_{m_n=1}^{\infty}\frac{\rho^{m_n}\cos[m_n(\phi_n - \phi)]}{m_n}.$$

The above integral is trivial, and, upon summation over all values of $n$ and inclusion of the antisymmetric field $F$, the result is

$$\langle h_{\mu\nu}\partial^a X^\mu \partial^a X^\nu(\rho, \theta)\rangle_{F, T_0, U} = -2Z(g, F, T_0, U)$$

$$\times \sum_{m=1}^{\infty} m\mathrm{Tr}\left(\frac{h}{g + 2\pi\alpha' F + \frac{\alpha' U}{2\ m}}\right)\rho^{2(m-1)}. \tag{17}$$

Now it is easy to see that to obtain (6) one has to integrate this expression with the measure $\int \rho\, d\rho\, d\theta$, while to obtain (12) it is necessary to put $\rho = 0$: only the $m = 1$ term survives in this case. This is in agreement with our expectation that the boundary state describes the matrix element only when the operator is inserted at the center of the disc.

**5.** With the above choice of coordinates on the disc, there is a subset of the full conformal group of the plane that preserves the position and shape of the boundary of the disc. This subset is a $PSL(2, R)$ subgroup of the full conformal group. It acts on the complex coordinates of the disc as

$$z \longrightarrow w(z) = \frac{az + b}{b^*z + a^*}, \tag{18}$$

where

$$|a|^2 - |b|^2 = 1. \tag{19}$$

It is easy to verify that the unit circle is mapped onto itself. Thus, this mapping preserves the boundary of the disc. The origin is mapped to the point $b/a^* = \rho e^{-i\theta}$ in the interior of the disc.

We will examine how the boundary state $|B\rangle$ behaves under this transformation.

The boundary state is created by the exponential of the operator

$$\mathfrak{B} = \sum_{n=1}^{\infty} S_{\mu\nu}(n)\alpha^\mu_{-n}\tilde{\alpha}^\nu_{-n},$$

$$\text{and} \quad S_{\mu\nu}(n) = \frac{1}{n}\left[\frac{g - 2\pi\alpha' F - U/n}{g + 2\pi\alpha' F + U/n}\right]_{\mu\nu}, \tag{20}$$

where $\alpha^\mu_n$ and $\tilde{\alpha}^\mu_n$ are closed-string oscillators. It is useful to write this operator in terms of position variables. For this, we introduce the two fields

$$A^\mu(z) = \sum_{n\neq 0}\frac{\alpha^\mu_{-n}}{n}z^n, \tag{21}$$

$$\tilde{A}^\mu(\bar{z}) = \sum_{n\neq 0}\frac{\tilde{\alpha}^\mu_{-n}}{n}\bar{z}^n. \tag{22}$$

Here, $z$ are complex coordinates on the disc and $\eta = -\ln z$ are coordinates on a cylinder.

Then (20) can be written in the form

$$\mathfrak{B} = \oint\frac{dz}{2\pi i}\oint\frac{d\bar{z}}{-2\pi i}S_{\mu\nu}(z, \bar{z})A^\mu(z)\tilde{A}^\nu(\bar{z}), \tag{23}$$

where the integrations are on the unit circle and the kernel is defined by the power series

$$S_{\mu\nu}(z, \bar{z}) = \sum_{p=1}^{\infty} S_{\mu\nu}(p)p^2(z\bar{z})^{p-1}. \tag{24}$$

Now we take into account that, under a general coordinate transformation, the coordinate functions $A^\mu(z)$ and $\tilde{A}(z)$ transform as

$$A'^\mu(z') = A^\mu(z), \quad \tilde{A}'^\mu(\bar{z}') = \tilde{A}^\mu(\bar{z}). \tag{25}$$

If we apply this equation to the conformal transformation and change variables in the integral, we obtain the

transformed boundary operator

$$\mathcal{B}(a, b) = \oint \frac{dz}{2\pi i} \oint \frac{d\bar{z}}{-2\pi i} S_{\mu\nu}(z, \bar{z}|a, b) A^{\mu}(z) \tilde{A}^{\nu}(\bar{z}), \quad (26)$$

where

$$S_{\mu\nu}(z, \bar{z}|a, b) = \left|\frac{dw}{dz}\right|^2 S_{\mu\nu}(w(z), \overline{w}(\bar{z})). \quad (27)$$

As an exercise, we can verify that the usual, conformally invariant boundary state is independent of the PSL(2, $R$) coordinates ($a, b$). In that case (for simplicity, we put here $F = 0$),

$$S^0_{\mu\nu}(p) = \delta_{\mu\nu}/p \quad (28)$$

and

$$S^0_{\mu\nu}(z, \bar{z}) = \delta_{\mu\nu}/(1 - z\bar{z})^2,$$

$$S^0_{\mu\nu}(z, \bar{z}|a, b) \quad (29)$$

$$= \delta_{\mu\nu} \left|\frac{dw(z)}{dz}\right|^2 \frac{\delta_{\mu\nu}}{(1 - w(z)\overline{w}(\bar{z}))^2} = \frac{\delta_{\mu\nu}}{(1 - z\bar{z})^2}.$$

This is independent of $a$ and $b$, which is the desired result.

Then the PSL(2, $R$) transformed boundary state is created by the exponential of the operator $\mathcal{B}(a, b)$. In terms of oscillators, this operator has the form

$$\mathcal{B}(a, b) = \sum_{m, n > 0} S_{\mu\nu}(m, n|a, b) \alpha^{\mu}_{-m} \tilde{\alpha}^{\nu}_{-n}. \quad (30)$$

(We will verify that it still contains only negative index oscillators.) The moments are defined by

$$S_{\mu\nu}(m, n|a, b) = \sum_{p = 1}^{\infty} \frac{p}{m} \frac{p}{n} S_{\mu\nu}(p) \oint \frac{dz}{2\pi i} z^{p-1}$$

$$\times \left(\frac{b^*z + a^*}{az + b}\right)^m \oint \frac{d\bar{z}}{-2\pi i} \bar{z}^{p-1} \left(\frac{b\bar{z} + a}{a^*\bar{z} + b^*}\right)^n. \quad (31)$$

Since $|a|/|b| > 1$, the contour integrals on the right-hand side of (31) have poles inside the unit circle only when $m, n > 0$. Therefore, they are nonzero only when $m > 0$ and $n > 0$, as anticipated in (30). It is straightforward to evaluate the integrals in (31). For example, in the case that we will shortly see is relevant to massless closed-string states,

$$S_{\mu\nu}(1, 1|a, b) = \frac{1}{|a|^2} \sum_{p = 1}^{\infty} \left|\frac{b}{a}\right|^{2p-2} p^2 S_{\mu\nu}(p). \quad (32)$$

We can see from the form of the transformation in (31) that the boundary states generally depend on all three parameters of PSL(2, $R$). In some special cases, (32) for example, it depends on fewer parameters, such as $|b/a^*| = \rho$. The matrix element of any massless closed-string state with the boundary state will depend on the

PSL(2, $R$) parameters only through this dependence on the coordinate.

Note that the matrix element $\langle 0|B \rangle$ does not change under the transformation (18); i.e., Eq. (10) is legitimate. However, the correlator $\langle h|B \rangle$ transforms according to (32) as

$$\langle h|B_{\rho} \rangle = \langle 0|h_{\mu\nu} \alpha^{\mu}_1 \tilde{\alpha}^{\nu}_1 Z(g, F, T_0, U)$$

$$\times \exp\left\{-\sum_{m > 0} \frac{1}{m} \left[\frac{g - 2\pi\alpha'F - \frac{\alpha'U}{2m}}{g + 2\pi\alpha'F + \frac{\alpha'U}{2m}}\right]_{\mu\nu}\right.$$

$$\times m^2(1 - \rho^2)^2(-\rho)^{2(m-1)} \alpha^{\mu}_{-1} \tilde{\alpha}^{\nu}_{-1} + \dots \left.\right\}|0\rangle \quad (33)$$

$$= -2Z(g, F, T_0, U)$$

$$\times \sum_m m \text{Tr}\left[\frac{h}{g + 2\pi\alpha'F + \frac{\alpha'U}{2m}}\right] \rho^{2(m-1)}(1 - \rho^2)^2.$$

It is worth mentioning here that if $U \longrightarrow 0$ then

$$\sum_{m > 0} m\rho^{2(m-1)} = \frac{1}{(1 - \rho^2)^2}$$

exactly cancels $(1 - \rho^2)^2$ in the numerator, and, hence, (6) agrees with (12) and (33).

At the same time, the Haar measure on the PSL(2, $R$) group is given by

$$\int d^2a d^2b \delta(|a|^2 - |b|^2 - 1) f$$

$$= \int d^2a d^2b \delta(|a|^2 - |b|^2 - 1) \quad (34)$$

$$\times \int d\rho \delta\left(\left|\frac{b}{a}\right| - \rho\right) f = 2\pi^2 \int \frac{\rho d\rho}{(1 - \rho^2)^2} f,$$

which is valid if the function $f$ within the integral depends only on $\rho$. Combining formulas (33) and (34), we find exact agreement.

In conclusion, we conjecture that the average over PSL(2, $R$) of the transformed boundary state,

$$|\hat{B}\rangle = \int d^2a d^2b \delta(|a|^2 - |b|^2 - 1)|B_{a, b}\rangle, \quad (35)$$

will have the correct overlap with any on-shell closed-string state. Here, we have checked this for the closed-string tachyon and the graviton, and it is straightforward to check it for the antisymmetric tensor, which has a nonzero expectation value when a background gauge field is turned on. It would be interesting to check this hypothesis for higher order correlation functions. The

generalization of our results to the superstring boundary states with linear tachyon profile is straightforward.

## REFERENCES

1. E. Witten, Phys. Rev. D **46**, 5467 (1992); hep-th/9208027.
2. E. Witten, Phys. Rev. D **47**, 3405 (1993); hep-th/9210065.
3. E. Witten, hep-th/9306122.
4. S. L. Shatashvili, Phys. Lett. B **311**, 83 (1993); hep-th/9303143.
5. S. L. Shatashvili, hep-th/9311177.
6. A. A. Gerasimov and S. L. Shatashvili, J. High Energy Phys. **0010**, 034 (2000); hep-th/0009103.
7. A. A. Gerasimov and S. L. Shatashvili, J. High Energy Phys. **0101**, 019 (2001); hep-th/0011009.
8. D. Kutasov, M. Marino, and G. Moore, J. High Energy Phys. **0010**, 045 (2000); hep-th/0009148.
9. E. T. Akhmedov, A. A. Gerasimov, and S. L. Shatashvili, hep-th/0105228.
10. A. A. Gerasimov and S. L. Shatashvili, hep-th/0105245.
11. P. Kraus and F. Larsen, Phys. Rev. D **63**, 106004 (2001); hep-th/0012198.
12. B. Craps, P. Kraus, and F. Larsen, hep-th/0105227.
13. K. S. Viswanathan and Y. Yang, hep-th/0104099.
14. R. Rashkov, K. S. Viswanathan, and Y. Yang, hep-th/0101207.
15. M. Alishahiha, hep-th/0104164.
16. O. Andreev, Nucl. Phys. B **598**, 151 (2001); hep-th/0010218.
17. T. Takayanagi, S. Terashima, and T. Uesugi, J. High Energy Phys. **0103**, 014 (2001); hep-th/0012210.
18. G. Arutyunov, A. Pankiewicz, and B. Stefanski, hep-th/0105238.
19. S. P. de Alwis, Phys. Lett. B **505**, 215 (2001); hep-th/0101200.
20. K. Bardakci and A. Konechny, hep-th/0105098.
21. T. Lee, hep-th/0105264.
22. T. Lee, hep-th/0105115.
23. A. Fujii and H. Itoyama, hep-th/0105247.
24. P. Di Vecchia and A. Liccardo, hep-th/9912275.
25. P. Di Vecchia and A. Liccardo, hep-th/9912161.
26. E. S. Fradkin and A. A. Tseytlin, Phys. Lett. B **163B**, 123 (1985).
27. J. Liu and J. Polchinski, Phys. Lett. B **203**, 39 (1988).
28. M. Laidlaw, J. High Energy Phys. **0103**, 004 (2001); hep-th/0009068.

# Molecular Effect in the Formation of the Energy Spectrum upon the Transmission of Low-Energy Hydrogen Ions through Ultrathin Carbon Foils

### E. A. Gridneva, V. A. Kurnaev, N. N. Trifonov, and S. K. Zhdanov

*Moscow Engineering Physics Institute (State University), Moscow, 115409 Russia*
*e-mail: helen@plasma.mephi.ru*
Received November 26, 2002

The energy spectra of ions transmitted through ultrathin diamond-like foils irradiated by $H^+$, $H_2^+$, and $H_3^+$ ions with energies from 2 to 12 keV/nucleon are studied. For molecular ions incident on the target with identical velocities, a considerable broadening of the energy spectrum is observed with an increase in the ion mass. The spectrum halfwidth reduced to the identical particle velocity remains constant for each type of incident ion, irrespective of the foil thickness. © *2003 MAIK "Nauka/Interperiodica"*.

PACS numbers: 34.50.Dy

In the last few years, the effects accompanying the interaction of molecular ions and clusters with matter have become one of the hottest areas of research in the field of atomic collisions in solids [1]. The reason is that such effects offer a better insight into the mechanisms of interaction between the aforementioned types of particles and matter. In addition to the radiation effects that occur in matter and are nonadditive with respect to the number of atoms in a molecular ion, the vicinage effect, the wake effect, the charge state of particles scattered in matter, and other effects are intensively studied. In the case of the transmission of molecular ions (especially of the simplest of them $H_2^+$) through thin layers of matter [2–5], the comparison of experimental data with model considerations is most simple. For energies corresponding to particle velocities higher than the Bohr velocity, the effect of initial interatomic distance in the incident cluster on the energy spectra and other parameters of the transmitted particle flux was given an adequate theoretical interpretation [3]. However, in the low-energy region, as far as we know, such investigations have not been carried out.

This paper presents the study of the effect of the number of atoms in molecular hydrogen ions on the specific energy loss and the width of the energy spectrum upon the irradiation of thin foil targets by particles with energies on the order of several keV per nucleon.

Measurements were made on the "Big Mass Monochromator" of the Moscow Engineering Physics Institute [6]. The system provided an angular beam divergence of less than 0.4° and an energy homogeneity within 0.003. After the transmission through foils, the ion energies were analyzed by an automated energy analyzer with the aperture $\Delta\phi_0 = 1.5°$ and an energy resolution of 0.005. The pressure in the chamber during the experiment was $10^{-7}$ torr. Other measurement conditions were the same as described in [7].

The targets were carbon foils with the rated thickness values $L \approx 25$, 40, and 70 Å and a density of $2 \pm 0.2$ g/cm³.

The foils were irradiated by $H^+$, $H_2^+$, and $H_3^+$ ions with energies from 2 to 12 keV per nucleon. After their interaction with the foils, only protons arising from the dissociation of the initial ions were observed, while the latter lost part of their energy in the target material. The positions of spectral maxima of the transmitted particles coincide for the different molecular ions with equal initial velocities per nucleon (Fig. 1). This suggests that the energy loss is the same for different molecular ions. Within the experimental accuracy, the measured velocity dependence of the most probable energy $E_m$ of exit particles is linear for different foils.

From the dependence of the spectrum width $\Delta E_{1/2}$ on the initial velocity ($E_0^{1/2}$), one can see (Fig. 2) that, for different ions with equal initial velocities, the energy spectrum broadens as the number of atoms in the ion increases, and the velocity dependence of the spectrum width is approximately linear. The spectrum for the two- and three-atomic molecular ions broadens in both high- and low-energy directions, without any significant asymmetry.

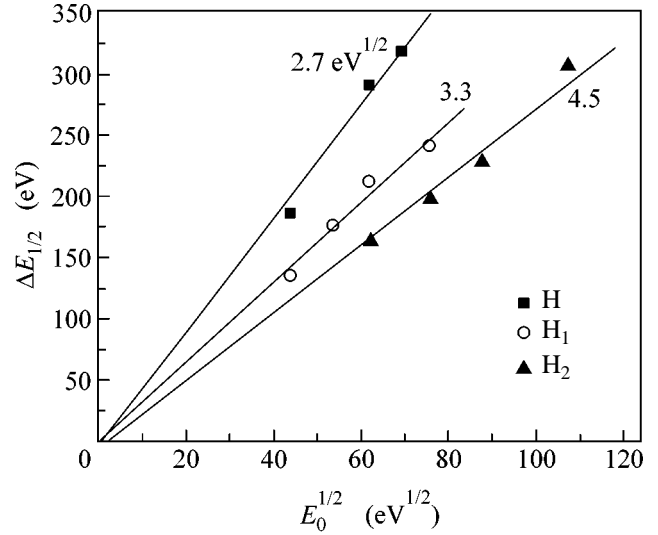As was shown in [7], in the given hydrogen energy range, the peak halfwidth observed for the protons
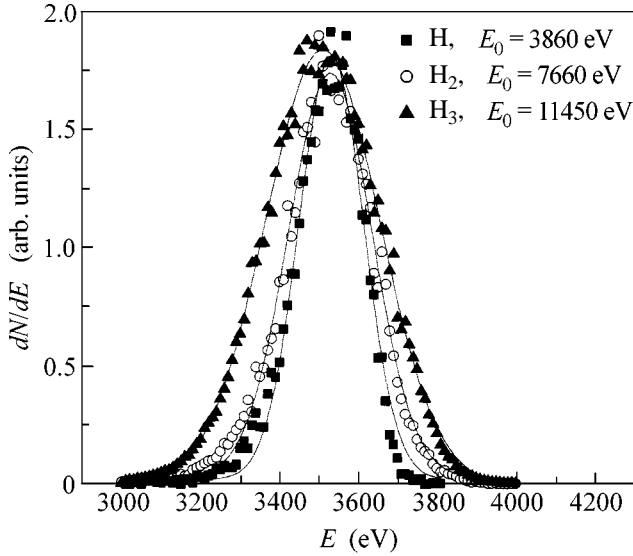
**Fig. 1.** Energy spectra of different molecular hydrogen ions with equal energies per nucleon.



**Fig. 2.** Halfwidths of energy spectra for a diamond-like foil with $L = 25$ Å versus the initial velocity of the incident particles (per nucleon). The values of $\Delta E_{1/2}/E_0^{1/2}$ are indicated near the curves.

detected in the incident beam direction ($\theta = 0$) can be expressed as

$$\Delta E_{1/2} \cong 2\sqrt{2\ln 2}\,\sqrt{E_0}\,kL\left\{\left(\frac{\Delta L}{L}\right)^2 + \frac{\overline{\varepsilon^2}(E_0)}{(\bar{\varepsilon}(E_0))^2}\frac{1}{L}\right\}^{1/2},$$

where $\Delta L$ is the fluctuation of foil thickness, $k$ is the proportionality coefficient characterizing the energy dependence of stopping power, and the last term in the braces determines the relative energy-loss fluctuations due to inelastic collisions. According to [8], the relative energy-loss fluctuation in the inelastic collisions depends neither on thickness nor on energy but only on the material. Therefore, for each of the foils under study, the quantity $\Delta E_{1/2}/\sqrt{E_0}$ must not depend on energy, which is confirmed by the experiment: within the experimental accuracy (~0.05), this ratio is constant for any of the foils. As an example, Fig. 3 shows the values of $\Delta E_{1/2}/\sqrt{E_0}$ that were determined from the spectra measured with a 25-Å-thick foil for atomic and molecular ions with different energies. One can see that $\Delta E_{1/2}/\sqrt{E_0} = \text{const}$ for each type of ion.

If we represent the halfwidth of energy spectrum in the form $\Delta E_{1/2}^* \sim \sqrt{E_0}\{\Delta E_{1/2}^2 + \Delta E_{\mathrm{mol}}^2\}^{1/2}$, where $\Delta E_{1/2}$ is the aforementioned energy spectrum halfwidth (mainly caused by the fluctuation of foil thickness) of the protons transmitted through the foil and $\Delta E_{\mathrm{mol}}$ is the contribution from the molecular effect, we find that the ratio $\Delta E_{\mathrm{mol}}/\sqrt{E}$ is constant. From the comparison

of the spectra obtained for $H^+$ and $H_2^+$, we find $\Delta E_{\mathrm{mol}}/\sqrt{E} = 2.1 \pm 0.3$ eV$^{1/2}$ for all foils under study in the energy range 2–10 keV/nucleon. The comparison of the spectra from the $H^+$ and $H_3^+$ ions for the foil with $L = 25$ Å yields the value $\Delta E_{\mathrm{mol}}/\sqrt{E} = 3.6 \pm 0.3$ eV$^{1/2}$.
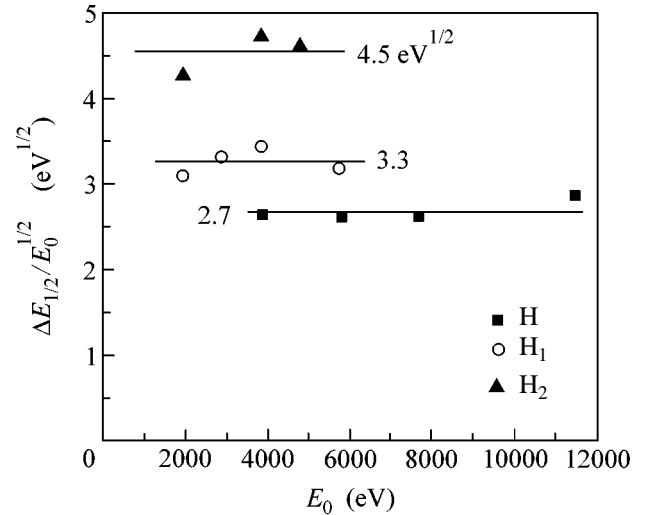


**Fig. 3.** The values of $\Delta E_{1/2}/E_0^{1/2}$ versus the initial energy of incident particles per nucleon for a diamond-like foil with $L = 25$ Å. The values of $\Delta E_{1/2}/\sqrt{E_0}$ are indicated near the curves.

The broadening of the spectra of the fragments of molecular ions may result from the Coulomb repulsion of the protons that "suddenly" lost their binding electron. A simple analysis of this situation for the $H_2^+$ ion with kinetic energy $E_0$ and Coulomb repulsion energy $I = e^2/r$, where $r$ is the internuclear distance (with the conservation of the total energy and momentum after the loss of the electron), yields the following expression for the energy difference between the particles: $\Delta E^* \approx 2\sqrt{2}\sqrt{(IE_0)}\cos\alpha$, where $\alpha$ is the angle between the direction of the center-of-mass motion of the $H_2^+$ ion and the straight line connecting the nuclei. Thus, the energy difference $\Delta E^*$ between the fragments of molecular ion should linearly depend on the particle velocity, and the quantity $\Delta E^*/\sqrt{E}$ should be constant. The numerical value of the quantity $\Delta E^*/\sqrt{E}$ depends both on the internuclear distance $r_0$ corresponding to the equilibrium configuration of molecular ion with minimal binding energy ($r_0 = 1.03$ Å for $H_2^+$ and $r_0 = 0.86$ Å for $H_3^+$) and on the orientation of the parent ion relative to the target surface upon flying up to it. The calculation of the maximum possible loss due to the Coulomb repulsion gives $\Delta E^*/\sqrt{E} = 2.16$ eV$^{1/2}$ for $H_2^+$ and $\Delta E^*/\sqrt{E} = 3.4$ eV$^{1/2}$ for $H_3^+$, which agrees well with the experimental data for the quantity $\Delta E_{mol}/\sqrt{E}$ corresponding to the contribution of the "molecular" effect to the spectrum width.

## REFERENCES

1. N. R. Arista, Nucl. Instrum. Methods Phys. Res. B **164–165**, 108 (2000).

2. C. D. Denton *et al.*, Nucl. Instrum. Methods Phys. Res. B **193**, 198 (2002).

3. C. D. Denton, R. Garcia-Molina, I. Abril, and N. R. Arista, Nucl. Instrum. Methods Phys. Res. B **135**, 50 (1998).

4. N. R. Arista *et al.*, Phys. Rev. A **62**, 1261 (2000).

5. R. Garsia-Molina *et al.*, Nucl. Instrum. Methods Phys. Res. B **164–165**, 310 (2000).

6. V. A. Kurnaev, E. S. Mashkova, and V. A. Molchanov, *Light Ion Reflection from Solid Surface* (Énergoatomizdat, Moscow, 1985).

7. N. N. Koborov, A. I. Kuzovlev, V. A. Kurnaev, *et al.*, Nucl. Instrum. Methods Phys. Res. B **129**, 5 (1997).

8. W. Eckstein, *Computer Simulation of Ion–Solid Interactions* (Springer, Berlin, 1991; Mir, Moscow, 1995).

*Translated by E. Golyamina*

# Orbital Phase Transition in $Pr_{1-x}Ca_xMnO_3$

### V. S. Shakhmatov*, N. M. Plakida*, and N. S. Tonchev**

*\* Joint Institute for Nuclear Research, Dubna, Moscow region, 141980 Russia*
*\*\* Institute of Solid State Physics, Bulgarian Academy of Sciences, 1784 Sofia, Bulgaria*
Received October 31, 2002

The phenomenological theory of phase transition in $Pr_{0.6}Ca_{0.4}MnO_3$ manganite is developed. It is shown that this is the orbital phase transition and that the two electronic states of the manganese ion, which are discussed in the literature, result from two different types of condensation of the same orbital order parameter. Thus, the manganese ions in $Pr_{1-x}Ca_xMnO_3$ manganites with $0.3 \leq x \leq 0.5$ may be in either of the two electronic states, depending on the thermodynamic parameters. © 2003 MAIK "Nauka/Interperiodica".

PACS numbers: 64.70.Kb

Recently [1], new structural data on the phase transition (PT) in $Pr_{0.6}Ca_{0.4}MnO_3$ manganite to a state with both charge and orbital ordering was reported. The experimental results were interpreted as the observation of ordered Zener polarons in the low-temperature phase. In addition, it was concluded that this electronic state of a manganese ion may be its ground state in manganites, in which the PT with charge and orbital ordering is observed at the doping level $x = 0.5$. The characteristic feature of this electronic state is that manganese ions have the same valence throughout the crystal, unlike the state [2, 3] in which the charges are separated while the $Mn^{3+}$ and $Mn^{4+}$ ions are spatially ordered.

Note that the complex interrelation between the orbital and charge orderings is also typical of manganites with other doping levels (see, e.g., [4, 5]).

In this paper, we construct the Landau phenomenological theory for the PT in $Pr_{0.6}Ca_{0.4}MnO_3$ on the basis of symmetry analysis. We show that this PT is the orbital PT, while the two states reported in [1] and [2, 3] correspond to two types of orbital ordering of a single orbital order parameter (OP) (for a given (OP), three types of orbital ordering are possible). Hence, it is the orbital and not the charge degrees of freedom which are "soft" and whose condensation leads to the PT.

The PT in $Pr_{0.6}Ca_{0.4}MnO_3$ proceeds from the crystal phase with the $Pnma(D_{2h}^{16})$ symmetry and is associated with the wave vector $\mathbf{k}_1 = (1/2, 0, 0)$ [1–3] (the Cartesian coordinate system used in our consideration is shown in Fig. 1). According to Kovalev [6], the OP for this PT is two-component and can have the symmetry of the irreducible representation (IR) $\tau_1$ or $\tau_2$. Using two invariants, $I_1 = \varphi_1^2 + \varphi_2^2$ and $I_2 = \varphi_1^2 \varphi_2^2$, we represent the free energy in the form

$$F_1 = F_\varphi + F_{\varphi\psi} + F_\psi, \quad (1)$$

where

$$F_\varphi = \frac{1}{2}r(\varphi_1^2 + \varphi_2^2) + \frac{1}{4}u(\varphi_1^2 + \varphi_2^2)^2 + \frac{1}{2}v\varphi_1^2\varphi_2^2, \quad (2)$$

$$F_{\varphi\psi} = \beta_1(\varphi_1^2 - \varphi_2^2)\psi, \quad F_\psi = \frac{1}{2}r_1\psi^2. \quad (3)$$

Here, $r = \alpha(T - T_c)$; $T_c$ is the bare PT temperature; $\alpha$, $r_1$, $u$, $v$, and $\beta_1$ are temperature-independent phenomenological constants; $\{\varphi_1, \varphi_2\}$ is the main two-component OP with wave vector $\mathbf{k}_1 = (1/2, 0, 0)$; and $\psi$ is the secondary OP with wave vector $\mathbf{k}_2 = (0, 0, 0)$.

Note that in expansion (2) we restricted ourselves to the fourth power of the OP, which is sufficient for
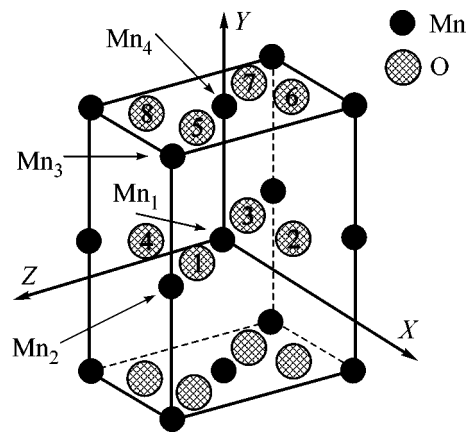


**Fig. 1.** Structure of the manganese ion sublattice in the *Pnma* phase of the crystal. The arrows indicate four nonequivalent manganese atoms in the primitive cell of the crystal, and the numbers 1, …, 8 mark the nonequivalent oxygen ions lying in the $MnO_2$ planes.
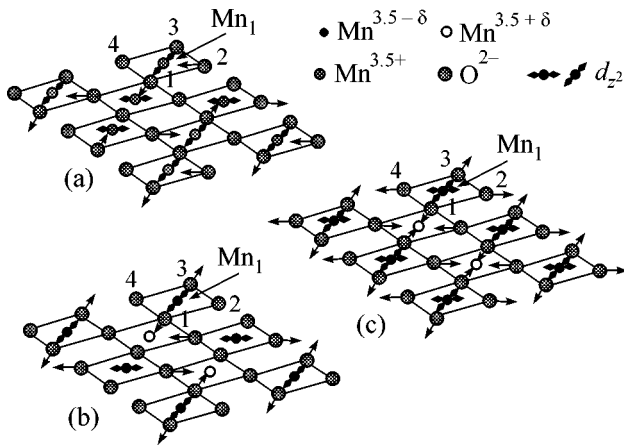
**Fig. 2.** Orbital ordering of the $d_{z^2}$ orbitals in the $MnO_2$ plane. The arrows show the displacements of oxygen atoms. (a) Orbital ordering in the case of the OP condensation of the $\varphi_1 = \varphi_2 \neq 0$ type; (b) orbital ordering in the case of the condensation of two OPs $\varphi_1 \neq 0$ and $\psi \neq 0$; and (c) charge ordering in the case of the condensation of a single secondary $\psi \neq 0$ OP.

describing two low-symmetry phases: $\varphi_i \neq 0$, $\varphi_j = 0$ and $\varphi_1 = \varphi_2 \neq 0$ (see, e.g., [7]). To describe the intermediate phase $\varphi_1 \neq \varphi_2 \neq 0$, it is necessary to include the terms up to the eighth power of the OP inclusive. A complete symmetry analysis for this PT will be described elsewhere. In Eq. (3), one more invariant term is present: $F_{\varphi\psi'} = \beta'_1 \varphi_1 \varphi_2 \psi'$. However, in the orbital structures discussed in this paper, the $\psi'$ OP does not occur.

Figure 2 shows the structure of orbital ordering of the $Mn^{3+}$ $d_{z^2}$ orbitals for two types of OP condensation: $\varphi_1 = \varphi_2 \neq 0$ and $\varphi_i \neq 0$, $\varphi_j = 0$, $\psi \neq 0$ (Figs. 2a and 2b, respectively). In the analysis, we assume that the $d_{z^2}$ orbital in the *Pnma* phase lies in the $MnO_2$ plane and has two possible directions: along $O_4$–$Mn_1$–$O_2$ or along $O_1$–$Mn_1$–$O_3$ (Fig. 1). In the case of the OP of $\tau_1$ symmetry, the orbital direction in the neighboring $MnO_2$ plane does not change (upon the displacement along the *Y* axis), while in the case of the $\tau_2$ symmetry it changes.

The orbital $\{\varphi_1, \varphi_2\}$ and $\psi$ OPs have the physical meaning of the probabilities of an electron occupying the $d_{z^2}$ orbital. In the case of the OP condensation of type $\varphi_1 = \varphi_2 \neq 0$ (Fig. 2a), the probability of occupying the $d_{z^2}$ orbital is the same for all manganese ions, providing the same valence for all manganese ions. In the case of the OP condensation of the $\varphi_1 \neq 0$, $\psi \neq 0$ type (Figs. 2b, 2c), the probabilities that electrons occupy the $d_{z^2}$ orbitals are different for different manganese

ions. This results in the charge separation and spatial ordering of the $Mn^{3.5+\delta}$ and $Mn^{3.5-\delta}$ ions ($\delta > 0$).

Taking into account that the $Mn^{3+}$ $d_{z^2}$ orbital increases the O–$Mn^{3+}$–O bond length (see, e.g., the works of Khomskii and Kugel [8, 9]), we show by arrows in Fig. 2 the displacements of the nearest oxygen atoms, as it follows from the constructed structure of orbital ordering.

Thus, the physical reason for the orbital PT is a decrease in the total free energy at the expense of a decrease in electron energy upon the orientational ordering of the $d_{z^2}$ orbitals with a certain increase in energy due to the elastic deformation of the $MnO_6$ octahedra.

The results of our symmetry analysis (Fig. 2) are presented for manganite with the doping level $x = 0.5$. In the high-symmetry *Pnma* phase, an electron occupies the $d_{z^2}$ orbital of the Mn ion with the probability $P = 50\%$, and the average valence of the manganese ions is $Mn^{3.5+}$. In the low-symmetry phase $\varphi_1 = \varphi_2 \neq 0$, the valence of manganese ions remains the same, i.e., $Mn^{3.5+}$, while in the phase $\varphi_i \neq 0$, $\varphi_j = 0$, the charge separation into the $Mn^{3.5+\delta}$ and $Mn^{3.5-\delta}$ ions takes place (The structures with charge ordering in low-symmetry phases will be considered elsewhere). In the experiments [10, 11], the PT under discussion was observed in $Pr_{1-x}Ca_xMnO_3$ with the concentrations $0.3 < x < 0.7$. It is believed (see, e.g., [1]) that, in the concentration range $0.3 < x < 0.5$, the excess of electrons over the doping level $x = 0.5$ (or the electron deficiency at $0.5 < x < 0.7$; although striped orbital structures may arise in this concentration range [4, 9]) is randomly distributed over the crystal and only gives rise to defects in the orbital structure, without introducing qualitative changes in it. Our model of orbital ordering leads to a different picture for $0.3 < x < 0.5$; in this region, at least two phases with different orbital structures should be observed (for details, see below).

The structure of orbital ordering can be determined by the synchrotron *X*-ray diffraction study [12]. However, the interpretation of the results obtained by this method may be ambiguous [13]. Today, the basic information on the orbital state of a manganese ion is usually extracted from data on the exact structure of the $MnO_6$ octahedron. In this connection, we consider below the phonon degrees of freedom.

In Fig. 3, the arrows indicate the displacements of oxygen and manganese atoms determined from the neutron diffraction data [1–3]. The long Mn–O bonds marked *L* in Fig. 3 indicate the direction of the $d_{z^2}$ orbital in the $MnO_6$ octahedron [8, 9]. The comparison of Figs. 2a and 2b with Figs. 3a and 3b shows that the constructed orbital structures fully agree with the experimental data [1–3].

To describe the deformations of the $MnO_6$ octahedra, we introduce the phonon OPs interacting with the main orbital OP. These are the two-component Jahn–Teller $\{\eta_1, \eta_2\}$ OP, which is characterized by the wave vector $\mathbf{k}_1 = (1/2, 0, 0)$ and the symmetry of the main OP, and the secondary $\xi$ OP characterized by the wave vector $\mathbf{k}_2 = (0, 0, 0)$. The expansion of the free energy with allowance for the orbital and phonon degrees of freedom has the form

$$F = F_1 + F_{\varphi\eta} + F_\eta + F_{\varphi\xi} + F_\xi, \tag{4}$$

where

$$F_{\varphi\eta} = r_3(\varphi_1\eta_1 + \varphi_2\eta_2), \quad F_\eta = \frac{1}{2}r_3'(\eta_1^2 + \eta_2^2), \tag{5}$$

$$F_{\varphi\xi} = \beta_2(\varphi_1^2 - \varphi_2^2)\xi, \quad F_\xi = \frac{1}{2}r_2\xi^2. \tag{6}$$

Thus, for the two cases under consideration, the complete set of condensed orbital and phonon OPs is as follows:

$$\varphi_1 \neq 0, \quad \psi \neq 0, \quad \eta_1 \neq 0, \quad \xi \neq 0,$$
$$\text{and} \quad \varphi_1 = \varphi_2 \neq 0, \quad \eta_1 = \eta_2 \neq 0. \tag{7}$$

Note that, similar to Eq. (3), Eq. (6) contains the additional term $F_{\varphi\xi'} = \beta_2'\varphi_1\varphi_2\xi'$, which should be taken into account in the general case. However, in describing the atomic displacements shown in Figs. 2 and 3, the phonon $\xi'$ OP can be ignored.

The orbital OP has the wave vector $\mathbf{k}_1 = (1/2, 0, 0)$ and the IR symmetry $\tau_1$ or $\tau_2$. Hence, six different PT are possible from the crystal phase with the *Pnma* symmetry:

$$Pnma(D_{2h}^{16}) - \tau_1 \longrightarrow P2_1/m(C_{2h}^2),$$
$$Pmn2_1(C_{2v}^7), \quad Pm(C_s^1), \tag{8}$$

$$Pnma(D_{2h}^{16}) - \tau_2 \longrightarrow P2_1/c(C_{2h}^5),$$
$$Pna2_1(C_{2v}^9), \quad Pc(C_s^2). \tag{9}$$

The low-symmetry phases in Eqs. (8) and (9) are arranged in the following order of OP condensation: $\varphi_1 \neq 0$, $\varphi_1 = \varphi_2 \neq 0$ and $\varphi_1 \neq \varphi_2 \neq 0$, respectively. In the experiments [1–3], the phases with symmetries $P2_1/m(C_{2h}^2)$, $Pmn2_1(C_{2v}^7)$, and $Pm(C_s^1)$ were observed. Therefore, one should take the $\tau_1$ IR. Below, only those phonon basis vectors that are necessary for describing the experimentally observed atomic displacements are written for the $\tau_1$ IR (Fig. 3).

For the two-dimensional $\tau_1$ IR, the symmetrized basis vectors $E(i)$ of atomic displacements are written as

$$E(i) \equiv (e_1(i), e_2(i)). \tag{10}$$
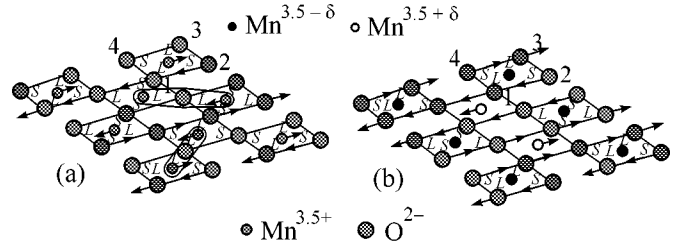
**Fig. 3.** Displacements of oxygen and manganese atoms in the $MnO_2$ plane. The atomic displacements are shown by arrows; *L* and *S* are, respectively, the long and short Mn–O bond lengths in the $MnO_6$ octahedron. (a) Atomic displacements in the low-temperature phase of $Pr_{0.6}Ca_{0.4}MnO_3$ [1]; the shown Mn–O–Mn structural fragments represent Zener polarons [1]. (b) Atomic displacements in the low-temperature phases of $La_{0.5}Ca_{0.5}MnO_3$ [2] and $Pr_{0.5}Ca_{0.5}MnO_3$ [3].

Here, the unit basis vectors $e_1(i)$ and $e_2(i)$ are determined in the space of atomic displacements and related to the phonon $\{\eta_1, \eta_2\}$ OP.

For the manganese atoms, the basis vectors $e_j(i)$ have the form

$$\sqrt{2}e_1(1) = u_x(Mn_2) + u_x(Mn_3),$$
$$\sqrt{2}e_2(1) = -u_x(Mn_1) - u_x(Mn_4),$$
$$\sqrt{2}e_1(2) = u_y(Mn_2) - u_y(Mn_3),$$
$$\sqrt{2}e_2(2) = -u_y(Mn_1) + u_y(Mn_4), \tag{11}$$
$$\sqrt{2}e_1(3) = u_z(Mn_2) + u_z(Mn_3),$$
$$\sqrt{2}e_2(3) = u_z(Mn_1) + u_z(Mn_4),$$

where $u_x(Mn_i)$ is the unit displacement of the $Mn_i$ atom along the *X* axis. The displacements of manganese atoms shown in Figs. 3a and 3b are described by the functions

$$[-e_1(3) - e_2(3)]\exp(-i\mathbf{k}_1\mathbf{R}_n),$$
$$e_1(3)\exp(-i\mathbf{k}_1\mathbf{R}_n), \tag{12}$$

respectively. Here, $\mathbf{R}_n \equiv n_1\mathbf{a}_1 + n_2\mathbf{a}_2 + n_3\mathbf{a}_3$, where $\{n_i\}$ are integer numbers and $\mathbf{a}_i$ are the fundamental translation vectors for the *Pnma* crystal phase. The first of functions (12) is associated with the condensation of the phonon OP of the $\eta_1 = \eta_2 \neq 0$ type, and the second function is associated with the $\eta_1 \neq 0$, $\eta_2 = 0$ type.

For the oxygen atoms in the $MnO_2$ planes, six basis vectors $E(i)$ exist in the general case. Below, only those that describe the displacements in the (*X*, *Z*) plane are presented:

$$2e_1(4) = u_x(O_1) - u_x(O_3) + u_x(O_5) - u_x(O_7),$$
$$2e_2(4) = -u_x(O_2) - u_x(O_4) - u_x(O_6) - u_x(O_8),$$
$$2e_1(5) = u_x(O_2) - u_x(O_4) + u_x(O_6) - u_x(O_8),$$
$$2e_2(5) = -u_x(O_1) - u_x(O_3) - u_x(O_5) - u_x(O_7),$$
$$2e_1(6) = u_z(O_1) - u_z(O_3) + u_z(O_5) - u_z(O_7), \tag{13}$$
$$2e_2(6) = u_z(O_2) + u_z(O_4) + u_z(O_6) + u_z(O_8),$$
$$2e_1(7) = u_z(O_2) - u_z(O_4) + u_z(O_6) - u_z(O_8),$$
$$2e_2(7) = u_z(O_1) + u_z(O_3) + u_z(O_5) + u_z(O_7).$$

The displacements of oxygen atoms shown in Figs. 3a and 3b are described by the functions

$$\{\alpha_1[e_1(6) + e_2(6)] + \alpha_2[e_1(7) + e_2(7)]\}\exp(-i\mathbf{k}_1\mathbf{R}_n), \tag{14}$$

$$[\alpha_1' e_1(6) + \alpha_2' e_1(7)]\exp(-i\mathbf{k}_1\mathbf{R}_n),$$

respectively. The first of functions (14) is associated with the condensation of the phonon OP of the $\eta_1 = \eta_2 \neq 0$ type, and the second function is associated with the $\eta_1 \neq 0$, $\eta_2 = 0$ type. All different mixing coefficients $\{\alpha_i\}$, $\{\alpha_i'\}$, ... satisfy the normalization conditions

$$\sum_i \alpha_i^2 = 1, \sum_i \alpha_i'^2 = 1, \dots.$$

The displacements of manganese and oxygen atoms shown in Fig. 3 are described by functions (12) and (14) with the wave vector $\mathbf{k}_1 = (1/2, 0, 0)$. However, our symmetry analysis shows [see Eqs. (7)] that the secondary phonon $\xi$ OP with the wave vector $\mathbf{k}_2 = (0, 0, 0)$ is also present. The condensation of this OP leads to the additional atomic displacements. We denote the basis vectors for the $\xi$ OP by $e(i)$. For the oxygen atoms in the $MnO_2$ planes, the basis vectors are represented as

$$2\sqrt{2}e(1) = u_x(O_1) + u_x(O_2) - u_x(O_3) - u_x(O_4)$$
$$+ u_x(O_5) + u_x(O_6) - u_x(O_7) - u_x(O_8),$$
$$2\sqrt{2}e(2) = u_z(O_1) - u_z(O_2) - u_z(O_3) + u_z(O_4) \tag{15}$$
$$+ u_z(O_5) - u_z(O_6) - u_z(O_7) + u_z(O_8).$$

The displacements of the oxygen atoms shown in Figs. 2a–2c are described by the functions

$$\{\alpha_1[e_1(4) + e_2(4)] - \alpha_2[e_1(5) + e_2(5)]$$
$$+ \alpha_3[e_1(6) + e_2(6)] + \alpha_4[e_1(7) + e_2(7)]\}\exp(-i\mathbf{k}_1\mathbf{R}_n),$$

$$\alpha_1''[\alpha_1 e_1(4) - \alpha_2 e_1(5) + \alpha_3 e_1(6) - \alpha_4 e_1(7)]$$
$$\times \exp(-i\mathbf{k}_1\mathbf{R}_n) + \alpha_2''[\alpha_1' e(1) + \alpha_2' e(2)]\exp(-i\mathbf{k}_2\mathbf{R}_n), \tag{16}$$
$$[\alpha_1 e(1) + \alpha_2 e(2)]\exp(-i\mathbf{k}_2\mathbf{R}_n)$$
$$= \alpha_1 e(1) + \alpha_2 e(2),$$

respectively. The first of functions (16) is associated with the condensation of the phonon OP of the $\eta_1 =$

$\eta_2 \neq 0$ type, the second is associated with $\eta_1 \neq 0$, $\xi \neq 0$, and the third, with $\xi \neq 0$.

The above analysis shows that all atomic displacements observed in the experiments [1–3] are adequately described by the proposed theory.

Now, we formulate the results of our study. Using the known PT wave vector $\mathbf{k}_1 = (1/2, 0, 0)$, the free-energy expansion was constructed in the form of Eqs. (1)–(3), which describes all PTs from the crystal phase with the *Pnma* symmetry [see Eqs. (8) and (9)]. Based on the experimental data on the symmetry groups of low-temperature phases (see [1–3]), the $\tau_1$ IR was chosen. Symmetry analysis shows that different low-temperature phases with the $P2_1/m(C_{2v}^2)$, $Pmn2_1(C_{2v}^7)$, and $Pm(C_s^1)$ symmetries are formed as a result of three types of OP condensation: $\varphi_1 \neq 0$, $\varphi_1 = \varphi_2 \neq 0$, and $\varphi_1 \neq \varphi_2 \neq 0$, respectively. According to the experimental data in [10, 11], the PT in $Pr_{1-x}Ca_xMnO_3$ manganite with $0.3 < x < 0.7$ results in the orbital and charge orderings. Hence, the OP of this PT is related to either orbital or charge degrees of freedom, while the orbital and charge degrees of freedom may interact with each other. In [1] it was found that all manganese ions in the low-temperature phase of $Pr_{0.6}Ca_{0.4}MnO_3$ have the same valence. This fact suggests that the OP of the PT under discussion is related to the orbital ($d_{z^2}$ orbital) rather than to the charge degrees of freedom. In our phenomenological theory, the $\{\varphi_1, \varphi_2\}$ OP describes the crystal-averaged probability for an electron to occupy the $Mn^{3+}$ $d_{z^2}$ orbital, while all $d_{z^2}$ orbitals lie in the $MnO_2$ plane and have two possible directions in the *Pnma* phase (Fig. 2). Within the framework of this model, it has been shown that, in the case of the OP condensation of the $\varphi_1 = \varphi_2 \neq 0$ type, the orbital orientational ordering leads to the identical valences of manganese ions in the low-temperature phase of $Pmn2_1(C_{2v}^7)$ symmetry (Fig. 2a), while, in the case of the OP condensation of the $\varphi_1 \neq 0$ type, it results in charge separation (the appearance of the $Mn^{3.5+\delta}$ and $Mn^{3.5-\delta}$ ions) and in the orbital structure shown in Fig. 2b ($P2_1/m(C_{2h}^2)$ symmetry of the low-temperature phase). The analysis of atomic displacements also shows that all atomic displacements observed experimentally for the two electronic states of manganese are adequately described within the framework of the proposed phenomenological theory and correspond to two types of orbital OP condensation: $\varphi_1 = \varphi_2 \neq 0$ and $\varphi_i \neq 0$, $\varphi_j = 0$. The low-temperature phase of $P2_1/m(C_{2h}^2)$ symmetry with the OP condensation of the $\varphi_i \neq 0$, $\varphi_j = 0$ type appears when $\tilde{v} > 0$ and $\tilde{u} > 0$, and the phase of $Pmn2_1(C_{2v}^7)$ symmetry with OP condensation of the $\varphi_1 = \varphi_2 \neq 0$ type arises when $\tilde{v} < 0$ and $\tilde{u} + \tilde{v}/2 > 0$,

where $\tilde{v} \equiv v + 4\beta_1^2/r_1 + 4\beta_2^2/r_2$ and $\tilde{u} \equiv u - 2\beta_1^2/r_1 -$ $2\beta_2^2/r_2$ (similar analysis was carried out in [7]). Hence, the sign of the phenomenological constant $\tilde{v}$ determines the formation of one phase or the other. In [1], it was found that the real symmetry of the low-temperature phase of $Pr_{0.6}Ca_{0.4}MnO_3$ is $Pm(C_s^1)$. Our analysis shows that this is the intermediate phase with the OP condensation of the $\varphi_1 \neq \varphi_2 \neq 0$ type, and, hence, it is for this reason that the phenomenological constant $\tilde{v}$ changes sign at the concentration $x \sim 0.4$. Thus, the phase diagram of $Pr_{1-x}Ca_xMnO_3$ with $0.3 < x < 0.7$ [10, 11] should be revised. One can assume that $Pr_{1-x}Ca_xMnO_3$ at $x \sim 0.4$ is in the intermediate phase corresponding to $\varphi_1 \neq \varphi_2 \neq 0$ [1], and in the concentration ranges $0.3 < x < 0.4$ and $x > 0.4$ the two different orbital structures shown in Fig. 2 should be observed. The microscopic theory of the orbital and charge orderings can be developed using the two-orbital double-exchange model (see, e.g., [14]).

## REFERENCES

1. A. Daoud-Aladine, J. Rodriguez-Carvajal, L. Pinsard-Gaudart, *et al.*, Phys. Rev. Lett. **89**, 097205 (2002).

2. P. G. Radaelli, D. E. Cox, M. Marezio, and S.-W. Cheong, Phys. Rev. B **55**, 3015 (1997).

3. Z. Jirak, F. Damay, M. Hervieu, *et al.*, Phys. Rev. B **61**, 1181 (2000).

4. S. Mori, C. H. Chen, and S.-W. Cheong, Nature **392**, 473 (1998).

5. M. V. Lobanov, A. M. Balagurov, V. Yu. Pomjakushin, *et al.*, Phys. Rev. B **61**, 8941 (2000).

6. O. V. Kovalev, *Representations of the Crystallographic Space Groups: Irreducible Representations, Induced Representations, and Corepresentations* (Nauka, Moscow, 1986; Gordon and Breach, Yverdon, Switzerland, 1993).

7. A. D. Bruce and R. A. Cowley, *Structural Phase Transitions* (Taylor and Francis, London, 1981; Mir, Moscow, 1984).

8. K. I. Kugel' and D. I. Khomskiĭ, Usp. Fiz. Nauk **136**, 621 (1982) [Sov. Phys. Usp. **25**, 231 (1982)].

9. D. I. Khomskii and K. I. Kugel, Europhys. Lett. **55**, 208 (2001); cond-mat/0112340 (2001).

10. Z. Jirak, S. Krupica, Z. Simsa, *et al.*, J. Magn. Magn. Mater. **53**, 153 (1985).

11. M. V. Zimmermann, C. S. Nelson, J. P. Hill, *et al.*, Phys. Rev. B **64**, 195133 (2001).

12. Y. Murakami, H. Kawada, H. Kawata, *et al.*, Phys. Rev. Lett. **80**, 1932 (1998).

13. J. Garcia, M. C. Sanchez, J. Blasco, *et al.*, J. Phys.: Condens. Matter **13**, 3243 (2001).

14. G. Jackeli, N. B. Perkins, and N. M. Plakida, Phys. Rev. B **62**, 372 (2000).

*Translated by E. Golyamina*

# Ground-State and Josephson Dynamics of Double-Well Condensates Interacting with Trap Oscillations¶

## L. A. Manakova

*Russian Research Centre Kurchatov Institute, Moscow, 123182 Russia*
*e-mail: manakova@kurm.polyn.kiae.su*
Received November 22, 2002

In the present paper, it is shown that the interaction between classical anharmonic oscillations of a trapped condensate and excited Josephson states corresponding to a large enough initial imbalance of particle number generates their equilibrium bound state. The dynamics of the system are determined by the self-consistent oscillations of the initial imbalance of the particle number and condensate shape. The existence of the bound state implies that the Josephson states can be detected by observing the change of the condensate shape. © 2003 MAIK "Nauka/Interperiodica".

PACS numbers: 03.75.Lm; 05.30.Jp; 32.80.Pj

**1.** Since the discovery of two-component condensates [1] and condensates in a double-well potential [2], the phenomena caused by phase coherence of two-condensated modes attract considerable interest, both experimental and theoretical (see, e.g., [3] and references therein). In [2], spatial quantum coherence was observed by means of the interference pattern in two overlapping condensates. In [4], coherent oscillations of the relative populations were observed in driven two-component condensates with different internal states. As is well known, a bright manifestation of phase coherence is the Josephson effect. In numerous studies devoted to the Josephson effect in systems of two condensates in different internal states [4, 5] or in a double-well potential [6, 7], coherent Josephson oscillations are considered for various dynamical regimes caused by the competition between tunneling and intracondensate interaction (nonlinearity). However, experimental observation of the Josephson effect is difficult, because the small energy splitting associated with Josephson coupling means that thermal and quantum fluctuations will destroy the phase coherence between two condensates even at the lowest achievable temperatures [8, 9]. While the energy splitting can be increased, for instance, by lowering of the barrier height, it then becomes comparable with that of motion states of the condensates.

The problem of interaction between the degrees of freedom generated by the Josephson coupling and states of motion (oscillations) of the trapped condensates was partially analyzed in the work [10]. The present paper focuses on a mechanism of formation of the bound state of the Josephson degrees of freedom

and trap oscillations due to their interaction. The mechanism proposed in what follows may be important for detection of excited Josephson states.

As is well known [3, 6, 7, 12], the Hamiltonian of two condensates with Josephson coupling has the form

$$H_J - E_0 = E_C (\Delta N)^2 - 2E_J \cos \phi. \qquad (1)$$

Here, $\Delta N = N_1 - N_2$, $E_C = \partial \mu / \partial N$, $\mu \equiv \mu_1 = \mu_2$ are the chemical potentials; $N$ are the total particle numbers; $E_J$ describes the Josephson (tunneling) coupling; and $\phi = \theta_1 - \theta_2$ is the relative phase of the condensates. The quantities $E_C$, $E_J$ depend on the total particle number $N$. $(\Delta N)$, $\phi$ are canonically conjugate variables. In (1), the energy origin is the mean-field summed energy of the condensates, namely, $E_0 \equiv \mu N$. The quantization of the Hamiltonian (1) produces the spectrum of the particle number in the Josephson potential $E_J \cos \phi$. The states of this spectrum represent the quantum analogue of Josephson oscillations. As is shown in what follows, any Josephson state can be realized by means of a given initial imbalance in the particle number. For this reason, it is interesting to obtain the complete spectrum generated by the Hamiltonian of (1) and to represent it as a function of the initial imbalance. The Schrödinger equation for the Hamiltonian (1) is derived by means of the quantization rule: $(\Delta N) \longrightarrow -i\partial/\partial\phi$. As a result, we obtain Mathieu's equation. The spectrum for this equation was derived in [11]. Here, we obtain the relation between the quantum numbers and initial imbalance in the particle number. In the Josephson regime $\Delta N \gg 1$ [3], the discrete spectrum

within the range of $-2E_J < \varepsilon < 2E_J$ is specified by the Bohr–Sommerfeld formula:

$$\nu(\varepsilon_\nu) = \oint \frac{d\phi_r}{\pi} \Delta N(\phi_r; \varepsilon_\nu)$$

$$= \oint \frac{d\phi_r}{\pi} \left[ \frac{1}{E_C} (\varepsilon_\nu + 2E_J \cos\phi) \right]^{1/2} \tag{2}$$

$$= \nu_c [E(\kappa) - (1 - \kappa^2) K(\kappa)],$$

$$\nu_c = \frac{8}{\pi} \left( \frac{E_J}{E_C} \right)^{1/2}, \quad \kappa^2 = \frac{\varepsilon_\nu + 2E_J}{4E_J}, \quad \nu_c \gg 1;$$

$K(\kappa)$ and $E(\kappa)$ are complete elliptic integrals of the first and second kinds. The quantity $\nu_c$ is of the maximum possible value of the number of levels in the well. In what follows, the states with $\nu < \nu_c$ are denoted as "libration" states. In the region of $\nu \geq \nu_c$, the $\nu(\varepsilon)$ dependence is determined by the expression

$$\nu(\varepsilon) = \frac{4}{\pi^2} \left( \frac{E_J}{E_C} \right)^{1/2} \kappa E(\kappa^{-1}). \tag{3}$$

The states (3) with $\nu > \nu_c$ are self-trapping states [7]. Equations (2), (3) imply that

$$\varepsilon(\nu) \approx -2E_J + \omega_m \nu \quad \text{at} \quad 1 \ll \nu \ll \nu_c,$$
$$\varepsilon(\nu) \approx 4\pi^2 E_C \nu^2 \quad \text{at} \quad \nu \gg \nu_c. \tag{4}$$

At the same time, it is easy to show that $d^2\varepsilon(\nu)/d\nu^2 < 0$ at $\nu < \nu_c$ and $d^2\varepsilon(\nu)/d\nu^2 > 0$ at $\nu > \nu_c$. At $\nu = \nu_c$, the curve $\varepsilon(\nu)$ has a flex point.

Since energy is conserved, a state with a given $\nu$ value can be realized by means of the definition of the initial values of $(\Delta N)_0$ and $\phi(0)$. Namely, $\varepsilon(\nu) = E_C(\Delta N)_0^2 - 2E_J \cos\phi(0)$. Supposing that $\phi(0) = 0$, we obtain the following relation between $\nu$ and $(\Delta N)_0$:

$$\varepsilon(\nu) = -2E_J + E_C(\Delta N)_0^2. \tag{5}$$

Using Eqs. (4), (5), we arrive at the expressions

$$\nu = \frac{1}{2\pi} |(\Delta N)_0| \quad \text{for the self-trapping (sf) states,}$$

$$\nu = \left( \frac{E_C}{\omega_m} \right) (\Delta N)_0^2 \quad \text{for the "libration" (l) states.} \tag{6}$$

**2.** The interaction of Josephson states and condensate oscillations can be realized by the following mechanisms. First, the interaction is secured if we allow for the dependence of $E_C$ in $\varepsilon(x)$ on the atom displacements. The latter are generated by the condensate oscillation. Second, the interaction can be realized by applying a two-photon traveling-wave laser pulse with the Rabi frequency $\Omega$. The pulse both creates condensates with the different particle numbers and induces the interaction of an atom's displacements with the excited Josephson states corresponding to the particle-number

imbalance created by the pulse. The general description proposed in what follows is independent of a specific mechanism.

Let us consider the classical states of motion of the condensate. These states may be described in terms of the complex amplitudes $a^*$, $a = n^{1/2} e^{\pm i\varphi_1}$, where $n = \langle a | \hat{a}^+ \hat{a} | a \rangle = |a|^2$ is the average number of quanta in the coherent state $|a\rangle$. The variables $n$, $\varphi_1$ are canonical. By "classical state of motion" we mean that its number of quanta is very large, $n \gg 1$. It is convenient to specify the relation between the $a$, $a^*$ amplitudes and the $\hat{a}$, $\hat{a}^+$ operators as $a = N^{-1/2} \hat{a}$. Here, the commutator of $a$, $a^*$ is equal to zero with macroscopic accuracy: $[a, a^*] = 1/N \longrightarrow 0$. The Hamiltonian of the motion states can be written in the form $N\epsilon(n)$. For the quasiclassical Josephson states with $\nu \gg 1$, the $c_\nu$, $c_\nu^*$ amplitudes may be written in the form $c_\nu = \nu^{1/2} e^{i\varphi_2}$. However, it is convenient to rewrite $\varepsilon(\nu)$, $c_\nu$ by means of the variable $x = |(\Delta N)_0|/N^{1/2} \gg 1$. Combining this inequality with the requirement that $x = |(\Delta N)_0|/N \ll 1$, we arrive at the conditions for the $x$ values: $1 \ll x \ll N^{1/2}$. Using Eqs. (4), (5), we find that $\nu = \nu(x)$, $\varepsilon(\nu) = N(-E_J/N + E_C x^2)$. In the general case, the $\nu(x)$ dependence is implicit. It is determined by Eqs. (2), (3), and (5). However, in the particular cases of the "libration" ($\varepsilon(\nu) \ll E_J$) and self-trapping ($\varepsilon(\nu) \gg E_J$) states, the relations between $\nu$ and $(\Delta N)_0$ can be represented in a simple form, as is seen from (6). By means of Eqs. (5) and (6), we come to the expressions $H_0 \equiv N\varepsilon_0(n, x) = N[-(E_J/N) + \epsilon(n) + E_C x^2]$ and

$$c_\nu^{(sf)} = N^{1/4} x^{1/2} e^{i\varphi_2} \equiv N^{1/4} c_x^{(sf)},$$

$$c_\nu^{(l)} = N \left( \frac{E_C}{\omega_m} \right)^{1/2} x e^{i\varphi_2} \equiv N \left( \frac{E_C}{\omega_m} \right)^{1/2} c_x^{(l)}. \tag{7}$$

For any mechanism producing an interaction between two subsystems, it can be written in the form of a multiple Fourier series in $\varphi_1$, $\varphi_2$

$$H_{\text{int}} = N \sum_{k_1 k_2} [g_{k_1 k_2}(N) a^{*k_1} c_\nu^{k_2} + \text{c.c.}]$$

$$= N \sum_{k_1, k_2 > 0} [g_{k_1 k_2}^{(sf, l)}(N) n^{k_1/2} x^{\alpha k_2} e^{i(k_1 \varphi_1 - k_2 \varphi_2)} + \text{c.c.}], \tag{8}$$

$$\alpha_{sf} = \frac{1}{2}, \quad \alpha_l = 1.$$

Here, $k_1$ and $k_2$ are integers. For the sake of simplicity, we disregard the phase-independent interaction in

Eq. (8). Using Eq. (7), we obtain

$$g_{k_1k_2}^{(sf)}(N) = g N^{-1 + k_2/4},$$

$$g_{k_1k_2}^{(l)}(N) = g N^{-1 + k_2} \left(\frac{E_C}{\omega_m}\right)^{k_2/2}. \tag{9}$$

The constant $g$ is specified by the concrete mechanism producing the interaction. Let us assume that the term with the phase $\phi_k^r = k_1\phi_1 - k_2\phi_2$, which varies anomalously slowly with time, can be set off in sum (8). It is possible to make this assumption under two conditions:

$$k_{1r}\left(\frac{d\epsilon(n)}{dn}\right) = k_{2r}\left(\frac{d\epsilon_J(x)}{dx}\right),$$

$$\left(\frac{d^2 H_0}{dx^2}\right)_{x = x_m} (\Delta x)_{\max} \gg \left(\frac{\partial H_{\text{int}}}{\partial x}\right)_{x = x_m}, \tag{10}$$

where the $x_m$ value is determined from the first equality in (10)

$$x_m = \frac{k_{1r}\epsilon_n'}{2k_{2r}E_C}, \quad \epsilon_n' \equiv \left(\frac{d\epsilon(n)}{dn}\right). \tag{11}$$

The inequality in (10) is written taking into account that $H_0$, $H_{\text{int}}$ are functions of a single dynamic variable, e.g., $x$. The $\epsilon_n'$ quantity defines the level separations of an oscillation spectrum. From Eqs. (10) and (11), one finds that the time variation of the $\phi_k^r$ phase is proportional to $(d^2 H_0/dx^2)_m(\Delta x)$, where $(\Delta x)$ is the change in $x$ near the $x_m$ value. The maximum $(\Delta x)_{\max}$ value specifies the width of the near-minimum region, since $d\phi_k^r/dt \sim \Delta x$. The second condition in (10) implies that the width of the near-minimum region is large at the characteristic interaction-variation scale. An estimate of $(\Delta x)_{\max}$ is given in what follows. Thus, the leading term in sum (8) has the form

$$H_{\text{int}}^{(r)} = H g_k^{(sf, l)}(N; n, x)\cos\phi_k,$$

$$\phi_k = k_{1r}\theta_1 - k_{2r}\theta_2. \tag{12}$$

All remaining terms in this sum are rapidly oscillating perturbations and will be disregarded in this work. Here and below, the index $k$ in $g_k$ and $\phi_k$ denotes a set of $k_{1r}$, $k_{2r}$. One can easily show that, aside from the energy $H = N[\epsilon_0(n, x) + g_k(N; n, x)\cos\phi_k]$, the system in question has an additional integral of motion $n_0 = n/k_{1r} + x/k_{2r}$, $dn_0/dt = 0$. For this reason, the first condition in (10) is equivalent to the condition of the minimum of $\epsilon_0(n_0, x)$ over $x$ at a given $n_0$ value. Supposing for the sake of simplicity that $k_{1r} = k_{2r} = k$, one can readily show that the second condition in (10) is met provided $x_m$, $(n_0 - x_m) \gg k$. And, for this reason, it is fulfilled with macroscopic accuracy. Using Eqs. (10)–(12), it is straightfor-

ward to write the Hamiltonian $H_m = H_0 + H_{\text{int}}^{(r)}$ near the minimum of the first nonvanishing order in $(\Delta x)$:

$$H_m = N\left[\epsilon_0(n_m; x_m) + \left(\frac{d^2\epsilon_0}{dx^2}\right)_m (\Delta x)^2 - g_{km}\cos\phi_k\right], \tag{13}$$

where $n_m = n_0 - k_1 x_m/k_{2r}$, $(d_2\epsilon_0/dx^2)_m = 2E_c$, and $g_{km} = g_k^{(sf, l)}(N; n_m, x_m)$. Terms with the derivatives of $H_{\text{int}}$ are absent in Eq. (13) due to the inequality in (10). Equation (13) implies that $(\Delta x)_{\max} \sim (g_{km}/E_c)^{1/2}$. Using the fact that $E_C \sim \omega_0(a/a_0)^{2/5}N^{-3/5}$ in the Thomas–Fermi approximation [12] (here $a$, $a_0 \sim (1/M\omega_0)^{1/2}$ are the scattering and oscillator lengths), we can represent the $1 \ll x_m \ll N^{1/2}$ inequalities in the form

$$\frac{1}{N}\left(\frac{Na}{a_0}\right)^{2/5} \ll \frac{k_{1r}}{k_{2r}}\left(\frac{\epsilon_n'}{\omega_0}\right) \ll \frac{1}{N^{1/2}}\left(\frac{Na}{a_0}\right)^{2/5}. \tag{14}$$

As is known [12], the $(Na/a_0) \gg 1$ relation occurs in the Thomas–Fermi approximation. However, $N^{-1/2}(Na/a_0)^{2/5} \ll 1$. Owing to these relations, the condition (14) or (what is the same) (10) specifies the region of the dense oscillation spectrum, where $\epsilon_n' \ll \omega_0$. Both here and in what follows, we suppose that $k_{1r} = k_{2r} = 1$ for the sake of simplicity.

**3.** At a fixed $n_0$ value, the principal contribution to the partition function comes from the neighborhood of the minimum at $x = x_m$. The expression for $Z(n_0; x_m; T)$ is equal to

$$Z(n_0; x_m; T) = \text{const}\int_{-\infty}^{\infty} d(\Delta x)$$

$$\times \int_{-\pi}^{\pi} d\phi_k e^{-\beta H_m(n_0, (\Delta x), \phi_k)} \tag{15}$$

$$\approx \frac{\exp[-\beta N\epsilon_0(N; n_m; x_m) + \ln I_0(\beta N g_{km})]}{(\beta N E_C)^{1/2}},$$

where $\beta = 1/T$, $T$ is temperature, and $I_0(x)$ is the modified Bessel function. Using Eq. (15), we come to the following equation for the $\bar{n}_m$ value realizing the minimum of the free energy:

$$\left(\frac{d\epsilon_{0m}}{dn_m}\right)_{n_m = \bar{n}_m} = \left(\frac{dg_{km}}{dn_m}\right)_{n_m = \bar{n}_m} \frac{I_1(\beta N g_{km})}{I_0(\beta N g_{km})}, \tag{16}$$

$$I_1(x) = I_0'(x).$$

In addition to $\bar{n}_m$, the thermodynamic average of $\cos\phi_k$ is determined from Eq. (15). This average is equal to

$$\langle\cos\phi_k\rangle_T = -\frac{\partial\ln Z}{\partial(\beta N g_{km})}$$
$$= \frac{\partial F}{T\partial(\beta N g_{km})} = \frac{I_1(\beta N g_{km})}{I_0(\beta N g_{km})}. \qquad (17)$$

The order parameters $\bar{n}_m$, $\langle\cos\phi_k\rangle_T$ describe a new coherent state. There is the bound state of the $\bar{n}_m$ oscillation quanta and the Josephson state generated by the initial imbalance in the particle number, which corresponds to the $x_m$ value. In addition, this state has the equilibrium phase-coherence factor $\langle\cos\phi_k\rangle_T$. The $\bar{n}_m \neq 0$ value provides the equilibrium distortion of the condensate shape. The equations obtained above imply that the shape distortion is self-consistently coupled to the $x_m$ value defining the equilibrium initial imbalance in the particle number.

At $T = 0$, the $\bar{n}_m$ value reaches the minimum of the thermodynamic energy

$$E_m = N[\varepsilon_0(N; n_m, x_m) - g_{km}(N; n_m, x_m)]. \qquad (18)$$

To determine the $\bar{n}_m(T = 0)$ value, it is suitable to use the following consideration. As is well known, the level separations $\epsilon'_n$ change slowly depending on $n$ in the dense (quasiclassical) spectrum. For this reason, we can suppose that $\epsilon'_n \approx \text{const} \equiv \omega_b \ll \omega_0$. On this assumption, the $x_m$ value does not depend on $n_m$, and the $\bar{n}_m$ quantity realizing the minimum of $E_m$ is equal to

$$\bar{n}_m^{1/2} = \frac{g^{(sf, l)}(N)x_m^\alpha}{2\omega_b}, \quad \alpha_{sf, l} = \frac{1}{2}, 1 \qquad (19)$$

(it is worth noting that $(\partial^2 E_m/\partial n_m^2) > 0$). Both here and in what follows, the $g_{k=1}^{(sf, l)}(N) \equiv g^{(sf, l)}(N)$ denotation is used. Taking Eq. (19) into account, one readily gets

$$\bar{g}_{1m}^{(sf)} = \frac{g^{(sf)2}(N)x_m}{2\omega_b}, \quad \bar{g}_{1m}^{(l)} = \frac{g^{(l)2}(N)x_m^2}{2\omega_b}, \qquad (20)$$

$$\frac{E_m^{(sf)}}{N} = -\frac{E_J}{N} - \frac{g^{(sf)2}(N)}{8E_C}\left(1 - \frac{8E_c^2 x_m^2}{g^{(sf)2}(N)}\right),$$
$$\frac{E_m^{(l)}}{N} = -\frac{E_J}{N} - \frac{g^{(l)2}(N)x_m}{16E_C}\left(1 - \frac{16E_c^2 x_m}{g^{(l)2}(N)}\right). \qquad (21)$$

The expressions for the energies imply, first, that we obtain the minimum in the region of sufficiently dense oscillation spectrum, which satisfies condition (14). The minimum corresponds to the formation of the bound state for the $\bar{n}_m$, $x_m$ values. Second, as is seen from Eq. (21), the absolute minimum of $E_m$ can be realized under the conditions

$$1 \ll x_m < \frac{g^{(sf)}(N)}{8E_C}, \quad 1 \ll x_m < \frac{g^{(l)2}(N)}{16E_C^2}. \qquad (22)$$

These inequalities are met when the interaction matrix elements $g^{(sf, l)}(N)$ are large enough. Let us estimate the condensate parameters that are required for the existence of the absolute minimum. In the Thomas–Fermi approximation, the $g^{(sf)}(N) \gg E_C$ inequality occurs provided that the total particle number is not very large, namely, $N \ll (g/\omega_0)(a_0/a)^{8/3}$. In turn, the $g^{(l)2}(N) \gg E_C^2$ relation holds true under the condition $N^{0.1}[g^2/(\Omega^{1/2}\omega_0^{3/2})](a_0/a)^{0.6} \gg 1$. Here, we use the fact that $E_J = \Omega N$. The latter condition is fulfilled for all admissible parameters provided $g^2/(\Omega^{1/2}\omega_0^{3/2}) \sim 1$. It should be emphasized that the right-hand-side inequalities in Eq. (22) are much stronger than the condition $x_m \ll N^{1/2}$. These conditions imply that the libration Josephson state forms the bound state with the condensate oscillation rather than the self-trapping state.

**4.** The Hamiltonian (13) describes the dynamics of the system that has the ground state with the parameters $x_m$, $\bar{n}_m$ and phase $\phi_k(0) = 0$ at $t = 0$. In the ground state, the initial imbalance in the particle number is equal to $|(\Delta N)_{0m}| = N^{1/2}x_m = N^{1/2}\omega_b/2E_C$. In the case considered here, the canonical equations of motion have the form $\partial\phi_k/\partial t = \partial h_m/\partial(\Delta x)$, $\partial(\Delta x)/\partial t = -\partial h_m/\partial\phi_k$, where $h_m = \bar{H}_m/N$. The Hamiltonian $\bar{H}_m$ is obtained from $H_m$ in Eq. (13) at $n_m = \bar{n}_m$ and $g_{1m} = \bar{g}_{1m}$. The $\bar{n}_m$ and $\bar{g}_{1m}$ quantities are determined in Eqs. (19) and (20), respectively. The solutions of the equations of motion describe the self-consistent oscillations of the initial imbalance and condensate shape. The first oscillates around the $(\Delta N)_{0m}$ value. The shape of the condensate changes around that which corresponds to the $\bar{n}_m$ value. Note that $(\Delta x) = -\Delta n$. For the libration state, the maximum frequency of the oscillations is determined by the expression

$$\omega_m^{(l)2} = E_C\bar{g}_{1m}^{(l)} \sim g^2\frac{\omega_b}{\omega_m}, \qquad (23)$$

where $\omega_m = (E_C E_J)^{1/2}$ is the maximum oscillation frequency for the "unperturbed" Josephson Hamiltonian (1). In the Thomas–Fermi approximation, one readily finds that $E_C \ll \omega_m \ll E_J$. Taking into account that $\omega_b \gg E_C$ (see Eq. (11)) and supposing that $\omega_b \sim E_J$, we obtain

$$\frac{\omega_m^{(l)}}{\omega_m} \sim \left(\frac{g_{1m}^{(l)}}{E_J}\right)^{1/2} \sim \left(\frac{g^{(l)}(N)}{E_C}\right)\left(\frac{\omega_b}{E_J}\right)^{1/2} \gg 1. \qquad (24)$$

Quite a different situation occurs for the self-trapping states. In this case, we have

$$\omega_m^{(sf)} = (E_C g_{1m}^{(sf)})^{1/2} \sim g^{(sf)}(N),$$

$$\frac{\omega_m^{(sf)}}{\omega_m} \sim \left(\frac{g^{(sf)}(N)}{E_C}\right)^{1/2} \left(\frac{g^{(sf)}(N)}{E_J}\right)^{1/2}$$

$$\sim \left(\frac{g^{(sf)}(N)}{E_C}\right)^{1/2} \left(\frac{g}{\Omega}\right)^{1/2} N^{-7/8}. \qquad (25)$$

Taking the conditions (22) into account, one finds that Eq. (25) implies that the ratio $\omega_m^{(sf)}/\omega_m$ may take on an arbitrary value.

It should be emphasized that the bound state arises in the neighborhood of the minimum of the $\varepsilon_0(n_0; x)$ function, where the conditions (10) are met. The conditions (10) specify the type of interaction between the Josephson and oscillation degrees of freedom. In addition, the first condition in (10) imposes definite restrictions on the spectrum of the oscillation states, which may effectively interact with the Josephson degrees of freedom. Namely, the density of oscillation states should satisfy the inequalities (14). The region of the dense spectrum exists in the neighborhood of the barrier top. In this case, according to the consideration proposed above, the equilibrium bound state of the highly excited oscillation and Josephson states is formed. The existence of the bound state generates the equilibrium distortion of the condensate shape specified by the $\bar{n}_m$

value. This mechanism can provide the experimental detection of the excited Josephson states. In addition, Eqs. (21) imply that there quantum phase transitions to a state with $\bar{n}_m \neq 0$ can be observed.

## REFERENCES

1. C. J. Myatt, E. A. Burt, R. W. Christ, *et al.*, Phys. Rev. Lett. **78**, 586 (1997).
2. M. R. Andrews, C. G. Townsend, H.-J. Meisner, *et al.*, Science **275**, 637 (1997).
3. A. J. Leggett, Rev. Mod. Phys. **73**, 307 (2001).
4. D. S. Hall, M. R. Mattews, C. E. Wiemann, and E. A. Cornell, Phys. Rev. Lett. **81**, 1543 (1998).
5. J. Williams, R. Walser, J. Cooper, *et al.*, Phys. Rev. A **59**, R31 (1999).
6. I. Zapata, F. Sols, and A. J. Leggett, Phys. Rev. A **57**, R28 (1998).
7. S. Raghavan, A. Smerzi, S. Fantoni, and V. B. Shenoy, Phys. Rev. A **59**, 620 (1999).
8. F. Meir and W. Zweger, Phys. Rev. A **64**, 033610 (2001).
9. L. P. Pitaevskii and S. Stringari, Phys. Rev. Lett. **87**, 180402 (2001).
10. L. A. Manakova, cond-mat/0210573.
11. L. A. Manakova, JETP Lett. **73**, 39 (2001).
12. F. Dalfovo, S. Giorgini, L. P. Pitaevskii, and S. Stringari, Rev. Mod. Phys. **71**, 463 (1999).

# Observation of Structural Vacancies

## A. A. Valeeva[1, *], G. Tang[2], A. I. Gusev[1, *], and A. A. Rempel[1]

*[1]Institute of Solid-State Chemistry, Ural Division, Russian Academy of Sciences,*
*ul. Pervomaĭskaya 91, Yekaterinburg, 620219 Russia*
*\* e-mail: valeeva@ihim.uran.ru; gusev@ihim.uran.ru*
*[2]Institut für Theoretische und Angewandte Physik, Universität Stuttgart, 70550 Stuttgart, Germany*
Received November 28, 2002

A method using the atom–vacancy ordering phenomenon for the visualization of structural vacancies in crystals was suggested and implemented. The ordered nonstoichiometric titanium monoxide $Ti_5O_5$ was taken as the object of investigation, because the structural vacancies in this compound can be observed due to the formation of continuous vacancy channels in certain crystallographic directions. The structural vacancies in the specially oriented sample of ordered titanium monoxide were directly observed by high-resolution transmission electron microscopy with a magnification of $4 \times 10^6$. © 2003 MAIK "Nauka/Interperiodica".

PACS numbers: 61.72.Ji; 68.37.Lp; 61.72.Ff

Structural vacancies are an important and inherent element of the crystal structure of cubic ($B1$ structure) carbides, nitrides, and oxides $MX_y$ (M is the group IV or V transition metal and X = C, N, or O) forming a group of strongly nonstoichiometric compounds [1]. The concentration of structural vacancies in them can be as high as several tens of atomic percent. Inasmuch as most of the strongly nonstoichiometric compounds contain structural vacancies only in the nonmetallic sublattice, their composition is written as $MX_y \equiv MX_y\square_{1-y}$, where $\square$ is the nonmetallic structural vacancy and $0.5 < y < 1.0$. However, some compounds, such as titanium and vanadium monoxides and niobium nitride, have a double defectiveness, i.e., contain structural vacancies in both sublattices. Cubic titanium monoxide $TiO_y \equiv Ti_xO_z \equiv Ti_x\blacksquare_{1-x}O_z\square_{1-z}$ ($y = z/x$ and $\blacksquare$ is the structural vacancy in the metallic sublattice) has a very broad homogeneity region from $TiO_{0.7}$ to $TiO_{1.25}$, and the vacancy concentration in each of the sublattices of $TiO_y$ monoxide can achieve 15–17 at. %. Due to the interparticle interactions, the structural vacancies in $TiO_y$ are ordered to form stable monoclinic $Ti_5O_5$ superstructure (space group $C2/m$ ($A12m/1$)) in the range $0.9 < O/Ti < 1.1$ at temperatures below 1000–1200 K [2, 3].

So far, the existence of both structural and thermal vacancies has been confirmed by convincing, though indirect, proofs based on the analysis of various properties as functions of temperature and composition. In this work, the method is proposed and implemented for the observation of structural vacancies using the ordering effect in titanium monoxide.

High-resolution transmission electron microscopy (HTEM) was used as a method for the observation of structural vacancies [4]. This method allows the direct observation of the network of crystal atomic sites. The corresponding image is a result of the superposition of tens of atomic layers. In the disordered state, structural vacancies are randomly distributed, so that each column of lattice sites contains both atoms and vacancies. Since the different columns have the same relative content of atoms and vacancies, they do not contrast in the image, and the structural vacancies are not seen. Because of the random distribution, the thermal vacancies have not been observed so far, although they exist in all crystals at any finite temperature.

The structural vacancies can be visualized in the ordered nonstoichiometric compound. The structural vacancies in these compounds are arranged in an ordered way, so that one can identify the directions which pass only through the vacancy sites to form continuous vacancy channels. In the case of ideal ordering, the atomic columns and vacancy channels are arranged with a certain periodicity, so that the HTEM images should have contrast at those sites where the atomic rows are disrupted by the vacancy channels oriented perpendicular to the image plane.

Since the nonmetallic interstitial O, C, and N atoms are weaker scatterers than the transition metals, the main information in the HTEM images is associated with the metallic sublattice. For this reason, the structural vacancies cannot be observed in the ordered carbides and nitrites, because they are situated solely in the nonmetallic sublattice. Consequently, those ordered nonstoichiometric compounds in which the vacancy concentration in the metallic sublattice is large are of the greatest interest for vacancy observation. The ordered titanium monoxide $Ti_5O_5$ ($Ti_5\blacksquare O_5\square$) containing 16.7 at. % vacancies in each of the titanium and oxygen sublattices is the optimal object for the direct observation of structural vacancies.

A sample of disordered titanium monoxide $TiO_{1.087}$ ($Ti_{0.833}O_{0.906}$) was prepared by high-temperature vacuum synthesis from titanium and titanium dioxide powders. To obtain the ordered state, the synthesized sample was annealed at 1330 K for 4 h followed by slow cooling to 300 K at a rate of 10 K h$^{-1}$. The synthesis method and the synthesis conditions, as well as the results of certifying the samples of the nonstoichiometric disordered and ordered titanium monoxide over the entire range of existence of the cubic phase, are described in detail in [5].

The crystal structure of titanium monoxide was studied by X-ray structural analysis on a Siemens D-500 autodiffractometer in the Bragg–Brentano photography geometry using $CuK\alpha_{1,2}$ radiation in the $2\theta$ range from $10°$ to $160°$ with the step $\Delta(2\theta) = 0.025°$. The photography was carried out on finely divided titanium monoxide powders. The micro- and crystal structures of titanium monoxide were also studied by electron microscopy and electron diffraction. The microstructure was studied on a foil with a thickness of no greater than 50 nm.

The high-atomic-resolution images were made using a JEM-4000FX electron microscope (wavelength $\lambda = 0.00164$ nm). To determine the orientation of the ordered $Ti_5O_5$ monoxide about the electron-beam direction, the sample structure was preliminary studied by electron diffraction. Then the same sample was studied by HTEM, with the electron diffraction angle relative to the high-resolution images being zero, so that the electron beam direction relative to the sample did not change. Electron diffraction was studied using a Philips CM-200 electron microscope with a beam width of 70 nm and wavelength $\lambda = 0.00251$ nm.

Analysis of the X-ray and electron diffraction data showed that the atomic and vacancy ordering in $TiO_y$ corresponds to the monoclinic $Ti_5O_5$ ($Ti_5\blacksquare O_5\square$) superstructure belonging to the space group $C2/m$ ($A12m/1$) described in [3, 5–10]. The primitive translation vectors of this superstructure in the coordinates of the basis $B1$ structure are $\mathbf{a}_m = \{10\text{–}1\}_{B1}$, $\mathbf{b}_m = \{0\ 1\ 0\}_{B1}$, and $\mathbf{c}_m = \{1\ 0\ 2\}_{B1}$.

The determination of the $Ti_xO_z \longleftrightarrow Ti_5O_5$ order–disorder phase-transition channel and the calculation of the distribution functions $n(\mathbf{r})$ for the titanium and oxygen atoms [1, 3, 11] showed that the titanium distribution in the monoclinic superstructure (space group $C2/m$) of $Ti_xO_z$ monoxide is described as

$$n_{Ti}(x_I, y_I, z_I)$$
$$= x - (\eta_{10}^{Ti}/6)\cos 2\pi z_I - (\eta_4^{Ti}/3)\cos[4\pi(x_I + z_I)/3] \quad (1)$$
$$- (\eta_1^{Ti}/3)\cos[2\pi(2x_I - z_I)/3],$$

and the oxygen distribution in the same superstructure is described by the function

$$n_O(x_I, y_I, z_I)$$
$$= z + (\eta_{10}^O/6)\cos 2\pi z_I - (\eta_4^O/3)\cos[4\pi(x_I + z_I)/3] \quad (2)$$
$$+ (\eta_1^O/3)\cos[2\pi(2x_I - z_I)/3],$$

where $x_I$, $y_I$, and $z_I$ are the coordinates of sites $\mathbf{r}$ in the ordered sublattice and $\eta_{10}$, $\eta_4$, and $\eta_1$ are the long-range order parameters. A completely ordered state of titanium monoxide is achieved when all long-range order parameters are equal to unity for each sublattice; i.e., $\eta_{10} = \eta_4 = \eta_1 = 1$. The distribution functions $n_{Ti, O}(\mathbf{r}) \equiv n_{Ti, O}(x_I, y_I, z_I)$ describe the structure of an ordered crystal in analytic form suitable for direct quantitative calculations. These functions are invariant under all symmetry transformations of the ordered crystal lattice and have a physical meaning of the probability of finding an atom of a given sort at site $\mathbf{r}$.

The analysis of the distribution functions (1) and (2) showed that the ordered monoclinic $Ti_5O_5$ monoxide has two types of continuous vacancy channels and allowed their directions to be determined. Vacancy channels of the first type pass through the vacant sites of only one sublattice, either titanium or oxygen. In the general form, the vacancy channels have the following directions: $[2m, \pm2n + 1, 2m + 1]_{C2/m} \equiv [4m + 1, \pm2n + 1, 2(m + 1)]_{B1}$ and $[2(m + 1), \pm2n + 1, 2m + 1]_{C2/m} \equiv [3(2m + 1), \pm2n + 1, 0]_{B1}$, where $m$ and $n$ are integers.

The vacancy channels of the second type pass through the sequentially alternating nonmetallic and metallic vacancies. These channels have the following directions: $[2m + 1, \pm2n + 1, 0]_{C2/m} \equiv [2m + 1, \pm2n + 1, \pm2(m + 1)]_{B1}$ and $[1, \pm2n, 2m + 1]_{C2/m} \equiv [2(m + 1), \pm2n, 4m + 1]_{B1}$, where $m$ and $n$ are integers, as well as $[2m - 2p - 1, \pm2n + 1, m + 2p + 1]_{C2/m} \equiv [3m, \pm2n + 1, 3(2p + 1)]_{B1}$ ($m \neq 0$, $n$, and $p$ are integers) and $[2m - 2p - 1, \pm2n, m + 2p + 1]_{C2/m} \equiv [3m, \pm2n, 3(2p + 1)]_{B1}$ ($n \neq 0$, $m$, and $p$ are integers).
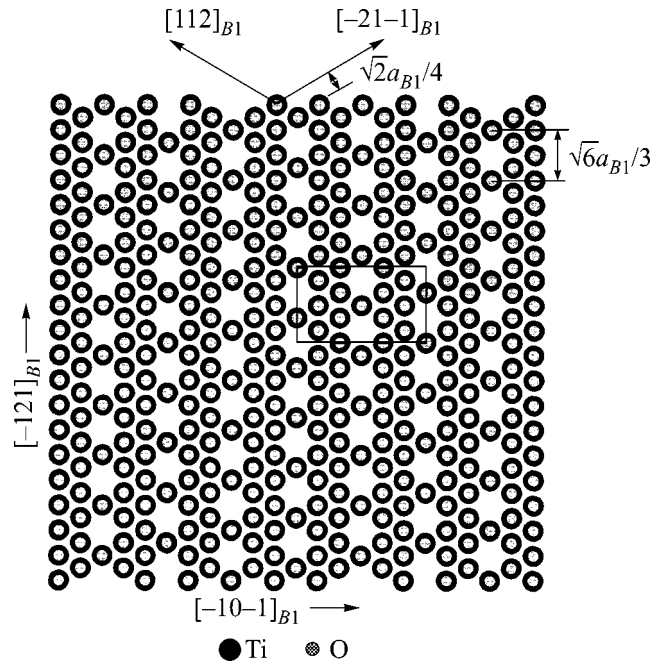
A search for the directions that are most favorable to the observation of vacancy channels in the ordered monoclinic (space group $C2/m$) $Ti_5O_5$ monoxide using high-resolution electron microscopy was accomplished by computer simulation. Only those vacancy channels can be observed whose directions coincide with the electron-beam direction. Besides, to observe a vacancy in the experiment, it is essential that the distances between the atomic rows and between the atoms in the row be no less than the electron microscope resolution (0.09 nm) in the atomic projection onto the plane perpendicular to the chosen direction. All things being the same, a decrease in the foil thickness is favorable to the vacancy visualization. The analysis of the crystal lattice of the ordered $Ti_5O_5$ monoxide with allowance for the interatomic and interplanar spacing and the revealed directions of the continuous vacancy channels showed
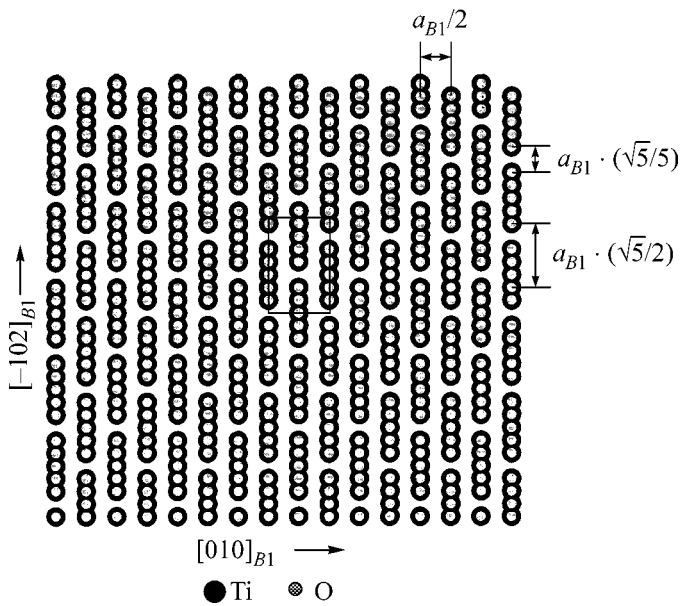
**Fig. 1.** The distribution of the structural vacancies and the titanium and oxygen atoms observed in the projection (along the $[1\ 0\ 1]_{C2/m} \equiv [2\ 0\ 1]_{B1}$ direction) onto the $(1\ 0\ 4)_{C2/m} \equiv (2\ 0\ 1)_{B1}$ plane of the ordered monoclinic titanium monoxide $Ti_5O_5$ (space group $C2/m$). The visible distance $d_{row}$ between the rows of like atoms is $a_{B1}/2$. The discontinuities between the atoms of the same row indicate the vacancy channels in the $[1\ 0\ 1]_{C2/m} \equiv [2\ 0\ 1]_{B1}$ direction. The distance between the vacancy-separated atoms is $(\sqrt{5}/5)a_{B1}$. The contour of the unit-cell section by the $(1\ 0\ 4)_{C2/m} \equiv (2\ 0\ 1)_{B1}$ plane is also shown.
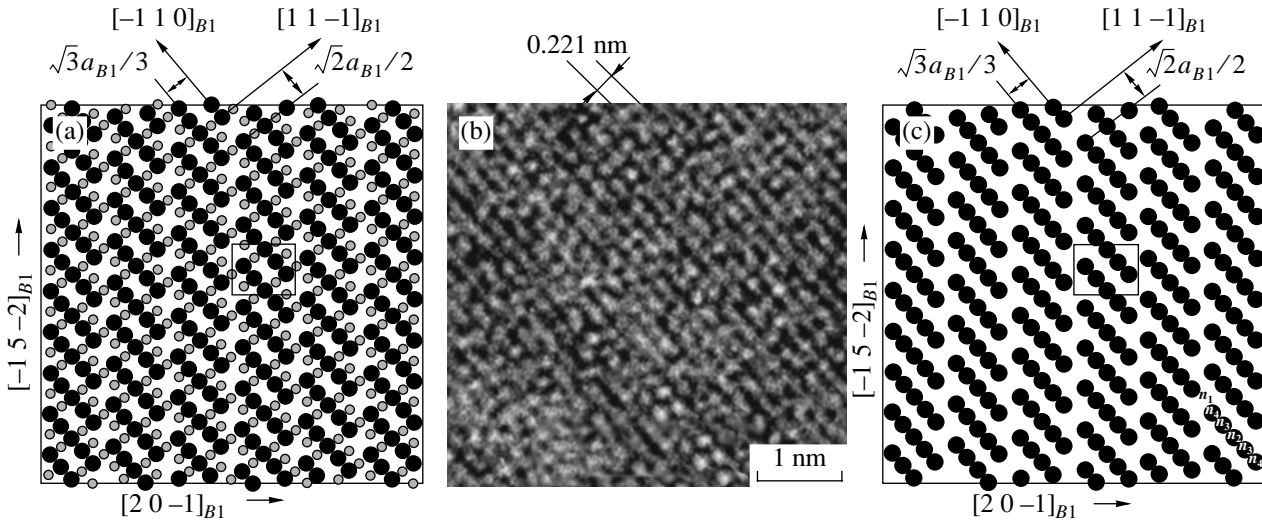


**Fig. 2.** Atomic and vacancy projections in the $[1\ 1\ 0]_{C2/m} \equiv [1\ 1\ -1]_{B1}$ direction onto the $(2\ 1\ -1)_{C2/m} \equiv (1\ 1\ -1)_{B1}$ plane of the ordered monoclinic $Ti_5O_5$ phase. The visible distance $d_{row}$ between the rows of like atoms is $(\sqrt{2}/4)a_{B1}$. The directions of vacancy channels are $[1\ 1\ 0]_{C2/m} \equiv [1\ 1\ -1]_{B1}$; the distance between the vacancy-separated atoms is $(\sqrt{6}/3)a_{B1}$. The contour of the unit-cell section by the $(2\ 1\ -1)_{C2/m} \equiv (1\ 1\ -1)_{B1}$ plane is also shown.

that three of them are most favorable for experimental observation: $[1\ 0\ 1]_{C2/m} \equiv [2\ 0\ 1]_{B1}$ (Fig. 1), $[1\ 1\ 0]_{C2/m} \equiv [1\ 1\ -1]_{B1}$ (Fig. 2), and $[0\ 1\ 1]_{C2/m} \equiv [1\ 1\ 2]_{B1}$ (Fig. 3a). The visible distances between the atomic rows and between the atoms in the rows are the largest for these directions. To imagine how the atomic and vacancy distributions appear in the section perpendicular to the chosen direction, the atomic and vacancy projections onto the planes perpendicular to this direction in an ideal completely ordered monoclinic phase $Ti_5O_5$ were determined for each of the indicated directions. The unfilled sites in the projection correspond to the vacancy channels.

The vacancy channels in the $[1\ 0\ 1]_{C2/m} \equiv [2\ 0\ 1]_{B1}$ direction perpendicular to the family of $(1\ 0\ 4)_{C2/m}$ planes (Fig. 1) or in the $[1\ 1\ 0]_{C2/m} \equiv [1\ 1\ -1]_{B1}$ direction perpendicular to the $(2\ 1\ -1)_{C2/m}$ planes (Fig. 2) are channels of the second type; they pass through the sequentially alternating nonmetallic and metallic vacancies. The third vacancy-channel direction is $[0\ 1\ 1]_{C2/m} \equiv [1\ 1\ 2]_{B1}$; i.e., it is a normal to the family of $(-1\ 1\ 4)_{C2/m}$ planes (Fig. 3a). In this case, the vacancy channel of the first type passes through the empty sites of either the metallic or the nonmetallic sublattice. The

directions of atomic rows, the visible distances $d_{row}$ between the rows of like atoms, and the visible distances between two vacancy-separated atoms are given in Figs. 1, 2, and 3a.

The visible distance between two vacancy-separated atoms is maximal for the atomic planes $(2\ 1\ -1)_{C2/m}$ observed in the $[1\ 1\ 0]_{C2/m} \equiv [1\ 1\ -1]_{B1}$ direction (Fig. 2); it is equal to $(\sqrt{6}/3)a_{B1}$, or 0.3408 nm for $a_{B1} = 0.4174$ nm. In the two other directions, the visible distances between the vacancy-separated atoms are smaller and are equal to $(\sqrt{2}/2)a_{B1} = 0.2951$ nm for the $[0\ 1\ 1]_{C2/m} \equiv [1\ 1\ 2]_{B1}$ direction (Fig. 3a) and $(\sqrt{5}/5)a_{B1} = 0.1867$ nm for the $[1\ 0\ 1]_{C2/m} \equiv [2\ 0\ 1]_{B1}$ direction (Fig. 1). Thus, the $[1\ 1\ 0]_{C2/m} \equiv [1\ 1\ -1]_{B1}$ direction is most suitable for the direct observation of vacancies by high-resolution electron microscopy.

The visible distance $d_{row} = d_{Ti-Ti} \equiv d_{O-O}$ between rows of like atoms is maximal if the atoms and vacancies in the ordered $Ti_5O_5$ phase are projected in the $[0\ 1\ 1]_{C2/m} \equiv [1\ 1\ 2]_{B1}$ direction onto the $(-1\ 1\ 4)_{C2/m} \equiv (1\ 1\ 2)_{B1}$ plane perpendicular to the projection direction (Fig. 3a); in this case, $d_{row} = (\sqrt{3}/3)a_{B1}$, or 0.2410 nm

**Fig. 3.** Distribution of the structural vacancies and the Ti and O atoms in the $[0\ 1\ 1]_{C2/m} \equiv [1\ 1\ 2]_{B1}$ direction with respect to the unit cell of the ordered monoclinic (space group $C2/m$) $Ti_5O_5$ oxide (atomic and vacancy projections in the $[0\ 1\ 1]_{C2/m} \equiv [1\ 1\ 2]_{B1}$ direction onto the $(-114)_{C2/m} \equiv (112)_{B1}$ plane): (a) computer simulation with both Ti and O atoms; (b) experimental high-resolution pattern ($4 \times 10^6$ magnification); and (c) computer simulation with only the Ti atoms (the order of alternation of the distribution function $n_{Ti}(\mathbf{r})$ is shown for the titanium sites in the $[-1\ 1\ 0]_{B1}$ rows). The visible model distance between rows of like atoms is $d_{row} = \sqrt{3}/3a_{B1} = 0.241$ nm (for $a_{B1} = 0.4174$ nm), and the experimental distance between the rows is $d_{row} = 0.221$ nm. The discontinuities between the atoms of the same row in the model drawings correspond to the vacancy channels in the $[0\ 1\ 1]_{C2/m}$ direction. The visible distance between the vacancy-separated atoms is $\sqrt{2}/2a_{B1} = 0.295$ nm. The contour of the unit-cell section by the $(-1\ 1\ 4)_{C2/m}$ plane is shown in the model drawings.

for $a_{B1} = 0.4174$ nm. If the atoms are projected in the $[1\ 0\ 1]_{C2/m} \equiv [2\ 0\ 1]_{B1}$ direction onto the plane of the $(1\ 0\ 4)_{C2/m} \equiv (2\ 0\ 1)_{B1}$ family, the visible distance is $d_{row} = a_{B1}/2$ and equals 0.2087 nm; for the projection in the $[1\ 1\ 0]_{C2/m} \equiv [1\ 1\ -1]_{B1}$ direction onto the $(2\ 1\ -1)_{C2/m} \equiv (1\ 1\ -1)_{B1}$ plane, it is equal to $(\sqrt{2}/4)a_{B1} = 0.1476$ nm. Therefore, the atomic rows are observed most distinctly in the $[0\ 1\ 1]_{C2/m}$ direction.

One of the experimental diffraction patterns of the ordered monoclinic (space group $C2/m$) $TiO_{1.087}$ monoxide is shown in Fig. 4; the direction of a normal pointed to the figure plane is $[0\ 1\ 1]_{C2/m} \equiv [1\ 1\ 2]_{B1}$. As was noted above, the visible distance between the rows of like atoms is the largest in this direction. In addition to the structural reflections (high-intensity spots), less intense superstructural reflections are seen from the twins that are present in the sample. In addition, a system of weak diffuse bands parallel to the $[[2\ 0\ -1]^*_{B1}$ and $[0\ 2\ -1]^*_{B1}$ directions, slightly shifted from the structural sites to the large-wavenumber region of the reciprocal space, is seen in the diffraction pattern. These bands form a system of geometrically similar parallelograms concentrically arranged near the parent (000) spot. None of the bands passes through the (000) site. The diffuse scattering of this type is primarily caused by the static displacements of atoms surrounding vacancies and by the correlative short-range order. The diffuse scattering bands were observed earlier [12]

in the diffraction pattern of the superstoichiometric cubic niobium nitride $NbN_{1.2}$ with vacancies in the niobium sublattice.

A high-resolution experimental pattern ($4 \times 10^6$ magnification) obtained for the ordered monoclinic (space group $C2/m$) $TiO_{1.087}$ sample studied by electron diffraction (Fig. 4) is presented in Fig. 3b. The image was obtained in the $(-1\ 1\ 4)_{C2/m} \equiv (1\ 1\ 2)_{B1}$ plane perpendicular to the $[0\ 1\ 1]_{C2/m} \equiv [1\ 1\ 2]_{B1}$ direction; the atomic rows are clearly seen in the image.

Since the thickness of the sample under study was about 50 nm, the pattern is a superposition of several tens of layers; in the observed area, atoms are arranged in well-defined rows only in the $[-1\ 1\ 0]_{B1}$ direction. The atomic chains in the row are disrupted; the discontinuity sites correspond to vacancies, but their arrangement is not perfectly periodic. The regions with a dark background in the microphotograph (Fig. 3b) correspond to larger sample thickness. The oxygen atoms are not seen in the experimental pattern (Fig. 3b), because their scattering factor is three times smaller than the scattering factor of the titanium atoms. For comparison, the pattern obtained by computer simulation with inclusion of only titanium atoms is presented in Fig. 3c; it better fits the real experimental pattern that is shown in Fig. 3b. In the general case, the distribution function $n_{Ti}(\mathbf{r})$ (1) takes four values that are equal to the probability of finding Ti atom at the sites of titanium fcc sublattice in the $TiO_y \equiv Ti_xO_z$ ($y = z/x$) monoxide: $n_{Ti1} =$
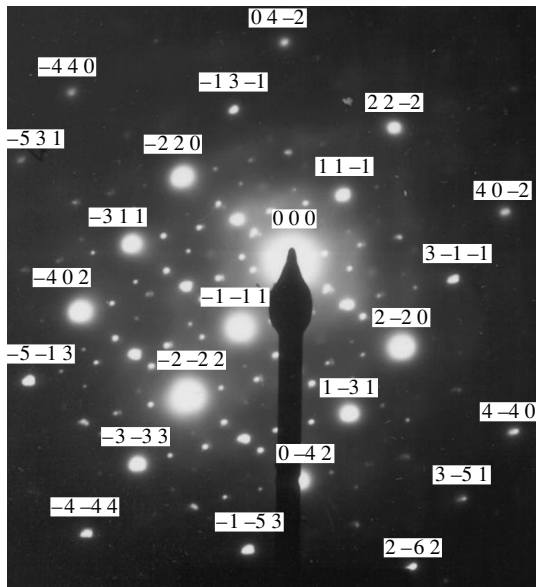
**Fig. 4.** Electron diffraction by the ordered monoclinic titanium monoxide $TiO_{1.087}$ (space group $C2/m$) with the parameter $a_{B1} = 0.4174$ nm of the basis crystal lattice (electron beam direction $[0\ 1\ 1]_{C2/m} \equiv [1\ 1\ 2]_{B1}$). The structural reflections are labeled indices of the basis $B1$ structure; the remaining reflections are due to the presence of superstructure and to the twinning of the basis cubic phase.

$x - \eta_{10}/6 - \eta_4/3 - \eta_1/3$, $n_{Ti2} = x + \eta_{10}/6 - \eta_4/3 + \eta_1/3$, $n_{Ti3} = x - \eta_{10}/6 + \eta_4/6 + \eta_1/6$, and $n_{Ti4} = x + \eta_{10}/6 + \eta_4/6 - \eta_1/6$. The value of $n_{Ti1}$ corresponds to the vacancy site in the titanium sublattice. One can see from Fig. 3c that the probabilities in the titanium rows alternate in the $[-1\ 1\ 0]_{B1}$ direction in the following order: $n_1, n_4, n_3, n_2, n_3, n_4, n_1, \dots$ . In the model image, every five titanium atoms are separated by the metallic structural vacancy (the probability of finding titanium atom equals $n_1$). Although the alternation of atoms and vacancies in the experimental image is not strictly periodic, it is similar, on the whole, to the model alternation. The periodicity in atomic rows can be interrupted by a combination of several factors: (i) the composition of the experimentally studied $TiO_{1.087}$ monoxide is different from the equiatomic composition of the titanium monoxide $TiO_{1.00}$ ($Ti_{0.833}O_{0.833}$), which can form an ideal ordered phase; (ii) the degree of long-range ordering in the titanium sublattice of the sample studied is not maximal; and (iii) apart from the long-range order, the ordered titanium monoxide under study possesses the short-range order due to the static relaxational displacements of atoms near the structural vacancies, as well as the correlative [1, 11, 13, 14] short-range order. Note that none of these factors can individually interrupt the periodicity in the arrangement of vacancy channels.

Thus, structural vacancies can be directly observed using high-resolution transmission electron micros-

copy. The ordered titanium monoxide $TiO_{1.087}$ having monoclinic $Ti_5O_5$ superstructure (space group $C2/m$) was used as the object of investigation. The observation of structural vacancies in $TiO_{1.087}$ with a magnification of $4 \times 10^6$ became possible due to the ordering and ensuing formation of continuous vacancy channels, as well as to the special sample orientation for which the electron beam and vacancy channel directions coincided.

REFERENCES

1. A. I. Gusev, A. A. Rempel, and A. A. Magerl, *Disorder and Order in Strongly Nonstoichiometric Compounds: Transition Metal Carbides, Nitrides and Oxides* (Springer, Berlin, 2001).

2. J. Murray and H. A. Wriedt, Bull. Alloy Phase Diagrams **8**, 148 (1987).

3. A. A. Valeeva, A. A. Rempel, and A. I. Gusev, Pis'ma Zh. Éksp. Teor. Fiz. **73**, 702 (2001) [JETP Lett. **73**, 621 (2001)].

4. D. Shindo and K. Hiraga, *High-Resolution Electron Microscopy for Materials Science* (Springer, Berlin, 1998).

5. A. A. Valeeva, A. A. Rempel, and A. I. Gusev, Neorg. Mater. **37**, 716 (2001).

6. D. Watanabe, J. R. Castles, A. Jostson, and A. S. Malin, Nature **210**, 934 (1966); Acta Crystallogr. **23**, 307 (1967).

7. E. Hilti and F. Laves, Naturwissenschaften **55**, 131 (1968).

8. D. Watanabe, O. Terasaki, A. Jostsons, and J. R. Castles, *The Chemistry of Extended Defects in Non-Metallic Solids*, Ed. by L. Eyring and M. O. Keeffe (North-Holland, Amsterdam, 1970).

9. A. W. Vere and R. E. Smallman, *Mechanism of Phase Transformation in Crystalline Solids* (Inst. of Metals, London, 1969).

10. H. Terauchi, J. B. Cohen, and T. B. Reed, Acta Crystallogr. A **34**, 556 (1978).

11. A. I. Gusev and A. A. Rempel, *Nonstoichiometry, Disorder, and Order in Solids* (Ural. Otd. Ross. Akad. Nauk, Ekaterinburg, 2001).

12. E. V. Shalaeva, B. V. Mitrofanov, and G. P. Shveikin, Phys. Status Solidi A **154**, 505 (1996).

13. A. A. Rempel and A. I. Gusev, Fiz. Tverd. Tela (Leningrad) **32**, 16 (1990) [Sov. Phys. Solid State **32**, 8 (1990)].

14. A. A. Rempel and A. I. Gusev, Phys. Status Solidi B **160**, 389 (1990).

*Translated by V. Sakun*

# Spin Relaxation in a Two-Electron Quantum Dot[¶]

## S. Dickmann[1, 2] and P. Hawrylak[3]

[1] *Institute for Solid State Physics, Russian Academy of Sciences, Chernogolovka, Moscow region, 142432 Russia*
[2] *Max-Planck-Institut für Physik Komplexer Systeme, D-01187 Dresden, Germany*
[3] *Institute for Microstructural Science, National Research Council, Ottawa, K1A 0R6 Canada*

Received November 28, 2002

We discuss the rate of relaxation of the total spin in a two-electron droplet in the vicinity of the magnetic-field-driven singlet–triplet transition. The total spin relaxation is attributed to spin–orbit and electron–phonon interactions. The relaxation process is found to depend on the spin of ground and excited states. This asymmetry is used to explain puzzles in recent high source–drain transport experiments. © 2003 MAIK "Nauka/Interperiodica".

PACS numbers: 73.21.La

The electronic structure of artificial atoms in quantum dots (QDs) [1] can be directly studied in transport measurements. Such voltage-tunable experiments in a varying magnetic field (e.g., see [1–7] and the works cited therein) enable researchers to change the number of electrons confined in a QD, as well as the mutual arrangement of electronic energy levels. The arrangement of levels depends on the total spin of electronic configurations [3, 4]. The application of the magnetic field induces transitions in the ground state between states characterized by different total spin. In this paper, we focus on the role played by total spin in the simplest system, a two-electron droplet. At low magnetic fields, the ground state is a singlet with total spin $S = 0$, while at higher magnetic fields the ground state is a triplet with total spin $S = 1$, in analogy to the parahelium–orthohelium transition, already studied theoretically in [4, 8]. Both singlet and triplet states and the singlet–triplet (ST) transition have been observed experimentally in both vertical [2, 6] and lateral QDs [5, 7]. However, while at least one of the triplet excited states is observed for magnetic fields below the ST transition, the singlet excited state is not seen past the ST transition, resulting in asymmetric (in $B$) source–drain transport spectra. In the present work, we present model calculations of total spin relaxation due to the mixture of spin–orbit (SO) and electron–phonon interaction, which helps to explain the unusual behavior of the levels associated with the different total spin seen in transport experiments.

We start with the SO interaction Hamiltonian for a two-dimensional (2D) electron in a quantum well, written as [9–13]

$$H_{SO} = \alpha(\mathbf{k} \times \hat{\boldsymbol{\sigma}})_z - \beta(\bar{\mathbf{k}} \cdot \hat{\boldsymbol{\sigma}}), \qquad (1)$$

where the layer plane is determined by the principal axes $(x, y)$ of the crystal. This expression is a combination of the Rashba term [14] (with the coefficient $\alpha$) and a 2D analogue of the Dresselhaus term (with the coefficient $\beta$) [10, 11]. We use the following notations: $\mathbf{k} = -i\nabla + e\mathbf{A}/c$ and $\bar{\mathbf{k}} = (k_x, -k_y)$ are 2D vectors; $\hat{\sigma}^{x, y}$ are the Pauli matrices. The $\beta$ coefficient is determined by the formula [10, 11]

$$\beta = \gamma_{so}\frac{\hbar}{\sqrt{2m^*G}}\mathrm{Ry}^* a_0^2/d^2 \equiv \mathcal{B}\,\mathrm{Ry}^* a_0^3/d^2, \qquad (2)$$

where $G$ is the band-gap width of the semiconductor, $\gamma_{so}$ is the spin–orbit constant [15], and $a_0 = \hbar^2\varepsilon/m^*e^2$ is the effective Bohr radius. (For GaAs: $G = 1.52$ eV, $\gamma_{so} = 0.07$, $a_0 = 9.95$ nm, $\mathrm{Ry}^* \approx 5.74$ meV, $m^* = 0.067m_e$, and $\mathcal{B} = 0.0043$.) The parameter $d$ is determined by averaging the square of the wave-vector $\hat{z}$ component of a 2D electron in the layer: $d^{-2} = -\langle f|d^2/dz^2|f\rangle$, where $f(z)$ is the corresponding size-quantized function. (In the well, we consider that $f = (2/\pi)^{1/4}e^{-z^2/d^2}/\sqrt{d}$.)

The Hamiltonian of the system of two interacting electrons in the harmonic potential $\frac{1}{2}m^*\omega_0^2(x^2 + y^2)$ may be written in center-of-mass (CM) and relative coordinates as $\mathcal{H} = H_m(\mathbf{r}) + \mathcal{H}_M(\mathbf{R}) + \mathcal{H}_S$. Here, $\mathbf{R} = (\mathbf{r}_1 + \mathbf{r}_2)/2$ and $\mathbf{r} = \mathbf{r}_1 - \mathbf{r}_2$ are CM and relative (Jacobi) coordinates of two particles. The first term in the Hamiltonian is

$$H_m = -\frac{\hbar^2}{2\mu}\left(\frac{\partial^2}{\partial r^2} + \frac{1}{r}\frac{\partial}{\partial r} - \frac{m^2}{r^2}\right)$$
$$-\frac{\hbar}{2}\omega_c m + \frac{\mu r^2\omega_0^2}{2}\left(1 + \frac{h^2}{4}\right) + e^2/\varepsilon r \qquad (3)$$

(here, $\omega_c = eB/m^*c$; $\mu = m^*/2$ is the reduced mass and $h = \omega_c/\omega_0$ is the dimensionless magnetic field). The expression for $\mathcal{H}_M(\mathbf{R})$ may be found from Eq. (3) for $H_m$ after the substitution $\mathbf{r} \longrightarrow \mathbf{R}$, $\mu \longrightarrow \mathcal{M} = 2m^*$, $m \longrightarrow M$, and $\varepsilon \longrightarrow \infty$.

The term $\mathcal{H}_S$ is the spin-dependent part of the Hamiltonian, namely, a combination of the Zeeman and spin–orbit coupling terms: $\mathcal{H}_S = \sum_{i=1,2}[|g\mu_B B|\hat{\sigma}_i^z + H_{SO}^{(i)}]$. For two electrons, the SO part $H_{SO}^{(1)} + H_{SO}^{(2)}$ can also be written in CM and relative coordinates $\mathbf{R}$ and $\mathbf{r}$. Denoting $\hat{\boldsymbol{\Sigma}} = \hat{\boldsymbol{\sigma}}_1 + \hat{\boldsymbol{\sigma}}_2$, $\hat{\boldsymbol{\sigma}} = \hat{\boldsymbol{\sigma}}_1 - \hat{\boldsymbol{\sigma}}_2$, we obtain

$$\mathcal{H}_S = (H_{RSO} + H_{rSO}) + g\mu_B B\hat{\Sigma}_z, \qquad (4)$$

where

$$H_{RSO} = -D_+(\alpha\hat{\Sigma}_- + i\beta\hat{\Sigma}_+) - D_-(\alpha\hat{\Sigma}_+ - i\beta\hat{\Sigma}_-),$$

and

$$H_{rSO} = -\partial_+(\alpha\hat{\sigma}_- + i\beta\hat{\sigma}_+) - \partial_-(\alpha\hat{\sigma}_+ - i\beta\hat{\sigma}_-). \qquad (5)$$

The new operators are

$$D_\pm = \mp\frac{1}{2}\left(\frac{\partial}{\partial X} \pm i\frac{\partial}{\partial Y}\right) + b(X \pm iY),$$

$$\partial_\pm = \mp\left(\frac{\partial}{\partial x} \pm i\frac{\partial}{\partial y}\right) + \frac{b}{2}(x \pm iy)$$

[$(X, Y)$ and $(x, y)$ are the components of 2D vectors $\mathbf{R}$ and $\mathbf{r}$], $b = m^*\omega_c/2\hbar$, and

$$\hat{\Sigma}_\pm = \frac{1}{2}(\hat{\Sigma}_x \pm i\hat{\Sigma}_y), \quad \hat{\sigma}_\pm = \frac{1}{2}(\hat{\sigma}_x \pm i\hat{\sigma}_y).$$

The wave function of the two-electron system may be written in the form $\Psi_M(R)e^{iM\Phi}\psi_m(r)e^{im\phi}\chi_{\sigma_1,\sigma_2}$, where $\sigma_1$ and $\sigma_2$ are the spin variables of the electrons. We expand the wave function in the basis set of the singlet and triplet states

$$|s\rangle = \Psi_0(R)\psi_0(r)|0, 0\rangle$$

$$\text{and } |t, S_z\rangle = \Psi_0(R)\psi_1(r)e^{i\phi}|1, S_z\rangle \quad (S_z = 0, \pm 1). \qquad (6)$$

Here, $\Psi_0$ is the ground-state function (i.e., it obeys the equation $\mathcal{H}_0\Psi_0 = \hbar\omega_0\sqrt{1 + h^2/4}\,\Psi_0$), while the functions $\psi_{0,1}$ have to be found from the equations

$$H_m\psi_m = E_m\psi_m. \qquad (7)$$

The analytical solution of Eq. (7) could be found if $l = \sqrt{\hbar/m^*\omega_0}\,(h^2 + 4)^{-1/4} \ll a_0$ or $l \gg a_0$. The $l \ll a_0$ case has been studied perturbatively in [8]. Here we consider

the opposite limit $l \gg a_0$ (this seems to be more relevant to a typical experimental situation). Then, in the leading approximation, the solutions of Eqs. (7) are the states of a one-dimensional oscillator with mass $\mu$ and frequency $\omega_0\sqrt{3 + 3h^2/4}$ localized in the vicinity of $r_0 = [2l_0^4/a_0(1 + h^2/4)]^{1/3} \gg l_0$ (here we have designated $l_0 = \sqrt{\hbar/m^*\omega_0}$). In this approximation, the energy measured from the ground state is

$$\delta_{m, S_z} = E_m - E_0$$
$$= \frac{\hbar^2 m^2}{r_0^2 m^*} - \frac{\hbar}{2}\omega_c(m + g^*S_z) \equiv \frac{\hbar\omega_0}{4}D_{m, S_z}(h) \qquad (8)$$

($g^* = gm^*/m_e \approx 0.029$). The equation determining the ST crossing thereby takes the form $\delta_{1, S_z} = 0$ (if $a_0/l_0 = 1/3$, then for the ST crossing point we obtain $h = 0.64$ at $S_z = 0$, whereas, for the same $a_0/l_0$ and $S_z$, the exact numerical calculation [8] gives $h = 0.69$).

We now turn to the effect of SO interaction on the mixing of singlet and triplet states. Operators $\Sigma_\pm$ and $\Sigma_z$ commute with $\boldsymbol{\Sigma}^2$; therefore, the first and third terms in Eq. (4) are not responsible for mixing of the singlet and triplet states. On the contrary, the second term in Eq. (4) results in this mixing. Indeed, let $|S, S_z\rangle$ be the normalized spin states of two electrons. When operating on the state $|0, 0\rangle$, the term $H_{rSO}$ yields the following nonzero matrix elements: $\langle 1, 1|H_{rSO}|0, 0\rangle$ and $\langle 1, -1|H_{rSO}|0, 0\rangle$. (One can check that $\hat{\sigma}_\pm|0, 0\rangle = \mp 2^{-1/2}|1, \pm 1\rangle$.)

Hence, we see immediately that the $|0, 0\rangle$ singlet state is mixed with the $|1, \pm 1\rangle$ triplet states but not with the $|1, 0\rangle$ state. This state is therefore long-lived.

For the states that are coupled, the expansion in terms of the small parameter $a_0/l_0$ leads to the following result for the mixing matrix element between $|s\rangle$ and $|t, 1\rangle$ states:

$$M_{SO} = \langle s|H_{rSO}|t, 1\rangle$$
$$\approx -\frac{i\beta}{2^{3/2}}\left(\frac{1}{r_0} + br_0\right) \equiv -\frac{i\beta}{2^{3/2}l_0}\mathcal{L}(h). \qquad (9)$$

If we take into account the Rashba term, we find that another nonzero matrix element is $\langle s|H_{rSO}|t, -1\rangle$; however, the state $|t, 0\rangle$ is never mixed with the singlet. Further, we neglect the Rashba coupling (usually there is $\alpha < \beta$ in GaAs heterostructures; in any case, $\alpha$ vanishes in the case of an ideally symmetric quantum well).

Using Eq. (9), we find the hybridized states $|S\rangle = C_0^-|s\rangle + C_1^-|t, 1\rangle$, and $|T\rangle = C_0^+|s\rangle + C_1^+|t, 1\rangle$, where

$$C_0^{\pm} = \left\{ \frac{M_{SO}}{2|M_{SO}|} \left[ 1 \mp \frac{\delta_{1,1}}{\delta E} \right] \right\}^{1/2},$$

$$C_1^{\pm} = \pm\left\{ \frac{M_{SO}}{2|M_{SO}|} \left[ 1 \pm \frac{\delta_{1,1}}{\delta E} \right] \right\}^{1/2} \tag{10}$$

($\delta E = \sqrt{\delta_{1,1}^2 + 4|M_{SO}|^2}$). The corresponding energies are $E_{T/S} = E_0 + (\delta_{1,1} \pm \delta E)/2$.

The next step in our study is the calculation of the $|T\rangle \longrightarrow |S\rangle$ (or $|S\rangle \longrightarrow |T\rangle$) relaxation rate for the case where $\delta_{1,1} > 0$ (or $\delta_{1,1} < 0$). Evidently, the main relaxation channel is determined by emission of the acoustic phonon with energy $\hbar c_s k = \delta E$, where $\mathbf{k} = (\mathbf{q}, k_z)$ is the phonon wave vector and $c_s$ is the mean sound velocity (we use the so-called isotropic model, i.e., $c_s$ does not depend on the polarization and on the $\mathbf{k}$ direction; we consider that $c_s = 3.37 \times 10^5$ cm/s). The probability of this event is determined by

$$\frac{1}{\tau} = \sum_{\mathbf{q}, k_z} \frac{2\pi |\mathcal{M}(\mathbf{q}, k_z)|^2}{\hbar} \delta(\hbar c_s k - \delta E), \tag{11}$$

where $\mathcal{M}(\mathbf{q}, k_z)$ is the appropriate matrix element

$$\mathcal{M}(\mathbf{q}, k_z) = \langle T|U_{\text{e-ph}}|S\rangle$$
$$= C_0^{+*} C_0^- (\langle s|U_{\text{e-ph}}|s\rangle - \langle 1, t|U_{\text{e-ph}}|t, 1\rangle). \tag{12}$$

Here, the phonon field is averaged over the angle $\phi = r \wedge q$:

$$U_{\text{e-ph}}(\mathbf{R}, r) = \left(\frac{\hbar}{V}\right)^{1/2} \sum_s \tilde{U}_s(\mathbf{q}, k_z) e^{i\mathbf{q}\mathbf{R}} \overline{(e^{i\mathbf{q}r} + e^{-i\mathbf{q}r})}$$
$$= 2\left(\frac{\hbar}{V}\right)^{1/2} \sum_s \tilde{U}_s(\mathbf{q}, k_z) e^{i\mathbf{q}\mathbf{R}} J_0(qr) \tag{13}$$

[$s$ is the polarization, $V$ is the sample volume, and $\tilde{U}_s(\mathbf{q}, k_z)$ is the renormalized vertex, which includes the deformation and piezoelectric fields created by the phonon]. The integration with respect to $z$ has already been performed and reduces to the renormalization $\tilde{U}_s = U_s(\mathbf{q}, k_z)F(k_z)$, where the formfactor is $F(k_z) = \langle f|e^{ik_z z}|f\rangle$. By using Eqs. (6) and (12) and the expansion $J_0(qr) \approx J_0(qr_0) - q(r - r_0)J_1(qr_0)$, we obtain the matrix element (12), and, after the substitution into

Eq. (11), we find that the relaxation rate is proportional to $\left|\sum_s U_s\right|^2$. The latter is represented as [12]

$$\left|\sum_s U_s(\mathbf{q}, k_z)\right|^2 = \frac{\pi\hbar c_s k}{p_0^3 \tau_A},$$
$$\text{where } \frac{1}{\tau_A(\mathbf{k})} = \frac{1}{\tau_D} + \frac{5p_0^2}{k^6\tau_P}(q^2 k_z^2 + q_x^2 q_y^2). \tag{14}$$

The summation involves averaging over the directions of the polarization unit vectors for both components of the electron–phonon interaction. The nominal times for the deformation and piezoelectric interactions in GaAs are $\tau_D \approx 0.8$ ps and $\tau_P \approx 35$ ps [12, 16]. The nominal momentum is $p_0 \approx 2.52 \times 10^6$/cm [16]. We also refer to [12, 16] for details concerning the meaning and the expressions of these values in terms of the GaAs material parameters.

Finally, using Eqs. (2), (9), (10), (12)–(14), and (11), we calculate the relaxation time

$$1/\tau(h) = \mathcal{W}\mathcal{E}\mathcal{L}^2 \exp(-\mathcal{A}\mathcal{E}^2)\mathcal{I},$$

where

$$\mathcal{W} = \frac{\pi(\text{Ry})^3 a_0^{10} \mathcal{B}^2}{216(\hbar c_s)^3 p_0 \tau_P l_0^4 d^4},$$

$$\mathcal{E}(h) = \frac{4\delta}{\hbar\omega_0} = \sqrt{\mathcal{D}_{1,1}^2(h) + 2[\mathcal{B}a_0 l_0 \mathcal{L}(h)/d^2]^2}$$

[see the definitions for $\mathcal{L}$ and $\mathcal{D}_{1,1}$ in Eqs. (8), (9)],

$$\mathcal{A} = \left(\frac{da_0^2 \text{Ry}}{4l_0^2 \hbar c_s}\right)^2,$$

$$\mathcal{I}(h) = \int_0^1 \frac{d\xi\xi}{\sqrt{1-\xi}} \{J_1[\mathcal{R}(\xi)]\}^2$$

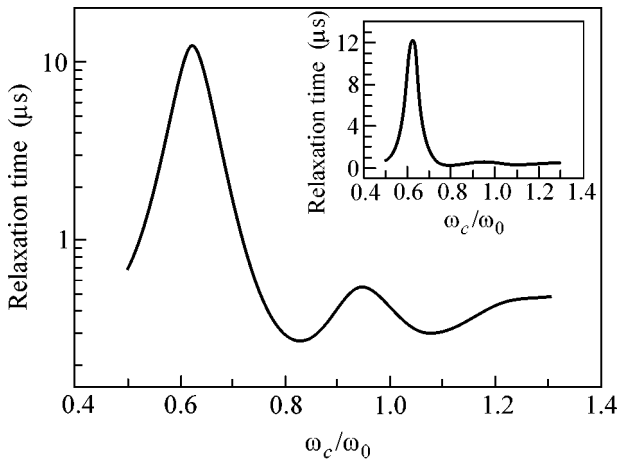$$\times \left[5\xi - \frac{35}{8}\xi^3 + \mathcal{S}\mathcal{E}^2(h)\right] e^{-\xi\mathcal{P}(h)},$$

$$\mathcal{R}(\xi) = a_0 \text{Ry}/\hbar c_s (a_0/l_0)^{2/3} \sqrt{\xi}\mathcal{E}(h)(4 + h^2)^{-1/3},$$

$$\mathcal{S} = (\tau_P/\tau_D)(a_0^2 \text{Ry}/2l_0^2 \hbar c_s p_0)^2,$$

and

$$\mathcal{P}(h) = \left[a_0^2/l_0^2 \sqrt{4 + h^2} - \frac{1}{2}(da_0/l_0^2)^2\right]$$

$$\times [\mathcal{E}(h)a_0 \text{Ry}]^2/8(\hbar c_s)^2.$$

As an illustration, the figure shows the relaxation rate as a function of the magnetic field on the logarithmic scale (the main picture) and on the usual scale (the inset). The relaxation time is seen to have a sharp maximum in the

The ST relaxation time $\tau$ calculated for $a_0/l_0 = 1/3$ and $d = 5$ nm. The maximum corresponds to ST transition at $\omega_c/\omega_0 = 0.64$. See the text for details.

vicinity of the ST crossing but constitutes a comparatively small value (of the order of 0.1 μs) in the regions where the singlet and triplet lines are resolved. The nonmonotonic behavior of $\tau$ to the right of the ST crossing originates from the correlations between the wavefunction characteristic distance $r_0$ and the wavelength $\hbar c_s/\delta E$ of the emitted phonon.

We now turn to the discussion of the manner in which the ST relaxation could influence the transport spectroscopy through the QD states. By studying the kinetic processes of filling and emptying the dot in the presence of a large "source–drain" voltage, we estimate the effective electron lifetime inside the dot at the "working level," i.e., at the level which participates in the transport through the dot. This effective lifetime $\tau_{dot}$ under the experimental conditions of [6, 7] we estimate to be on the order of 1 μs, and this value should evidently be compared with the ST relaxation time calculated above. If the working level is exactly the upper level of the two-electron droplet, then the relaxation could influence the current. Namely, if $\tau < \tau_{dot}$, then the working level could be emptied due to the ST relaxation occurring within the dot. In this case, the current through the upper two-electron state becomes negligible. The relaxation process is asymmetric across the ST transition. Before the transition, the "working level" involves $|t, \pm 1\rangle$ and $|t, 0\rangle$ (6) triplet states. (The Zeeman splitting is not resolved.) The $|t, 0\rangle$ state is long-lived and hence is observed in experiment, while the $|t, 1\rangle$ state relaxes efficiently to the $S = 0$ singlet state $|s\rangle$. Past the ST transition, the $|t, 1\rangle$ state is the ground state, but the excited state is the singlet. The singlet state relaxes efficiently to the $|t, 1\rangle$ ground state. Hence, this asymmetry in the relaxation processes associated with the

singlet–triplet transition could be responsible for the anomalies observed in the transport experiments [6, 7].

In closing, it is worth mentioning other relaxation channels that are not taken into account in our calculation but that, in the framework of the considered mechanism, could additionally reduce the ST relaxation time. These are provided by special phonon modes (e.g., by surface and confinement phonons excited in the heterojunction) and certainly by the SO Rashba coupling if the latter is significant.

## REFERENCES

1. For reviews and references see L. Jacak, P. Hawrylak, and A. Wójs, *Quantum Dots* (Springer, Berlin, 1998); L. P. Kouwenhoven, C. M. Marcus, P. McEuen, *et al.*, in *Mesoscopic Electron Transport*, Ed. by L. L. Sohn, L. P. Kouwenhoven, and G. Schön (Kluwer Academic, Dordrecht, 1997), NATO ASI Ser., Ser. E, Vol. 345; R. C. Ashoori, Nature **379**, 413 (1996); M. Kastner, Phys. Today **46**, 24 (1993); T. Chakraborty, Comments Condens. Matter Phys. **16**, 35 (1992).

2. R. C. Ashoori, H. L. Stormer, J. S. Weiner, *et al.*, Phys. Rev. Lett. **71**, 613 (1993).

3. P. Hawrylak, C. Gould, A. S. Sachrajda, *et al.*, Phys. Rev. B **59**, 2801 (1999).

4. P. Hawrylak, Phys. Rev. Lett. **71**, 3347 (1993).

5. A. S. Sachrajda, P. Hawrylak, M. Ciorda, *et al.*, Physica E (Amsterdam) **10**, 493 (2001).

6. T. Fujisawa, D. G. Austing, Ya. Tokura, *et al.*, Nature **419**, 278 (2002).

7. J. Kyriakidis, M. Pioro-Ladriere, M. Ciorga, *et al.*, Phys. Rev. B **66**, 035320 (2002).

8. M. Wagner, U. Merkt, and A. V. Chaplik, Phys. Rev. B **45**, 1951 (1992).

9. T. Ando, A. B. Fowler, and S. Stern, Rev. Mod. Phys. **54**, 437 (1982).

10. M. I. D'yakonov and V. Yu. Kachorovskiĭ, Fiz. Tekh. Poluprovodn. (Leningrad) **20**, 178 (1986) [Sov. Phys. Semicond. **20**, 110 (1986)].

11. G. Bastard, Phys. Rev. B **46**, 4253 (1992).

12. S. M. Dikman and S. V. Iordanskiĭ, Zh. Éksp. Teor. Fiz. **110**, 238 (1996) [JETP **83**, 128 (1996)].

13. S. Dickmann, Phys. Rev. B **61**, 5461 (2000).

14. Yu. A. Bychkov and E. I. Rashba, Pis'ma Zh. Éksp. Teor. Fiz. **39**, 66 (1984) [JETP Lett. **39**, 78 (1984)].

15. G. E. Pikus and A. N. Titkov, in *Optical Orientation*, Ed. by F. Meier and B. P. Zakharchenya (North-Holland, Amsterdam, 1984), p. 73.

16. V. F. Gantmakher and Y. B. Levinson, *Carrier Scattering in Metals and Semiconductors* (Nauka, Moscow, 1984; North-Holland, Amsterdam, 1987).

# New Wannier–Stark Localization Effects in Natural 6H–SiC Superlattice

## V. I. Sankin*, P. P. Shkrebiĭ, N. S. Savkina, and N. A. Kuznetsov

*Ioffe Physicotechnical Institute, Russian Academy of Sciences, Politekhnicheskaya ul. 26, St. Petersburg, 194021 Russia*
*\* e-mail: sankin@pop.ioffe.rssi.ru*

A premature electric breakdown caused by the formation of a strong-field domain under conditions of negative differential conductivity in the 6H–SiC $n^+$–$n^-$–$n^+$ structure optimized for ultrahigh-frequency measurements was observed in the range of electric fields corresponding to the Bloch oscillation regime in a natural 6H–SiC superlattice. The experimental results and ensuing estimates indicate that this domain is mobile and, hence, oscillating, allowing the microwave oscillations that are rapidly damped under conditions of avalanche breakdown in a natural 6H–SiC superlattice to be forecasted. Crystal perfectness of a natural 6H–SiC superlattice made it possible to directly observe the Wannier–Stark localization up to electric breakdown, i.e., during the natural crystal lifetime. This was accomplished by the optical photoelectric transformation method in the multiplication regime for a photocurrent created by photons with above-bandgap energy. It was shown that the Wannier–Stark localization, which involves only electrons, occurs in natural 6H–SiC superlattice up to fields that are almost equal to the breakdown field in 6H–SiC, unresponsively to band mixing, i.e., to the fundamental destroyer of the Wannier–Stark localization. © 2003 MAIK "Nauka/Interperiodica".

PACS numbers: 73.21.Cd; 72.20.Ht

The theory of electrical conductivity in crystals [1, 2] predicts that, under the action of an increasing external uniform electric field $F$, the monotonic translational electron motion turns into oscillations at a certain $F$. This phenomenon was called Bloch oscillations (BOs) or Bragg reflection, by analogy with the well-known wave effect. In this case, the band spectrum splits into discrete levels, so-called Wannier–Stark ladders. The BO effect arises in a sufficiently strong field for which the following relations are fulfilled:

$$F \geq \hbar/ea\tau, \qquad (1)$$

$$leF \geq E_1. \qquad (2)$$

Here, $\hbar$ is Planck's constant, $e$ is electron charge, $a$ is lattice constant, $\tau$ is the scattering time, $l$ is the electron (hole) mean free path, and $E_1$ is the lower conduction band width. In the electric field satisfying Eqs. (1) and (2), an electron can ballistically reach, with some probability, the miniband edge to undergo Bragg reflection. Thereafter, the electron moves back in both $k$ and real spaces; this means, in fact, a decrease in current with a rise in electric field. In other words, negative differential conductivity (NDC) arises in the crystal. The electron becomes localized in a finite region whose size decreases with increasing field, and the quantization of its motion in this region gives rise to discrete energy levels separated by the energy $eFa$ (Stark splitting). This phenomenon is known as the Wannier–Stark localization (WSL). It follows that, to observe the BO effect in conventional semiconductors, where $E_1$ is as large as

several electron volts, crystal-destroying fields are required. For this reason, an effort was undertaken to prepare artificial crystals with a superlattice (SL) [3].

SLs based on a sequence of AlAs–GaAs heterojunctions and their modifications have gained the greatest acceptance. Since the SL spacing is larger than the base lattice spacing, while the conduction band is split into a set of narrow bands (minibands), the lowest of which may be as narrow as several tens of millielectron volts, the threshold field determined by Eqs. (1) and (2) will be substantially lower for the SL. The optical and electrical transport studies aimed at observing the above-mentioned effects were carried out mostly with the SLs of this type [4–10]. These studies can be briefly summarized as follows: certain WSL effects were observed in these SLs. However, their magnitudes were too small to be of practical importance. These effects are unique and attractive not only because of their fundamental nature, but also because they hold obvious practical promise by themselves. In turn, the practical significance of the observed effects would also be a strong argument in favor of the correctness of solutions [2] against the theoretical disproofs [11–13] that consider the WSL regime impossible because of the inevitable band mixing in an electric field and ensuing delocalization due to the change-carrier transfer to the upper bands.

Note, however, that the SLs with heterojunctions and, in particular, the AlAs–GaAs SL are not the only objects for such investigations. It was shown in a number of works [14–17] that the superstructural polytypic
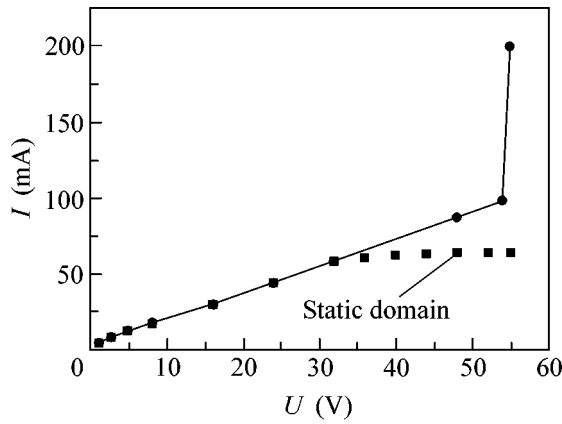
**Fig. 1.** Current–voltage characteristic of the 6H–SiC $n^+$–$n^-$–$n^+$ diode structure.



**Fig. 2.** General view of the 6H–SiC $n^+$–$n^-$–$n^+$ triode structure with a $p$–$n$ junction gate.

(hexagonal and rhombohedral) SiC crystals display in many experiments unique properties caused by the WSL and BO. Recall that the field in this case should be aligned with the SL axis, which coincides with the crystal axis. In [18–21], the Wannier–Stark resonances were observed with a rather high NDC, evidencing the development of the WSL process in these crystals from BO to the complete localization of the lower miniband and even to the electron delocalization through resonance tunneling.

In this work, new results on electric-field-induced electron localization in a natural superstructural 6H–SiC crystal are presented. Previous results [20] have shown that electron drift in a specially prepared triode structure displays pronounced NDC at a certain field satisfying Eq. (1). This result was obtained in the static measurement mode. Further analysis invoking experimental miniband-spectrum parameters such as $E_1$ and $E_{12}$ [20] showed that the NDC is, most likely, caused by the BO regime [21]. A further step in this direction consisted in the design of a new homogeneous diode structure with electron conductivity for the direct measurements of the current–voltage characteristics in fields ranging from 0 to 200 kV/cm, i.e., near the BO threshold fields obtained in [18]. Such an $n^+$–$n^-$–$n^+$ diode structure optimized for the ultrahigh-frequency measurements was fabricated by the epitaxial technique. On a highly doped Lely-type substrate, an epitaxial $n^-$ layer was formed with the extremely low concentration ($10^{15}$–$10^{16}$ cm$^{-3}$) of a residual donor impurity, in which the electric field was concentrated, while the upper highly doped contact $n^+$ layer was formed by ion-implantation doping. The geometric sizes of the mesa structure were $40 \times 3 \times 3$ μm. The current–voltage characteristic (CVC) of this structure (Fig. 1) shows no prominent features below a certain bias and is close to linear. Of interest is the curve portion where, at a certain bias, the current in the structure increases drastically
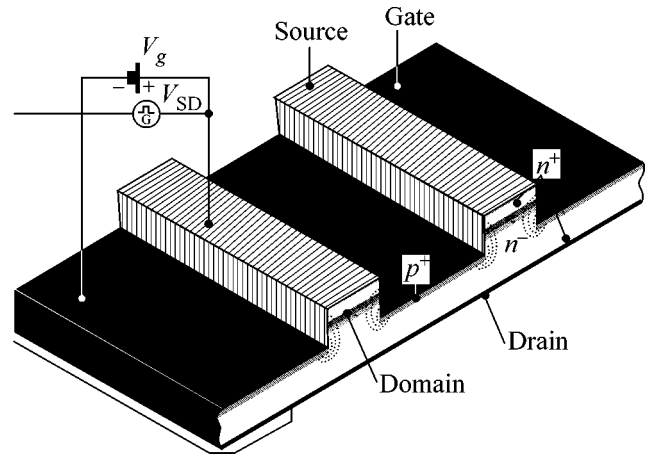
with light emission. The spectrum of this emission coincided with the emission spectrum of the $p$–$n$-junction breakdown. However, the strength of a uniform field did not exceed 150 kV/cm, which is lower, by more than 15 times, than the known lowest value of the breakdown field in 6H–SiC. Such a field deficiency can probably be overcome through the formation of a field domain in the base region. The formation of a field domain is known to be accompanied by the appearance of NDC in crystal [22]. According to the aforesaid, the NDC observed at 150 kV/cm in 6H–SiC was caused by the BO regime [18].

The answer to the question of whether the domain is static or mobile is of fundamental importance. If the domain is mobile, one should expect microwave generation. The CVC in Fig. 2 counts in favor of the latter. Indeed, in this particular case, the localized domain would have the width $d = U/F_{br}$. At $U = 50$ V and $F_{br} = 2000$ kV/cm one has $d \le 0.25$ μm. For the static domain, the CVC would show a plateau with the differential resistance $R = L^2/\varepsilon v S$, where $L$ is the width of the $n^-$ region, $\varepsilon$ is the dielectric constant of the semiconductor, $v$ is the saturated electron-drift velocity, and $S$ is the area of the $n^-$ region. For the unipolar diode $n^+$–$n^-$–$n^+$ structure of interest with $\varepsilon = 10^{-12}$ F/cm, $v = 2 \times 10^6$ cm/s, $L = 3$ μm, and $S = 1.3 \times 10^{-5}$ cm$^2$, the differential resistance $R$ is equal to $3 \times 10^3$ Ω (broken line in Fig. 4), whereas the differential resistance in the breakdown region is 10–20 Ω.

For a mobile domain, the electron–hole-pair generation rate in the breakdown region (on the assumption that the generation is uniform and that the recombination can be ignored because of a fast transit) would be $G = I/SqL$, giving $G = 1.2 \times 10^{26}$ cm$^{-3}$/s for $I = 100$ mA. The theoretical estimate of the generation rate can be made using Eq. (12b) from [23] for the mobile Gunn domains. Using $a_\alpha = 1 \times 10^6$ cm$^{-1}$ [16], $n_r = 10^{16}$ cm$^{-3}$, one obtains $G = 2 \times 10^{26}$ cm$^{-3}$/s. This can be considered
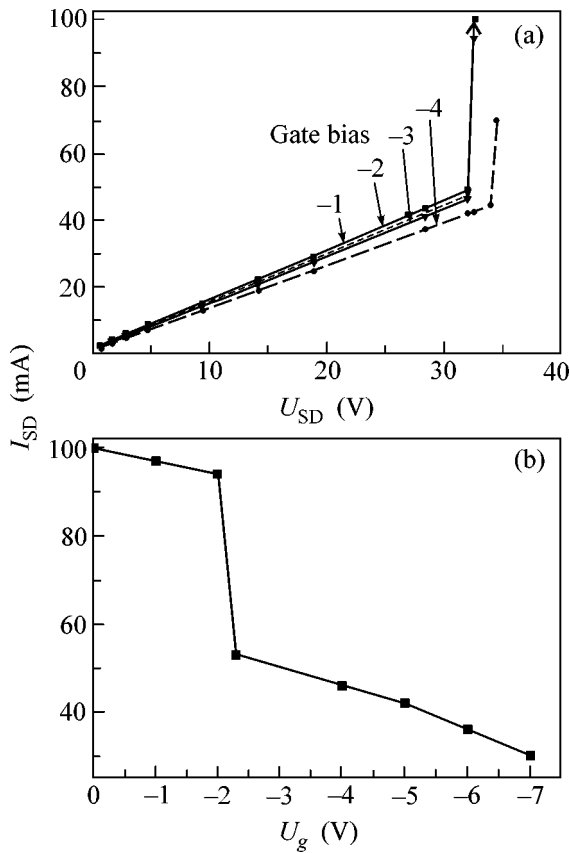
**Fig. 3.** Current–voltage characteristic of the 6H–SiC $n^+$–$n^-$–$n^+$ triode structure. (a) $J_{SD} \sim f(V_{SD})$ and (b) $J_{SD} \sim f(V_G)$.
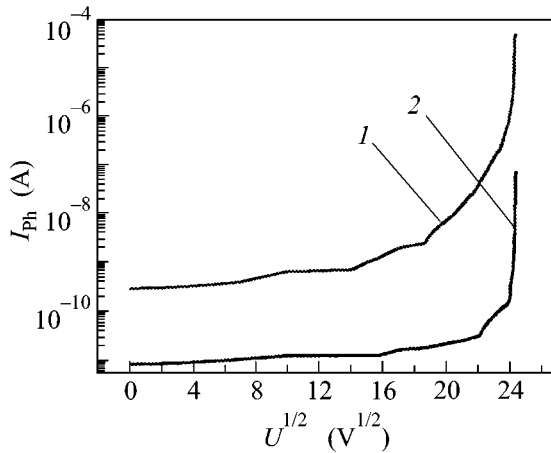


**Fig. 4.** Photocurrent in the 6H–SiC $p^+$–$n^-$–$n^+$ structure as a function of external voltage.

as a good agreement confirming the assumption about the mobile domain.

It is known that the action of an electric field on a dipole (domain in our case) brings about its transformation up to destruction. To verify this, a comb of diode structures similar to those considered above was fabricated, with a *p–n* junction built in between (Fig. 2). This structure is an analogue of a unipolar field-effect transistor (FET), and its operation is described using the appropriate terminology. The current $n^+$–$n^-$–$n^+$ channel with geometric sizes of $40 \times 3 \times 3$ μm is bounded on two sides by the *p–n*-junction fields whose directions have a component transverse to the current direction from the drain to the source in the channel. Experiment showed that the CVC of these channels (Fig. 3a) at the gate (*p–n* junction) bias $V_g = 0$ is similar to the CVC of the diode structure (Fig. 1). It was established experimentally that, at $V_g \neq 0$, the behavior of CVC in the linear region is drastically different from its behavior in the breakdown region. In the linear region, the behavior is typical of a FET: the current decreases with the slope $S = 2$–$4$ mA/V as the field at the gates increases, in accordance with the channel parameters. However, in the breakdown region, the current decreased, at a certain gate field, with the slope $S = 40$–$60$ mA/V (Fig. 3). Such a pronounced and sharp current drop can be explained by the domain destruction in an electric field directed perpendicular to the domain field. Naturally, the domain destruction is followed by the suppression of breakdown and a sharp decrease in current. This experimental finding is strong evidence of domain formation in the channel with natural SL. At the same time, one can conclude from the data obtained that the domain is mobile, because, according to geometric considerations, the gate field acts in the channel region, which is offset by about $2.0$ μm from the source, and cannot act on the static domain that is ordinarily localized near the source (cathode). Therefore, these results give new evidence of the occurrence of the BO regime in natural 6H–SiC SL.

We now turn to the new, from the viewpoint of our objective and the chosen method, study of WSL. It was pointed out in [21] that the natural silicon carbide SL is intrinsically built in a crystal; it has the same ideal crystal structure and, accordingly, creates the optimally favorable medium for the implementation of fine effects such as BO and all WSL effects altogether, which are quite sensitive to the presence of structural defects acting as charge-carrier scattering centers. For this reason, natural 6H–SiC SL can be used for the direct observation of induced localization up to the electric breakdown, i.e., during the crystal natural lifetime. The previous assumption [16] that only the electronic spectrum is quantized in silicon carbide SL can be verified by direct observation. The possibility of observing a nonquantized hole and quantized electronic components in the same sample under the same conditions drastically improves the unambiguity of interpretation. This problem can be implemented experimentally using the optical photoelectric transformation method in the multiplication regime for a photocurrent created by photons with the above-bandgap energy. This method allows one to use the internal field in the space-charge region (SCR) of the *p–n* junction and

change it by an external electric field to obtain, in high electric fields, comparatively low photocurrents controlled by the light incident on the surface of the $p–n$ junction. Due to this circumstance, sample destruction in the near-breakdown fields can be avoided. Either electrons or holes can mostly be injected into the strong-field region, depending on the experimental demands.

So, 6H–SiC-based $p^+–n^-–n^+$ structures were prepared for our study. In contrast to the structure described above, the upper aluminum-doped epitaxial $p^+$ layer was grown to the concentration of uncompensated acceptors on the order of $10^{18}$ cm$^{-3}$, and the residual donor concentration in the epitaxial $n$ layer ranged from $6 \times 10^{16}$ to $2 \times 10^{17}$ cm$^{-3}$. The electric field in the SCR varied following the law for an abrupt $p–n$ junction, namely, $F \sim (V_k + V)^{1/2}$, where $V_k = 2.9$ V is the contact potential and $V$ is the external voltage. The $p^+$-layer thickness and the photon energy were dictated by two requirements: (i) the number of photons absorbed in the $p^+$ layer be minimal and (ii) photon absorption in the $p^+$ layer be as complete as possible. In the first case, light is mostly absorbed in the SCR and the $n^-$ layer. Holes diffuse from the $n^-$ layer first to the SCR and then to the multiplication layer, where the carriers acquire additional energy under the action of a strong field to create new carriers in the collisions with lattice atoms. Depending on the efficiency of energy transfer from the field to carrier and on the probability of carrier collision with atoms, new carriers are created in one or another amount to increase (multiply) the initial photocurrent. In this particular case, the initial photocurrent contains electronic and hole components created in the SCR and the diffusional hole component from the $n^-$ layer. In the second case, electrons created in the $p^+$ layer and diffusionally transported to the SCR prevail. Our estimates give $I_n/I_h \geq 10^2$.

In Fig. 4, the photocurrent (PC) is shown on the semilogarithmic scale as a function of the square root of the external voltage applied to the $p^+–n^-–n^+$ structure, i.e., in fact, to the SCR. Curve *1* corresponds to the above-mentioned case (i) and curve *2* corresponds to (ii). In the first case, the PC is intensely multiplied, starting with certain voltages, to a very high level to demonstrate the onset of avalanche electric breakdown at $V_{br} = 610$ V. But, since the initial PC consisted of the electronic and hole components, one cannot separate these contributions in this curve. However, the situation is unambiguous for curve *2*, because it corresponds almost fully to the electronic PC. Electronic PC displays no evidence of multiplication up to voltages close to their breakdown values and, hence, curve *1* reflects only the hole multiplication. So, the electron system shows no evidence of hole near-critical events. Unfortunately, it is difficult to exactly determine from these data the voltage corresponding to the onset of electron multiplication, because the hole multiplication

achieves by this time more than two orders of magnitude (curve *1*), so that its presence in curve *2* cannot be excluded even at a ratio of one hole per hundred electrons in the initial PC. Since, by this time, the electric field far exceeds the value necessary for the onset of multiplication, it is quite possible that the electron multiplication arises explosively at the instant of avalanche electric breakdown, which occurs only in the presence of both multiplication components. Nevertheless, one can confidently assert that the electron heating is suppressed up to very high fields because of the WSL, which arises and continues unresponsive to the band mixing, i.e., to the fundamental WSL destroyer [11–13]. Thus, the electronic miniband spectrum in 6H–SiC provides conditions for WSL life up to very high fields. Electron tunneling to the upper miniband, which was observed in [20] at a certain field, does not result in full electron delocalization, because, as was shown above, the WSL process is observed at high fields as well. Moreover, it is precisely the WSL that suppresses electron heating and, thus, provides anomalously high (from two to three times higher than the estimates taking into account only the band gap) breakdown fields in 6H–SiC. Intriguing effects can be obtained in a comparative study of the WSL in various SiC polytypic objects with different electronic miniband spectra.

It is also worthy of note that the presence of only one multiplying carrier provides unique conditions for the implementation of high-efficiency photodetectors or solid-state photomultipliers in the UV region.

## REFERENCES

1. F. Bloch, Z. Phys. **52**, 555 (1928); C. Zener, Proc. R. Soc. London, Ser. A **145**, 523 (1934).
2. G. N. Wannier, Phys. Rev. **11**, 432 (1960).
3. L. Esaky and R. Tsu, IBM J. Res. Dev. **14**, 61 (1970).
4. E. E. Mendez, F. Agullo-Rueda, and J. M. Hong, Phys. Rev. Lett. **60**, 2426 (1988).
5. P. Voisin, J. Bleuse, C. Bouche, *et al.*, Phys. Rev. Lett. **61**, 1639 (1988).
6. J. Feldman, K. Leo, D. A. B. Miller, *et al.*, Phys. Rev. B **46**, 7252 (1992).
7. K. Leo, P. Haring Bolivar, F. Bruggeman, *et al.*, Solid State Commun. **84**, 943 (1992).
8. A. Sibille, J. F. Palmier, H. Wang, and F. Mollot, Phys. Rev. Lett. **64**, 52 (1990).
9. F. Bettram, F. Capasso, D. L. Sivco, *et al.*, Phys. Rev. Lett. **64**, 3167 (1990).
10. J. Grenzer, A. A. Ignatov, E. Schomburg, *et al.*, Ann. Phys. (Leipzig) **4**, 1 (1995).
11. A. Rabinovitch and J. Zak, Phys. Rev. B **4**, 2358 (1971).
12. L. Kleinman, Phys. Rev. B **41**, 3857 (1990).
13. N. L. Chupricov, J. Phys.: Condens. Matter **11**, 1069 (1999).

14. Yu. A. Vodakov, A. O. Konstantinov, D. P. Litvin, and V. I. Sankin, Pis'ma Zh. Tekh. Fiz. **7**, 705 (1981) [Sov. Tech. Phys. Lett. **7**, 301 (1981)].

15. A. P. Dmitriev, A. O. Konstantinov, D. P. Litvin, and V. I. Sankin, Fiz. Tekh. Poluprovodn. (Leningrad) **17**, 1093 (1983) [Sov. Phys. Semicond. **17**, 686 (1983)].

16. V. I. Sankin, Yu. A. Vodakov, and D. P. Litvin, Fiz. Tekh. Poluprovodn. (Leningrad) **18**, 2146 (1984) [Sov. Phys. Semicond. **18**, 1339 (1984)].

17. Yu. A. Vodakov, D. P. Litvin, V. I. Sankin, *et al.*, Fiz. Tekh. Poluprovodn. (Leningrad) **19**, 814 (1985) [Sov. Phys. Semicond. **19**, 502 (1985)].

18. V. I. Sankin and A. V. Naumov, Superlattices Microstruct. **10**, 353 (1991).

19. V. I. Sankin and I. A. Stolichnov, Pis'ma Zh. Éksp. Teor. Fiz. **59**, 703 (1994) [JETP Lett. **59**, 744 (1994)].

20. V. I. Sankin and I. A. Stolichnov, Pis'ma Zh. Éksp. Teor. Fiz. **64**, 105 (1996) [JETP Lett. **64**, 114 (1996)].

21. V. I. Sankin and I. A. Stolichnov, Superlattices Microstruct. **23**, 999 (1998).

22. A. F. Volkov and Sh. M. Kogan, Usp. Fiz. Nauk **96**, 633 (1968) [Sov. Phys. Usp. **11**, 881 (1970)].

23. B. L. Gel'mont and M. S. Shur, Fiz. Tekh. Poluprovodn. (Leningrad) **7**, 453 (1973) [Sov. Phys. Semicond. **7**, 326 (1973)].

*Translated by V. Sakun*

# Proximity Effect and Spontaneous Vortex Phase in Planar SF Structures

## V. V. Ryazanov[1, *], V. A. Oboznov[1], A. S. Prokof'ev[1], and S. V. Dubonos[2]

[1]*Institute of Solid-State Physics, Russian Academy of Sciences, Chernogolovka, Moscow region, 142432 Russia*
*\* e-mail: ryazanov@issp.ac.ru*

[2]*Institute of Microelectronic Technology and Ultra-High-Purity Materials, Russian Academy of Sciences, Chernogolovka, Moscow region, 142432 Russia*

The proximity effect in SF structures is examined. It is shown that, due to the oscillations of the induced superconducting order parameter in a ferromagnet, the critical temperature of an SF bilayer becomes minimal when the thickness of the ferromagnetic layer is close to a quarter of the period of spatial oscillations. It is found that the spontaneous vortex state arising in the superconductor due to the proximity of the magnetic domain structure of a ferromagnet brings about noticeable magnetoresistive effects. © 2003 MAIK "Nauka/Interperiodica".
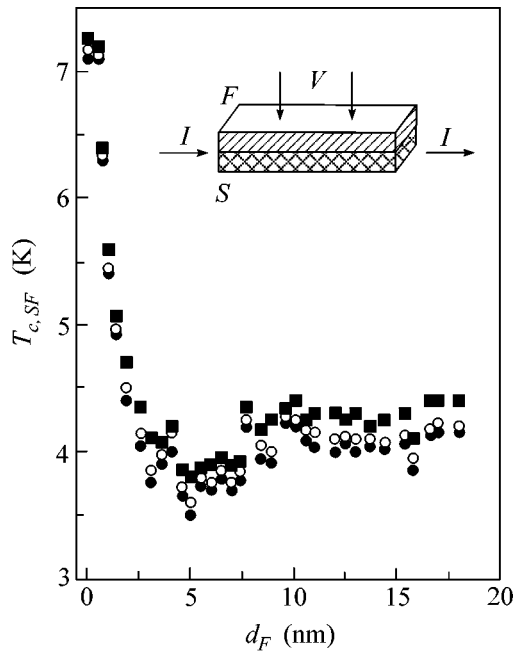
PACS numbers: 74.50.+r; 75.70.Cn; 74.80.Dm

In recent years, considerable interest has been shown in metallic multilayer systems with alternating magnetic and nonmagnetic layers. The normal metal–ferromagnet structures (NF systems) exhibiting giant magnetoresistance have already found practical use in computer technology [1]. Promising elements based on the multilayer superconductor–ferromagnet structures (SF systems), such as the FSF spin gate [2], Josephson SFS $\pi$ junction [3], and others, have also been suggested and studied. The coexistence of superconductivity and ferromagnetism is a problem of long-standing interest. The antagonism of these two phenomena differing in spin ordering is a cause for the strong suppression of superconductivity in the contact area of the S and F materials [4]. The appearance of oscillating sign-variable order parameter in the F layer near the SF interface [3, 5–7] is another fundamental consequence of the proximity of a ferromagnet and a superconductor. In spite of numerous theoretical works, experimental studies of the SF structures are in their infancy. In particular, the influence of a real domain structure on the indicated and other phenomena in the SF systems still remains to be studied. In this work, three different types of SF structures differing in size and geometry were prepared and studied: a continuous thin-film strip of SF bilayer, a macroscopic superconducting S–SF–S bridge (Notarys–Mercereau bridge [8]), and a one-dimensional chain of submicron (mesoscopic) S–SF–S bridges. The goal of this work was to observe the following effects: (i) the influence of the F-layer thickness and the sign-variable order parameter on the critical temperature $T_{c, SF}$ of the SF bilayer; (ii) the appearance of a spontaneous vortex state due to the proximity of the magnetic domain structure of a ferromagnet; and
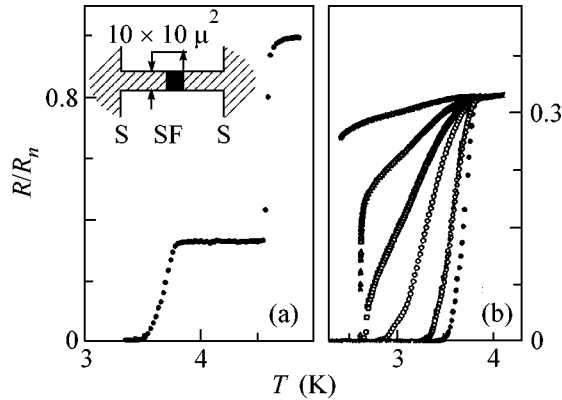
(iii) the appearance of additional resistive contributions in the S–SF–S-bridge chains caused by the injection of nonequilibrium quasiparticles from the SF regions into a superconductor.

Experimental studies were carried out on two-layer Nb–Cu/Ni SF structures, in which the $Cu_{0.43}Ni_{0.57}$ alloy films with the Curie temperature $T_C \sim 150$ K were used as a ferromagnetic layer [9]. The bottom superconducting Nb layer, with a thickness of 9–11 nm (close to the coherence length), was sputtered by dc magnetron. A top copper–nickel alloy film was deposited in a single vacuum cycle by rf diode sputtering. Weak ferromagnetism of the Cu/Ni alloy allowed us to retain the superconductivity of the SF bilayer with $T_{c, SF}$ close to the standard helium temperatures of 2–4 K and compare the obtained results with the results of Josephson experiments [3] on the Nb–$Cu_{0.43}Ni_{0.57}$–Nb sandwiches, in which a weak ferromagnetism was necessary for the fabrication of continuous homogeneous F layers whose thickness would be comparable with the pair-decay length $\xi_F$. Inasmuch as the pair-decay length in the layers of classical ferromagnetic materials (Co, Fe, Ni) is close to 1 nm, the fabrication of thin-film Josephson SFS junctions using these metals is a challenge. The use of ferromagnetic alloys with low Curie temperatures allowed us to increase the pair-decay length by several orders of magnitude and observe the transition of a Josephson SFS junction to the $\pi$ state upon a decrease in temperature [3].

Figure 1 shows the experimental geometry and the measured critical temperature $T_{c, SF}$ of the belayer SF structures with a superconducting niobium layer of thickness 11 nm, close to the coherence length in the thin-film niobium (7–8 nm), and different thicknesses

**Fig. 1.** Critical temperature of a belayer Nb–$Cu_{0.43}Ni_{0.57}$ structure vs. the thickness of ferromagnetic layer.



**Fig. 2.** Resistive transition of the S–SF–S bridge: (a) full curve for a current of 0.5 μA and (b) a part of the transition corresponding to the SF bilayer for currents 0.5, 1, 10, 30, 80, and 110 μA.

inhomogeneous sign-variable order parameter, as was predicted in 1964 by Larkin and Ovchinnikov [11] and Fulde and Ferrel [12]. The induced superconductivity in a ferromagnet near the SF interface proved to be a quite realizable LOFF modification [5, 6, 13]. It was shown in [14, 15] that the spatial oscillations of the order parameter in an SF bilayer with the thickness $d_F$ on the order of coherence length $\xi_F$ in the ferromagnet give rise to oscillations of the SF interface transparency, providing the simplest explanation for the nonmonotonic dependence of $T_{c,\,SF}$ on $d_F$. Simple considerations suggest that the lowest barrier at the SF interface (lowest $T_{c,\,SF}$) corresponds to the thickness $d_F$ close to 1/4 of the period $\lambda_{LOFF}$ of spatial oscillations of the induced superconducting order parameter in the F layer [16]. A comparison of the curve in Fig. 1 with the results of a detailed theoretical analysis was carried out in [16, 17]. We also had a chance to compare the period of spatial oscillations with the results obtained in the experiments with the Josephson SFS sandwiches, in which the same composition of Cu/Ni alloy was used as a Josephson interlayer and the same sputtering technique was applied (for the details of preparation and study of the Josephson SFS junctions, see [3]). The transition to the π state [3, 5, 13, 18], in which the order parameter has different signs on different banks of the SFS sandwich, occurs for ferromagnetic interlayer thicknesses close to a half-period of spatial oscillations of the order parameter. In the Nb–$Cu_{0.43}Ni_{0.57}$–Nb sandwiches, we observed this transition [19] for the F layers with a thickness of 15 nm, i.e., twice the thickness corresponding to the minimal $T_{c,\,SF}$ of an SF bilayer, in agreement with the theoretical estimates [3, 16].

To study the resistive processes in the current flow across the SF bilayer in more detail, planar S–SF–S structures were prepared (their different projections are shown in the insets in Figs. 2, 3). The SF bilayer was situated only in the central section of superconducting bridge and formed from a ferromagnetic strip, which completely spanned the superconducting bridge and suppressed superconductivity in a square area of 10 × 10 μm. To avoid the effects discussed in the preceding paragraph, the *F*-layer thickness was taken to be large enough (18 nm) to appreciably suppress the S layer and exclude the formation of a barrier associated with the oscillations of superconducting order parameter in the ferromagnet. The bridges with the above-mentioned sizes and the superconducting bridges with F islands of submicron size described in the last section of this article were formed using electron-beam lithography. A two-step resistive junction obtained with a minimal transport current of 0.5 μA is shown in Fig. 2a. The higher temperature step with normal resistance $R_n$ of the structure corresponds to the superconducting transition in the ferromagnet-free thin niobium film. The transition at $T_{c,\,SF}$ = 3.6–3.8 K corresponds to the resistive transition in the SF bilayer with thicknesses $d_S$ = 9 nm and $d_F$ = 18 nm. As is seen in Fig. 2b, the lower

$d_F$ of a ferromagnetic layer. The superconducting transition width was ~0.3 K. The curve shows the $T_{c,\,SF}$ values corresponding to the onset of transition, its middle part, and completion. It is seen that the dependence of $T_{c,\,SF}$ on $d_F$ is nonmonotonic and has a minimum at a ferromagnet thickness of 5–8 nm. Such a dependence was predicted in [6] and first observed for a belayer Nb/Gd structure in [10]. This phenomenon is caused by the appearance of superconducting electron pairs with nonzero net momentum in the presence of an exchange field that gives rise to the specific LOFF state with the

temperature transition broadens sizably with an increase in transport current. However, at the temperature $T^* = 2.6$–$2.65$ K a new sharp step arises, evidencing the abrupt dramatic increase in the critical current of the S–SF–S bridge below this temperature. The bridge current–voltage characteristics (CVCs) for different temperatures (in the absence of applied magnetic field) are shown in Fig. 3. One can clearly see that the jumplike increase in the critical current below $T^*$ is associated with a cardinal change of the resistance mechanism in the bridge. In the temperature range $T^* < T < T_{c,\,SF}$, the characteristics exhibit constant differential resistance corresponding to the magnetic-flux flow regime. The behavior below $T^*$ is typical of long superconducting bridges, in which the dissipation is caused by the sequential appearance of vortex slip lines at the bridge edges. The appearance of each line is displayed on the CVC as a new slanted step, which was experimentally recorded using a repeated current scan in the corresponding area. The unexpected, at first glance, zero-field flux-flow regime at high temperatures can easily be explained by the presence, in the superconductor, of a spontaneous vortex phase associated with the stray magnetic field in the domain walls of the ferromagnetic film. The appearance of the spontaneous vortex phase was theoretically discussed for "superconducting ferromagnets" and multilayer SF structures in [20, 21].

The appearance of the vortex phase lines in the superconducting layer near the domain walls of the ferromagnetic layer with in-plane magnetic anisotropy is shown in the inset in Fig. 4. The correlation between the flux-flow resistance and the number of domains (domain walls) is confirmed by the magnetic field measurements (Fig. 4). Magnetic field was applied parallel to the bilayer plane. The observed symmetric (i.e., even with respect to the field sign) behavior of $R(H)$ is caused by the direct action of the field on the superconducting film. The curves also show positive magnetoresistance peaks at the "magnetization reversal" fields corresponding to the sample coercive field (the hysteresis loop $M(H)$ is schematically drawn above the $R(H)$ curve; coercive fields were measured in the magnetic and Hall experiments). In the step region on the $R(T)$ curve (Fig. 2b), i.e., at temperatures $T$ slightly above $T^*$ and currents $I \geq I_c$, the magnetoresistance coefficient can be rather large and exceed 100%.

We now discuss the conditions for the appearance of spontaneous vortex phase in the SF bilayer and the value of critical temperature $T^*$ for the transition to the "Meissner" phase. The lower critical field for the penetration of a perpendicular magnetic field into the film is determined by the effective penetration depth $\lambda_\perp = \lambda^2/d_s$ and its temperature dependence ($\lambda$ is the field penetration depth into a thick film). Using the parameters of our film, one can estimate $H_{c1}(0) \sim 10$–$20$ G. This is comparable with the estimates of stray fields in the domain structure of our weak ferromagnet, if one
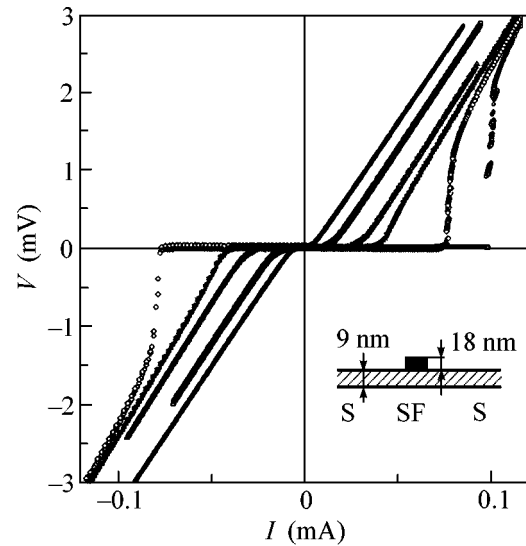


**Fig. 3.** Current–voltage characteristics of the S–SF–S bridge at temperatures 3.47, 3.2, 2.89, 2.66, 2.6, and 2.49 K.
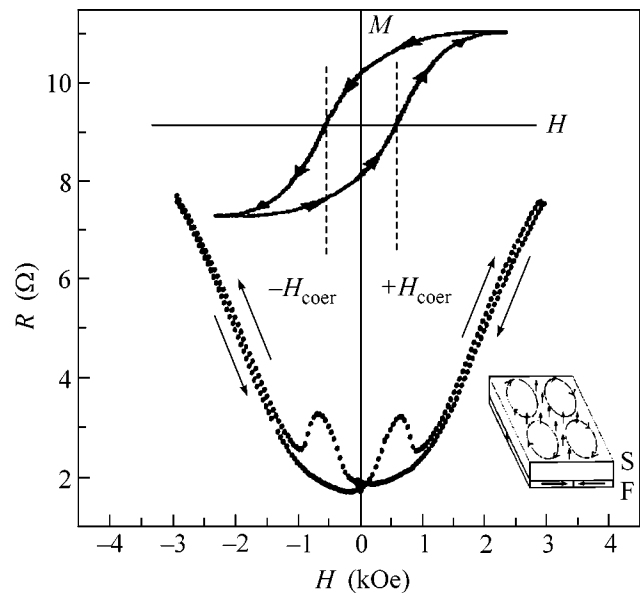


**Fig. 4.** Resistance of the S–SF–S bridge vs. longitudinal magnetic field at $T = 2.66$ K and a current of 50 µA. Arrows indicate the field-scan direction. The magnetization curve for a Cu/Ni layer is schematically shown at the top.

assumes that the domain wall width is on the order of the domain size ($\sim 0.2$–$0.5$ µm). Therefore, $T^*$ is the temperature for which the stray field becomes comparable with $H_{c1}(T)$. Below this temperature, the field of ferromagnetic film does not pierce the superconducting film through, and the flux-flow regime ceases. This model is additionally confirmed by the fact that the constant differential resistance disappears from the CVCs
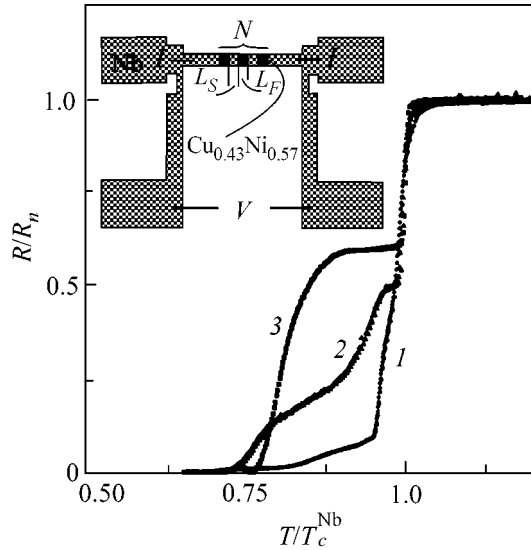
**Fig. 5.** Resistive transitions of a one-dimensional chain of S–SF–S bridges: $N = $ (*1*) 30, (*2*) 70, and (*3*) 100.

of S–SF–S bridges with the F-island sizes on the order of $0.2 \times 0.5$ μm. The ferromagnetic islands with this area are, in fact, single-domain, so that the stray field in the region of such a domain is appreciably weaker than the field produced by the domain wall.

We undertook an attempt at connecting the neighboring SF regions together in a one-dimensional chain of S–SF–S bridges using spin-polarized quasiparticles injected into the ferromagnet-free sections of the superconducting film. As is illustrated in the inset in Fig. 5, a section of the initial SF bilayer was "cut" at a length of 50 μm so as to form SF bridges separated by the sections of the Nb film. Since the length $L_F = 0.2$ μm of the ferromagnetic island remained constant, the spacing between the islands was varied by changing their number $N$ in the structure. The results obtained for three structures with the superconducting sections $L_S = 1$, 0.5, and 0.2 μm and, correspondingly, the number of SF islands $N = 30$, 70, and 100 are presented in Fig. 5. In all cases, the bridge width was equal to 0.5 μm. The resistive transition curves are given in the $T/T_c^{\mathrm{Nb}}$ coordinates, because the critical temperatures of the free Nb sections were slightly different due to the fact that the instant of time the Cu/Ni layer etching was completed could not be controlled accurately, so that the niobium layers were slightly different in thickness. In addition to this transition and a rather smeared resistive transition in the SF islands, a new step, associated with the resistance caused by the nonequilibrium quasiparticle injection into the superconducting sections, evolves in the mid-transition region starting at $L_S = 1$ μm. At $L_S = 0.2$ μm ($N = 100$), this contribution becomes dominant. The estimate of the penetration depth of nonequilibrium quasiparticles (charge-disbalance relaxation length $\lambda_Q$) into superconducting Nb at temperatures

close to $T_c^{\mathrm{Nb}}$ gives a value comparable to 0.2 μm. For the case of spontaneous antiparallel alignment of the magnetizations in the neighboring F islands, one could expect noticeable magnetoresistive effects in a magnetic field applied in the layer planes perpendicular to the bridge chain. Nevertheless, no appreciable effects were observed, most probably because of the absence of antiferromagnetic alignment and the weak spin polarization of quasiparticles in our system.

In summary, proximity effect in the SF system have been studied in this work; it is shown that, due to the spatial oscillations of the induced superconducting order parameter in a ferromagnet, the critical temperature $T_{c, SF}$ of a bilayer has a minimum when the thickness of the ferromagnetic layer is close to a quarter of the period of spatial oscillations. The occurrence of a spontaneous vortex state caused by the proximity of the domain magnetic structure of a ferromagnet has been observed in a superconductor. In this state, the magnetoresistive effects are quite appreciable.

REFERENCES

1. S. S. P. Parkin, K. P. Roche, M. G. Samant, *et al.*, J. Appl. Phys. **85**, 5828 (1999); B. N. Engel, in *Abstracts of International Symposium on Metallic Multilayers* (Aachen, Germany, 2001), p. 26.

2. L. R. Tagirov, Phys. Rev. Lett. **83**, 2058 (1999).

3. V. V. Ryazanov, V. A. Oboznov, A. Yu. Rusanov, *et al.*, Phys. Rev. Lett. **86**, 2427 (2001).

4. P. G. de Gennes and G. Sarma, J. Appl. Phys. **34**, 1380 (1963); J. J. Hauser, H. C. Theuerer, and N. R. Werthamer, Phys. Rev. **142**, 118 (1966); N. V. Zavaritskiĭ and V. N. Grigor'ev, Pis'ma Zh. Éksp. Teor. Fiz. **14**, 112 (1971) [JETP Lett. **14**, 73 (1971)].

5. A. I. Buzdin, L. N. Bulaevskiĭ, and S. V. Panyukov, Pis'ma Zh. Éksp. Teor. Fiz. **35**, 147 (1982) [JETP Lett. **35**, 178 (1982)].

6. Z. Radovic, L. Ledvij, L. Dobrosavljevic-Grujic, *et al.*, Phys. Rev. B **44**, 759 (1991).

7. T. Kontos, M. Aprili, J. Lesueur, and X. Grison, Phys. Rev. Lett. **86**, 304 (2001).

8. H. A. Notarys and J. E. Mercereau, Physica (Utrecht) **55**, 424 (1971).

9. A. Rusanov, R. Boogaard, M. Hesselberth, *et al.*, Physica C (Amsterdam) **369**, 300 (2002).

10. J. S. Jiang, D. Davidovic, D. H. Reich, and C. L. Chien, Phys. Rev. Lett. **74**, 314 (1995).

11. A. I. Larkin and Yu. N. Ovchinnikov, Zh. Éksp. Teor. Fiz. **47**, 1136 (1964) [Sov. Phys. JETP **20**, 762 (1965)].

12. P. Fulde and R. A. Ferrel, Phys. Rev. A **135**, 550 (1964).

13. A. I. Buzdin, B. Vuĭchich, and M. Yu. Kupriyanov, Zh. Éksp. Teor. Fiz. **101**, 231 (1992) [Sov. Phys. JETP **74**, 124 (1992)].

14. J. Aarts, J. M. E. Geers, E. Bruck, *et al.*, Phys. Rev. B **56**, 2779 (1997).

15. L. Lazar, K. Westerholt, H. Zabel, *et al.*, Phys. Rev. B **61**, 3711 (2000).

16. Ya. V. Fominov, N. M. Chtchelkatchev, and A. A. Golubov, Phys. Rev. B **66**, 014507 (2002).

17. Ya. V. Fominov, N. M. Chtchelkatchev, and A. A. Golubov, Pis'ma Zh. Éksp. Teor. Fiz. **74**, 101 (2001) [JETP Lett. **74**, 96 (2001)].

18. V. V. Ryazanov, V. A. Oboznov, A. V. Veretennikov, and A. Yu. Rusanov, Phys. Rev. B **65**, 020501(R) (2002).

19. V. V. Ryazanov *et al.* (in press).

20. E. B. Sonin, Phys. Rev. B **66**, 100504(R) (2002); cond-mat/0102102; cond-mat/0202193.

21. S. Erdin, A. F. Kayali, I. F. Lyuksyutov, and V. L. Pokrovsky, Phys. Rev. B **66**, 014414 (2002); I. F. Lyuksyutov and V. L. Pokrovsky, cond-mat/9903312.

*Translated by V. Sakun*

# Electron-Level Dynamics in the Presence of Impurities and the Ruijsenaars–Schneider Model

## V. G. Marikhin

*Landau Institute for Theoretical Physics, Russian Academy of Sciences, ul. Kosygina 2, Moscow, 117940 Russia*
*e-mail: mvg@itp.ac.ru*
Received November 12, 2002; in final form, December 3, 2002

The dynamic equations for the energy level of a finite system with impurities are shown to be equivalent to the rational Ruijsenaars–Schneider system. The action, which is simultaneously the generating function of the Bäcklund canonical transformation for this system, is calculated. Various variants of statistical averaging of the energy-level distribution are discussed. © 2003 MAIK "Nauka/Interperiodica".

PACS numbers: 71.55.-i

Much work has been devoted to the problem of electron-level dynamics under the action of an additional perturbation (see, e.g., [1, 2]). The role of time in these dynamics is played by the perturbation amplitude. In the cited works, the statistical properties of the spectra are mainly considered; i.e., the response of a system to the additional perturbation is calculated by averaging, e.g., over an ensemble of random matrices. Of interest is also the problem of deriving the dynamic equations for the energy levels of a system with an arbitrary initial spectrum and subsequent averaging. In this case, the averaging procedure may be different, e.g., from the procedure used in the theory of random matrices. The problem of spectrum dynamics of a system for an arbitrary form of perturbation was solved in [3]. The system of equations derived in [3] involves both the eigenvalues and the matrix elements of perturbation as unknown functions, for which reason it is too complicated for analysis. From the physical point of view, one can consider the impurity potential as a perturbation. This highly simplifies the problem; moreover, the many-impurity problem can be reduced to a single-impurity problem (see below).

Let us consider a finite quantum system with $N$ eigenstates and the Hamiltonian $\hat{H}_0$ ($N \times N$ matrix). In the presence of an impurity in the system, the energy levels undergo shifts (in this way, the problem was considered, e.g., in [4] and [5]); the problem is to derive dynamic equations for the energy levels, with the impurity potential playing the role of time.

The Hamiltonian of a system with impurity has the form

$$\hat{H} = \hat{H}_0 + t|0\rangle\langle 0|, \tag{1}$$

where $|0\rangle$ is the quantum state localized on the impurity.

For simplicity, we denote by $x$ and $y$ the eigenstates and by $|x\rangle$ and $|y\rangle$ the eigenfunctions of the unperturbed and perturbed systems, respectively; i.e.,

$$\hat{H}_0|x\rangle = x|x\rangle, \quad \hat{H}|y\rangle = y|y\rangle; \tag{2}$$

then, calculating the matrix element $\langle x|\hat{H}|y\rangle = \langle x|\hat{H}_0 + \hat{V}|y\rangle$, one obtains the condition

$$y\langle x|y\rangle = x\langle x|y\rangle + t\langle x|0\rangle\langle 0|y\rangle,$$

from which it follows that the equations for the eigenvalues of the perturbed system is

$$t\sum_x \frac{|\langle x|0\rangle|^2}{y - x} = 1,$$

or, in the explicit form,

$$t\sum_j^N \frac{|\langle x_j|0\rangle|^2}{y_i - x_j} = 1, \quad i = 1, 2, \dots, N. \tag{3}$$

Denoting $y_i = x_i(t)$ and $x_i = x_i(0)$, one can rewrite Eq. (3) in the polynomial form

$$R(x_j(t), t) = 0,$$

$$P(\xi, t) = \prod_j (\xi - x_j(t)) = P(\xi) - tQ(\xi), \tag{4}$$

where

$$P(\xi) = P(\xi, 0) = \prod_i (\xi - x_i(0)),$$

$$Q(\xi) = P(\xi) \sum_i \frac{\dot{x}_i(0)}{\xi - x_i(0)}, \tag{5}$$

with $\dot{x}_i(0) = |\langle x|0\rangle|^2$.

Note that the case $Q(\xi) = (1/N)P'(\xi) \longleftrightarrow \dot{x}_i(0) = 1/N$ corresponds to the unperturbed Hamiltonian $\hat{H}_0$ (2) whose eigenfunctions are plane waves with the matrix elements equal in magnitude and $\sum_x |\langle x|0\rangle|^2 = 1$.

From condition (4), it follows that $(\partial^2/\partial t^2)P(\xi, t) = 0$. Substituting the expression for $P(\xi, t)$, one obtains the desired equation of level dynamics:

$$\ddot{x}_i = 2\dot{x}_i \sum_{j \neq i} \frac{\dot{x}_j}{x_i - x_j}. \qquad (6)$$

This is the well-known rational Ruijsenaars–Schneider (RS) system of equations describing the dynamics of a many-body system [6, 7].

One can readily see that Eqs. (4) and (5) give the exact solution of the Cauchy problem for RS system (6). Indeed, evaluating polynomials $P(\xi)$ and $Q(\xi)$ by Eqs. (5), one can determine the $P(\xi, t)$ polynomial (4) whose roots are equal to the particle positions $x_i(t)$. In the impurity problem (3), all velocities $\dot{x}_i$ are positive.

The fact that the rational RS system describes the level dynamics of a finite system with impurity is likely to be a new fact. In [3], the equation of electron-level dynamics was derived for an arbitrary perturbation $V$, but Eq. (6) was not obtained.

Note that any impurity potential in a finite system has the form

$$V = \sum_{j}^{N} t_j |j\rangle\langle j|,$$

where $|j\rangle$ is the state localized in the coordinate space on the site with number $j$. In this case, the eigenvalue equation for the unperturbed system has the form (cf. Eq. (3))

$$\det(\delta_{ij} - G_{ij}t_j) = 0, \quad G_{ij} = \sum_x \frac{\langle i|x\rangle\langle x|j\rangle}{y - x}. \qquad (7)$$

For several impurities, the polynomial $P(\xi, t_1, t_2, \ldots, t_N) = \prod_j (\xi - x_j(t_1, t_2, \ldots, t_N))$ is a linear function of the potential $t_j$ of each impurity. Because of this, the condition $(\partial^2/\partial t_j^2) P(\xi, t_1, t_2, \ldots, t_N) = 0$ is fulfilled for each $j$, and, hence, the dynamics for each "time" $t_j$ obey Eq. (6). Indeed, let us consider the sequence

$$H_0 \longrightarrow H_1 \longrightarrow \ldots \longrightarrow H_{j-1} \longrightarrow H_j \longrightarrow \ldots \longrightarrow H_N,$$

$$H_j = H_{j-1} + t_j |j\rangle\langle j|,$$

with the set of eigenvalues of Hamiltonian $H_j$ being determined from Eq. (3), where $x$ are the eigenvalues of $H_{j-1}$, $y$ are the eigenvalues of $H_j$, and $\langle x|0\rangle$ should be replaced by $\langle x|j\rangle$.

Let $\langle x_k^j|$ be the eigenfunctions of Hamiltonian $H_j$. Introduce the instants of time $T_0 = 0$ and $T_j = T_{j-1} + t_j$ ($j = 1, 2, \ldots, N$). Then the energy-level evolution for several impurities can be described by the RS Eqs. (6) with a single time $t$ on the intervals $t \in (T_0, T_1) \cup (T_1, T_2) \cup (T_2, T_3) \ldots$ and the velocities $\dot{x}$ changing jumpwise at the times $T_1, T_2, T_3 \ldots$ :

$$\dot{x}_k|_{t=T_j-0} = |\langle x_k^j|j-1\rangle|^2, \quad \dot{x}_k|_{t=T_j+0} = |\langle x_k^j|j\rangle|^2. \quad (8)$$

As is known (see, e.g., [8]), the RS system of Eqs. (6) is Lagrangian, and the corresponding Lagrangian has the form

$$L = \sum_i \dot{x}_i \log\left[\dot{x}_i \prod_{j \neq i}(x_i - x_j)\right]. \qquad (9)$$

Interestingly, one can obtain an exact expression for the action on the classical trajectory for the system of Eqs. (6): assume that the particle coordinates are $x_i(0) = x_i$ at time $t = 0$ and $x_i(T) = y_i$ at time $t = T$. Then it follows from Eq. (4) that the polynomial $Q(\xi)$ has the form

$$Q(\xi) = \frac{1}{T}\left(\prod_i(\xi - x_i) - \prod_i(\xi - y_i)\right). \qquad (10)$$

At the same time, differentiating $P(\xi, t)$ with respect to $t$ and substituting $\xi = x_i(t)$, one gets

$$Q(x_i(t)) = \dot{x}_i(t) \prod_{j \neq i}(x_i(t) - x_j(t)). \qquad (11)$$

Substituting Eqs. (10) and (11) into the expression for Lagrangian (9), one can evaluate the action

$$S = \int L dt = \sum_i \int dt \dot{x}_i(t) \log Q(x_i(t))$$

$$= \sum_i \int_{x_i}^{y_i} dx \log\frac{1}{T}\left[\prod_j(x - x_j) - \prod_j(x - y_j)\right], \qquad (12)$$

or

$$S = \Delta\log\frac{\Delta}{T} + \sum_{i,\alpha}[g((y_i - z_\alpha) - g(x_i - z_\alpha))], \qquad (13)$$

$$g(x) = x\log\frac{x}{e}, \quad \Delta = \sum_i(y_i - x_i),$$

where $z_\alpha$ are the roots of polynomial $Q(x)$:

$$z_\alpha: \prod_j(z_\alpha - x_j) = \prod_j(z_\alpha - y_j), \qquad (14)$$

$$\alpha = 1, 2, \ldots, N-1.$$

It is worth noting that the calculated action $S$ is simultaneously the generating function of the canonical Bäcklund transformation, i.e., mapping of a momentum–coordinate pair at time $t = 0$ onto the momentum–coordinate pair at $t = T$: $(\{p_i\}, \{x_i\}) \longrightarrow (\{\hat{p}_i\}, \{y_i\})$ for the system of Eqs. (6),

$$p_i = \frac{\partial S}{\partial x_i}, \quad \hat{p}_i = -\frac{\partial S}{\partial y_i}, \qquad (15)$$

with the canonically conjugate variables for system (6) being determined in the ordinary way:

$$p_i = \frac{\delta L}{\delta \dot{x}_i} = \log(\dot{x}_i) + 1 + \sum_{j \neq i} \log(x_i - x_j),$$

$$H = \sum_i p_i \dot{x}_i - L = \sum_i \dot{x}_i, \qquad (16)$$

with the canonical Poisson bracket

$$\{p_i, x_j\} = \delta_{ij}, \quad \{p_i, p_j\} = 0, \quad \{x_i, x_j\} = 0.$$

Let us calculate the phase-space element in the variables $\{x_i\}$, $\{y_i\}$:

$$\prod_i dx_i dp_i = \prod_i dx_i dy_i J(\{x_i\}, \{y_i\}), \qquad (17)$$

where the Jacobian of transformation is given by the formula

$$J(\{x_i\}, \{y_i\}) = \left| \det\left(\frac{\partial p_i}{\partial y_j}\right) \right|$$

$$= \frac{\prod_{i>j} |x_i - x_j| \prod_{i>j} |y_i - y_j|}{\prod_{i,j} |x_i - y_j|}, \qquad (18)$$

because it follows from Eq. (16) that $\partial p_i / \partial y_j = \partial \log \dot{x}_i / \partial y_j$, while the velocities $\dot{x}_i$ can be found from Eqs. (10) and (11):

$$\dot{x}_i(0) = -\frac{1}{t} \frac{\prod_{i,j}(x_i - y_j)}{\prod_{j \neq i}(x_i - x_j)}.$$

The resulting Jacobian $J(\{x_i\}, \{y_i\})$ can be considered as a probability density of the joint distribution of energy levels $\{x_i\}$ in the unperturbed and $\{y_i\}$ in the perturbed systems. Here, it is assumed that the initial particle distribution in the phase space is uniform, which is quite natural for the Hamiltonian particles. One can also specify the initial positions of particles;

then the statistics will be determined by the momentum distribution. Therefore, it is assumed that the momentum distribution of particles is uniform in the initial state.

The momentum distribution function, naturally, depends on the particular type of system (1). For example, the case where the Hamiltonian $H_0$ is a random matrix belonging to the classical Gaussian ensemble (orthogonal ($\beta = 1$), unitary ($\beta = 2$), or symplectic ($\beta = 4$)) was considered in [4]. Note that distribution function (18) is a formal limit $\beta \longrightarrow 0$ of Eq. (5) in [4] for the distribution function in the case of classical ensembles.

In summary, it has been shown in this work that the energy-level dynamics of a finite quantum-mechanical system with impurity is described by the RS equations. The many-impurity problem can be reduced to a one-dimensional problem; i.e., it also obeys the RS equation, with the velocities undergoing jumps in the course of evolution.

It would be of interest to explicitly describe the transition from the equation of level dynamics (RS equation) to the dynamic equations for the level distribution function; it is shown in [2] that the evolution of the distribution function is described by the Fokker–Planck equation, which reduces in this case to the Colojero–Moser quantum system. It is also known (see, e.g., [8]) that the Colojero–Moser equation is a nonrelativistic limit of the RS equation. The question then arises of the interconnection between the quantum RS model [7] and the statistical properties of electronic spectra.

## REFERENCES

1. B. D. Simons and B. L. Altshuler, Phys. Rev. Lett. **70**, 4122 (1993).
2. O. Narayan and B. S. Shastry, Phys. Rev. Lett. **71**, 2106 (1993).
3. P. Pechukas, Phys. Rev. Lett. **51**, 943 (1983).
4. I. L. Aleiner and K. A. Matveev, Phys. Rev. Lett. **80**, 814 (1998).
5. V. G. Marikhin, Pis'ma Zh. Éksp. Teor. Fiz. **64**, 57 (1996) [JETP Lett. **64**, 62 (1996)].
6. S. N. M. Ruijsenaars and H. Schneider, Ann. Phys. (N.Y.) **170**, 370 (1986).
7. S. N. M. Ruijsenaars, Commun. Math. Phys. **110**, 191 (1987).
8. H. W. Braden and Ryu Sasaki, Prog. Theor. Phys. **97**, 1003 (1997).

*Translated by V. Sakun*

# Real-Time Coding in a Parallel Quantum Communication Channel

## S. N. Molotkov

*Institute of Solid State Physics, Russian Academy of Sciences, Chernogolovka, Moscow region, 142432 Russia\**
*Faculty of Computational Mathematics and Cybernetics, Moscow State University,*
*Vorob'evy gory, Moscow, 119899 Russia*
Received November 12, 2002; in final form, December 3, 2002

Coding theorems formulated as exchange protocols in the space of states of quantum systems do not answer one of the basic questions of real-time information transmission rate. Expressions obtained for the transmission capacity of a binary quantum communication channel describe the real-time information transmission rate. © 2003 MAIK "Nauka/Interperiodica".

PACS numbers: 03.67.Hk; 89.70.+c

Transmission capacity is the basic characteristic that determines the information transmission rate with an arbitrarily low error probability in the asymptotic limit of long sequences [1, 2]. Classical information in quantum communication channels is carried by quantum states and extracted by measurements. A quantum state itself can be transmitted through a communication channel (transmission of quantum information).

A number of profound and remarkable results have been obtained [3–6] for quantum communication channels. These results generalize the Shannon theorems for classical channels. Coding theorems for quantum communication channels were reviewed by Holevo in [3].

When calculating the transmission capacity for quantum channels, coding theorems are usually formulated as protocols, where only the properties of the space of states are used. Any information transmission by both quantum and classical states occurs in space and time. Coding theorems formulated as protocols in the space of states of quantum systems do not answer one of the basic questions of the real-time information transmission rate. In this work, we obtain the explicit expressions for the transmission capacity of a binary quantum communication channel that describe the real-time information transmission rate. Below, the case of independent parallel communication channels with finite observation time is considered. In contrast to a sequential relativistic quantum communication channel, the channel transmission capacity in this case can be obtained in the exact analytic form. Information is carried by single-particle states of a relativistic massless particle (photon). Classical information is coded into polarization states. The presence of many parallel independent channels does not mean that, e.g., many optical fiber lines are required. The set of parallel chan-

nels can be realized on the basis of a single channel with limited frequency band (multimode channel). In this case, each channel corresponds to its individual frequency band.

A quantum channel is specified by mapping (using a superoperator) input density matrices onto output ones. We consider below the ideal communication channel. The nonideality arises due to a limited observation time window at the receiver end. It can be effectively described by a certain superoperator. For a binary quantum channel, one can find the optimal spacetime form (amplitude) of states that ensures the maximum transmission capacity for a given observation time window and channel transmission band. Moreover, the resulting expression for the transmission capacity also retains its functional form in the case where measurements at the receiver are carried out in an inertial reference frame moving relative to the source.

Let the binary alphabet symbols $\{0, 1\}$ taken with probabilities $\{\pi_0, \pi_1\}$ $(\pi_0 + \pi_1 = 1)$ correspond to the single-photon states of the form

$$
\begin{aligned}
|\varphi_\mu\rangle &= \int d\hat{x}\, \varphi(\hat{x}) \varphi_\mu^+(\hat{x})|0\rangle \\
&= \int \frac{dk}{k} \varphi(k, k_0 = |k|) a_\mu^+(\hat{k})|0\rangle, \quad \mu = 0, 1,
\end{aligned}
\tag{1}
$$

where $[a_i^-(\hat{k}), a_i^+(\hat{k}')] = \delta_{i, i'} k_0 \delta(k - k')$, $|k\mu\rangle = a_\mu^+(\hat{k})|0\rangle$, $\langle ki|k'i'\rangle = k_0 \delta_{ii'}\delta(k - k')$, $i, i' = \pm$, polarization index $\mu$ takes the values 0 and 1 (in the general case, states are not orthogonal), $a_\mu^+(\hat{k}) = \alpha_\mu a_0^+(\hat{k}) + \beta_\mu a_1^+(\hat{k})$, $(|\alpha_\mu|^2 + |\beta_\mu|^2 = 1)$, and subscript $i$ corresponds to the orthogonal basis helicity states.

---

\* Basic affiliation.

Below, we consider field states propagating in one direction of the $x$ axis ($k > 0$); these are precisely the states that carry information between remote users:

$$|\varphi_\mu\rangle = \int_0^\infty \frac{dk}{k}\tilde{\varphi}(k,k)|k\mu\rangle$$

$$= \int_0^\infty dk\varphi(k)|k\mu\rangle = \int_{-\infty}^\infty d(x-t)\varphi(x-t)|x-t,\mu\rangle, \quad (2)$$

$$\varphi(k) = \frac{\tilde{\varphi}(k,k)}{\sqrt{k}},$$

where

$$\varphi(x-t) = \int_0^\infty e^{-i(k(x-t))}\varphi(k)dk,$$

$$(3)$$

$$|x-t,\mu\rangle = \int_0^\infty e^{ik(x-t)}|k\mu\rangle, \quad \langle\varphi_\mu|\varphi_\mu\rangle = 1.$$

The physical states in $\mathcal{H}$ are specified by their amplitudes on the mass shell. The amplitude of states propagating in one direction depends only on the difference $\tau = x - t$; i.e., if the measurement outcome occurs at time $t$ in the neighborhood $(x, x+dx)$, the same outcome can be obtained at time $t'$ in the neighborhood $(x', x'-x+t+dx)$. For brevity, we will say below that the amplitude $\varphi(\tau)$ is specified on the light cone branch.

We assume for the moment that the spatial amplitude is the same for different polarization states and that the density matrix for an individual channel is $\rho = \pi_0\rho_0 + \pi_1\rho_1 = \pi_0|\varphi_0\rangle\langle\varphi_0| + \pi_1|\varphi_1\rangle\langle\varphi_1|$. Therefore, the density matrix for the ensemble of messages of length $n$ in $n$ different channels is $\rho^{\otimes n} = \rho \otimes \rho \ldots \rho$. In the quantum case, the coding theorems for a source with messages described by the tensor product of individual bits use, as in the classical case, the concept of typical sequences [1] and random coding. The sequences of $M$ code words of length $n$ are chosen at random according to the distribution $\{\pi_0, \pi_1\} - |\varphi_{\vec{\mu}}^M\rangle = |\varphi_{\mu_1}^M\rangle \otimes |\varphi_{\mu_2}^M\rangle \ldots |\varphi_{\mu_n}^M\rangle$.

Measurements at the receiver reduce to projection onto the code words (for details, see [3–6]). The space of outcomes, where the probability distribution arises upon decoding, is a set of discrete values of index $\mathbf{\mu} = \{\mu_1, \mu_2, \ldots, \mu_n\}$ for a set of $M$ code words of messages of length $n$. The fundamental distinction of the decision rule (unity decomposition) for a limited observation time window $T$ at the receiver is that the space of outcomes is the direct product $\Omega = [(\tau_1 \in T, \mu_1) \cup (\tau_1 \notin T, \mu_1)] \times \ldots \times [(\tau_n \in T, \mu_n) \cup (\tau_n \notin T, \mu_n)]$. When decoding, the measurement outcome in each channel (for each polarization index $\mu_k$, $k = 1, \ldots, n$) can occur either in the time window $\tau_k \in T$ for $|\varphi_{\mu_k}\rangle$ or beyond the obser-

vation time window $\tau_k \notin T$, independently of other channels. For an observer, these outcomes mean that the detector does not trigger in the time window $T$.

Since the information is coded into the polarization states while the spatial degrees of freedom play the auxiliary role of polarization "carrier," any operator measuring the polarization state in a limited time window can be expanded in terms of basis operators

$$X_{ii'} = \int_0^\infty \frac{dk}{k}|ki\rangle\langle ki'| = \mathcal{M}_{ii'}(\tau \in T) + \mathcal{M}_{ii'}(\tau \notin T), \quad (4)$$

where

$$\mathcal{M}_{ii'}(\tau \in T)$$

$$= \int_T \frac{d\tau}{2\pi}\left(\int_0^\infty \frac{dk}{\sqrt{k}}e^{ik\tau}|ki\rangle\right)\left(\int_0^\infty \frac{dk'}{\sqrt{k'}}e^{-ik'\tau}\langle k'i'|\right), \quad (5)$$

and $\mathcal{M}_{ii'}(\tau \notin T)$ has a similar form. Any measurement of polarization states in a limited time window reduces to the following reduced density matrix, which is obtained by taking partial trace over the spacetime variable $\tau$:

$$\rho_{ii'} = \mathrm{Tr}_\tau\{\rho X_{ii'}\}$$

$$= \mathrm{Tr}_\tau\{\rho\mathcal{M}_{ii'}(\tau \in T)\} + \mathrm{Tr}_\tau\{\mathcal{M}_{ii'}(\tau \notin T)\} \quad (6)$$

$$= \rho_{ii'}(\tau \in T) \bigoplus \rho_{ii'}(\tau \notin T).$$

The first and second terms describe the outcomes inside and outside the time window $T$, respectively. For an observer, the latter outcomes mean that the measuring device does not trigger. The sign of the direct product is used to emphasize that the reduced density matrix acts in the orthogonal spaces; i.e., measurements on the extraction of information from the polarization degrees of freedom lead to mutually exclusive outcomes inside and outside the observation time window, independently of the polarization states.

From this point, the problem can be reduced to the calculation of transmission capacity for the communication channel described by the effective superoperator that transforms the total density matrix into the reduced density matrix containing only polarization degrees of freedom. One has

$$\mathcal{T}[\rho] = \rho_{ii'}(\tau \in T) \bigoplus \rho_{ii'}(\tau \notin T). \quad (7)$$

The reduced density matrix for pure states can be represented in the convenient symbolic form

$$\mathcal{T}[\rho_{\mu_l}] = (1-\varepsilon)|\mu_l\rangle\langle\mu_l| + \varepsilon|?\rangle\langle?|, \quad l = 0, 1. \quad (8)$$

$$(1-\varepsilon)|\mu_l\rangle\langle\mu_l|$$

$$= \int_T \frac{d\tau}{2\pi} \left( \int_0^\infty \int_0^\infty \frac{dk\,dk'}{\sqrt{kk'}} \tilde{\varphi}(k) e^{ik'\tau} \sum_{i=0,1} \langle k'i|k\mu_l\rangle \right)$$

$$\times \left( \int_0^\infty \int_0^\infty \frac{dk\,dk'}{\sqrt{kk'}} \tilde{\varphi}^*(k) e^{-ik'\tau} \sum_{i=0,1} \langle k\mu_l|k'i\rangle \right) \tag{9}$$

$$= \int_T \frac{d\tau}{2\pi} |\varphi(\tau)|^2 \left( \sum_{i=0,1} [\delta_{i,0}\alpha_{\mu_l} + \delta_{i,1}\beta_{\mu_l}] \right)$$

$$\times \left( \sum_{i'=0,1} [\delta_{i',0}\alpha_{\mu_l}^* + \delta_{i',1}\beta_{\mu_l}^*] \right),$$

$$\varepsilon|?\rangle\langle?|$$

$$= \int_{\bar{T}} \frac{d\tau}{2\pi} \left( \int_0^\infty \int_0^\infty \frac{dk\,dk'}{\sqrt{kk'}} \tilde{\varphi}(k) e^{ik'\tau} \sum_{i=0,1} \langle k'i|k\mu_l\rangle \right) \tag{10}$$

$$\times \left( \int_0^\infty \int_0^\infty \frac{dk\,dk'}{\sqrt{kk'}} \tilde{\varphi}^*(k) e^{-ik'\tau} \sum_{i=0,1} \langle k\mu_l|k'i\rangle \right).$$

where $|?\rangle$ formally denotes the outcomes beyond the observation time window. This state is orthogonal to any basis state; i.e., $\langle?|i\rangle \equiv 0$. Then,

$$\mathcal{T}[\rho] = \pi_0(1-\varepsilon)|\mu_0\rangle\langle\mu_0|$$

$$+ \pi_1(1-\varepsilon)|\mu_1\rangle\langle\mu_1| + \varepsilon|?\rangle\langle?|, \tag{11}$$

$$\mathcal{T}[\rho_{0,1}] = (1-\varepsilon)|\mu_{0,1}\rangle\langle\mu_{0,1}| + \varepsilon|?\rangle\langle?|,$$

and the Neumann entropy is equal to (transmission capacity reaches maximum at $\pi_0 = \pi_1 = 1/2$[3])

$$H(\mathcal{T}[\rho]) = -(1-\varepsilon)\log(1-\varepsilon) - \varepsilon\log\varepsilon$$

$$- (1-\varepsilon)\left[\left(\frac{1-\xi}{2}\right)\log\left(\frac{1-\xi}{2}\right) + \left(\frac{1+\xi}{2}\right)\log\left(\frac{1+\xi}{2}\right)\right], \tag{12}$$

$$\pi_{0,1} H(\mathcal{T}[\rho_{0,1}])$$

$$= -\pi_{0,1}[(1-\varepsilon)\log(1-\varepsilon) + \varepsilon\log\varepsilon], \tag{13}$$

where $\xi = |\langle\mu_0|\mu_1\rangle|$ [see Eq. (9)]. From this point, the problem can be formally reduced to the calculation of transmission capacity for the communication channel specified by Eqs. (7) and (8). The transmission capacity can be calculated by the Holevo formula [3–6]; taking Eqs. (7)–(13) into account, one obtains

$$C(T) = \max_{\{\pi_0, \pi_1\}} \left\{ H(\mathcal{T}[\rho]) - \sum_{i=0,1} \pi_i H(\mathcal{T}[\rho_i]) \right\}. \tag{14}$$

For pure input states, this formula reduces to the formula

$$C(T) = (1-\varepsilon)C(\xi) = -(1-\varepsilon)$$

$$\times \left[\left(\frac{1-\xi}{2}\right)\log\left(\frac{1-\xi}{2}\right) + \left(\frac{1+\xi}{2}\right)\log\left(\frac{1+\xi}{2}\right)\right]. \tag{15}$$

For the pure orthogonal input states (in this case $\xi = 0$), this result becomes particularly transparent: $C(T) = 1 - \varepsilon$. In this case, Eq. (15) is transformed to the expression for the transmission capacity of a classical binary erasing channel with transition probabilities $p(0|0) = p(1|1) = 1 - \varepsilon$, $p(0|?) = p(1|?) = \varepsilon$, and $p(0|1) = p(1|0) = 0$ ($p_0 = p_1 = 1/2$, $p_? = 0$). For the pure orthogonal input states, the number of typical sequences of length $n$ ($n \longrightarrow \infty$) for a source tends to $2^{nH(\rho)}$.

If measurements at the exit end of the communication channel are carried out in a wide time window (formally, $T \longrightarrow \infty$), the number of correctly decoded sequences is $2^{nH(\rho)}$ because of the certain distinguishability of orthogonal states (the states are entirely accessible in this limit). In this case, collective measurements are not required for the orthogonal states (in the binary channel); instead, it suffices to measure states in each individual bit. If measurements are carried out in a finite time window $T$, there will be outcomes for which the measuring device will not trigger during $T$. The probability of such an event is equal to $\varepsilon$, and, correspondingly, the probability of triggering within the time window is $1 - \varepsilon$. If the triggering occurs during $T$, the states are identified with certainty. In the absence of outcome inside the time window, one can believe that the state is erased (it is formally transformed to a certain new state at the receiver end; one can also formally assume that this state is sent with the probability $p_? = 0$ at the entry). Each typical sequence inflates into the Hamming sphere with radius $H(x|y)$. Here, $H(x|y)$ is the Shannon conditional entropy for the input alphabet ($x = \{0, 1, ?\}$) with probabilities $\{p_0 = 1/2, p_1 = 1/2, p_? = 0\}$ and the output alphabet ($y = \{0, 1, ?\}$), with transition probabilities in the channel $p(0|0) = p(1|1) = 1 - \varepsilon$, $p(0|1) = p(1|0) = 0$, and $p(0|?) = p(1|?) = \varepsilon$. Therefore, the number of correctly decoded sequences for $n \longrightarrow \infty$ is equal to

$$\frac{2^{nH(\rho)}}{2^{nH(x|y)}} = 2^{nI(x:y)}, \quad I(x:y) = 1 - \varepsilon, \tag{16}$$

which coincides with the transmission capacity of the classical binary erasing communication channel [2]. Formula (15) is valid for the nonorthogonal input states.

If the communication channel has a finite transmission bandwidth $\Delta k$ (speed of light $c = 1$), the transmission capacity (for fixed angles $\xi$ of the polarization vectors and a fixed time window $T$) reaches a maximum on those states with spacetime amplitude $\varphi(k)$ which correspond to the maximum of $\varepsilon$ and have carriers inside

the transmission band $\Delta k$. This leads to the variational problem in unconditional extremum (maximum) of the functional

$$\mathscr{F} = \frac{\frac{1}{2\pi}\int\limits_{T}|\varphi(\tau)|^2 d\tau}{\int\limits_{0}^{\infty}|\varphi(k)|^2 dk}. \qquad (17)$$

By varying the functional, one arrives at the integral equation for the amplitude

$$\lambda_n \varphi_n(k) = \frac{1}{\pi}\int\limits_{\Delta k} \frac{\sin(k-k')T}{k-k'}\varphi(k')dk', \qquad (18)$$

$$\mathrm{supp}\varphi(k) \in \Delta k.$$

The maximum of the functional and the optimal form of the state are obtained, respectively, for the maximal eigenvalue and the corresponding eigenfunction. This equation was analyzed previously in [7–9]. Its eigenvalues are positive and form a decreasing sequence $(1 > \lambda_0 > \lambda_1 \ldots > 0, n = 0, 1, \ldots, \infty)$. The eigenvalues are functions of the parameter $\Delta k T$. Several first eigenvalues for different $\Delta k T$ values were numerically calculated in [8] (for large $\Delta k T$ values, they rapidly tend to 1; e.g., $\lambda_0 = 0.99589$ for $\Delta k T = 4$). The asymptotic form as a function of parameter $\Delta k T \gg 1$ at a fixed $n$ is also known [9]:

$$\lambda_n(\zeta) \sim 1 - \frac{4\sqrt{\pi}8^n}{n!}\zeta^{n+1/2}e^{-2\zeta}, \quad \zeta = \Delta k T; \qquad (19)$$

i.e., the eigenvalues are exponentially close to unity. Therefore, the error in distinguishing the orthogonal states is exponentially low for a wide time window $(T \gg 1/\Delta k)$, and the channel transmission capacity is exponentially close to unity. For small $\Delta k T \ll 1$, the eigenvalue $\lambda_0 \sim \Delta k T$ and the transmission capacity is $C \sim (\Delta k T)^2 \ll 1$. Thus, the transmission capacity of a channel with finite-width frequency band and finite time window is given by the formula

$$C_T = \frac{C(\Delta k T)}{\Delta k T} = -\frac{\lambda_0(\Delta k T)}{\Delta k T}$$

$$\times \left[\left(\frac{1-\xi}{2}\right)\log\left(\frac{1-\xi}{2}\right) + \left(\frac{1+\xi}{2}\right)\log\left(\frac{1+\xi}{2}\right)\right], \quad (20)$$

$$\left[\frac{\mathrm{bit}}{\mathrm{frequency\ sec}}\right].$$

It describes the maximum admissible information transmission rate in bits per unit frequency band and unit time.

Thus, it follows from Eq. (20) that, in the case of a binary quantum channel, the transmission capacity $C(T) \equiv C(\Delta k T)$ per message reaches its limiting value for both orthogonal and nonorthogonal input states

only in the asymptotic limit of infinite observation time (more precisely, for $\Delta k T = \infty$).

Since we consider the nonrelativistic case, it is important to realize how the expression for transmission capacity looks in other inertial reference frames. We show now that expression (20) for the transmission capacity retains its functional form if the observer at the receiving end performs measurements in a moving reference frame. The measurements in the observer reference frame are written in the same manner as in Eqs. (4)–(6). In this case, all quantities in Eqs. (7)–(10) should be treated as their values in the observer reference frame. The state produced by the action of the appropriate unitary operator of the Poincaré-group representation should be taken as a quantum state that the observer "sees" in the moving frame of reference. The general coordinate transformation in the Poincaré group is a sum of translations in the Minkowski spacetime and Lorentz rotation $\hat{x}' = \hat{P}(\hat{a})\hat{L}\hat{x} = \hat{L}\hat{x} + \hat{a}$, where $\hat{P}(\hat{a})$ is the operator of translation by vector $\hat{a} = (a, a_0)$ and $\hat{L}$ is the operator of Lorentz rotation describing the transition to the other inertial system. These transformations induce transformations of the operators $\hat{U}(\hat{L}, \hat{a})a_\mu^+(\hat{k})\hat{U}^{-1}(\hat{L}, \hat{a}) = e^{i\hat{L}\hat{k}\hat{a}}a_\mu^+(\hat{L}\hat{k})$, where $\hat{U}(\hat{L}, \hat{a})$ is a unitary operator acting in $\mathscr{H}$. Since the polarization vector in this one-dimensional scheme is perpendicular to the wave vector $k$, it does not transform if the observer goes to the reference frame moving along the propagation direction of the photon field.

The observer effectively sees the transformed state of the form (recall that the spacetime amplitudes are taken to be identical for the different polarization states; this (unimportant) assumption enables one to obtain less cumbersome expressions than in the general case)

$$|\varphi_\mu(\hat{L}, \hat{a})\rangle = \hat{U}(\hat{L}, \hat{a})|\varphi_\mu\rangle$$

$$= \int d\hat{x}\tilde{\varphi}(\hat{x})\hat{U}(\hat{L}, \hat{a})\varphi_\mu^+(\hat{x})\hat{U}(\hat{L}, \hat{a})^{-1}\hat{U}(\hat{L}, \hat{a})|0\rangle$$

$$= \int d\hat{k}\tilde{\varphi}(\hat{k})e^{i\hat{k}\hat{k}\hat{a}}\delta(\hat{k}^2)\theta(k_0)a_\mu^+(\hat{L}\hat{k})|0\rangle \qquad (21)$$

$$= \int d\hat{k}\tilde{\varphi}(\hat{L}^{-1}\hat{k})e^{i\hat{k}\hat{a}}|\hat{k}\mu\rangle$$

$$= \int\limits_{0}^{\infty}\frac{dk}{k}\tilde{\varphi}\left(k\sqrt{\frac{1-\beta}{1+\beta}}, k\sqrt{\frac{1-\beta}{1+\beta}}\right)|\hat{k}\mu\rangle,$$

where $dk/k_0$ is the Lorentz invariant integration volume, and it is taken into account that the vacuum vector is invariant; i.e., $\hat{U}(\hat{L}, \hat{a})|0\rangle = |0\rangle$. Let the time interval measured by the observer's clocks at the receiving end in the moving coordinate system be equal to the time interval measured by his clocks in the rest system; i.e.,

$T_m = T$. In this case, the reduced density matrix has the form

$$\mathcal{T}[\rho^m_{\mu_l}] = (1 - \varepsilon_m)|\mu_l\rangle\langle\mu_l| + \varepsilon_m|?\rangle\langle?|,$$
$$\rho^m_{\mu_l} = |\varphi_{\mu_l}(\hat{L}, \hat{a})\rangle\langle\varphi_{\mu_l}(\hat{L}, \hat{a})|, \tag{22}$$

$$(1 - \varepsilon_m)|\mu_l\rangle\langle\mu_l| = \int\limits_{T_m}\frac{d\tau}{2\pi}$$

$$\times\left(\int\limits_0^\infty\int\limits_0^\infty\frac{dk\,dk'}{\sqrt{kk'}}\tilde{\varphi}\left(k\sqrt{\frac{1-\beta}{1+\beta}}\right)e^{ik\tau}\sum_{i=0,1}\langle k'i|k\mu_l\rangle\right) \tag{23}$$

$$\times\left(\int\limits_0^\infty\int\limits_0^\infty\frac{dk\,dk'}{\sqrt{kk'}}\tilde{\varphi}^*\left(k'\sqrt{\frac{1-\beta}{1+\beta}}\right)e^{-ik\tau}\sum_{i=0,1}\langle k'\mu_l|ki\rangle\right),$$

$$\varepsilon_m|?\rangle\langle?| = \int\limits_{\overline{T_m}}\frac{d\tau}{2\pi}$$

$$\times\left(\int\limits_0^\infty\int\limits_0^\infty\frac{dk\,dk'}{\sqrt{kk'}}\tilde{\varphi}\left(k\sqrt{\frac{1-\beta}{1+\beta}}\right)e^{ik\tau}\sum_{i=0,1}\langle k'i|k\mu_l\rangle\right) \tag{24}$$

$$\times\left(\int\limits_0^\infty\int\limits_0^\infty\frac{dk\,dk'}{\sqrt{kk'}}\tilde{\varphi}^*\left(k'\sqrt{\frac{1-\beta}{1+\beta}}\right)e^{-ik'\tau}\sum_{i=01,1}\langle k'\mu_l|ki\rangle\right).$$

Our further goal is to determine the maximum of $\varepsilon_m$. One has

$$\varepsilon_m = \int\limits_{T_m}\frac{d\tau}{2\pi}\left|\int\limits_{\Delta k_m}\frac{dk}{\sqrt{k}}\tilde{\varphi}(k)e^{ik\tau}\right|^2,$$
$$T_m = T\sqrt{\frac{1+\beta}{1-\beta}}, \quad \Delta k_m = \Delta k\sqrt{\frac{1-\beta}{1+\beta}}. \tag{25}$$

Since the eigenvalues of integral equation (18) and, correspondingly, the optimal form of amplitude depend only on $\Delta kT$, the transmission capacity retains its functional form in the moving reference frame and depends on $\Delta k\sqrt{\frac{1-\beta}{1+\beta}}T_m\sqrt{\frac{1+\beta}{1-\beta}} = \Delta kT$. That is, measurements in the moving reference frame do not change transmission capacity. This result is intuitively understandable, because, due to the Doppler effect, the transition to the moving reference frame results in the effective contraction of the frequency spectrum of the state, $\Delta k \longrightarrow \Delta k\sqrt{\frac{1-\beta}{1+\beta}}$ (if the observer moves in the same direction as the state) and, correspondingly, in the effective spatial extension of the state. As a result, it takes larger time $T \longrightarrow T\sqrt{\frac{1+\beta}{1-\beta}}$ to ensure the same fraction of

state in the time window. However, since the result depends only on the product $\Delta kT$, it does not change and also does not depend on the direction of observer's motion (i.e., sign of $\beta = v/c$). This result can be explained as follows. Since the scalar product $\hat{k}\hat{x}$ is Lorentz-invariant, while the spacetime variables for a photon propagating in one direction $k = k_0$ appear only as the combination $\tau = x - t$, the quantity $k\tau$ determining the result is Lorentz-invariant.

In conclusion, we present the expression for the transmission capacity in the case, where the classical alphabet is assigned to the density matrices of general form. As above, the information is coded into the different polarization states. Let the classical alphabet consist of $N$ symbols assigned to the single-photon density matrices $\rho_l$ taken with the probabilities $\rho_l$ ($l = 1\dots N$). In the basis of generalized eigenvectors $|ki\rangle$ ($i = 0, 1$), the density matrix has the following general form:

$$\hat{\rho}^{(l)} = \begin{pmatrix} \rho^{(l)}_{11}(k, k') & \rho^{(l)}_{12}(k, k') \\ \rho^{(l)}_{21}(k, k') & \rho^{(l)}_{22}(k, k') \end{pmatrix}. \tag{26}$$

Measurements in the finite time window result in the reduced density matrix containing only the polarization degrees of freedom. One has

$$\hat{\rho}^{(l)}_e = \text{Tr}\{\mathcal{M}(\tau \in T)\hat{\rho}^{(l)}\} + \text{Tr}\{\mathcal{M}(\tau \notin T)\hat{\rho}^{(l)}\}$$
$$= \begin{pmatrix} \rho^{(l)}_{11}(T) & \rho^{(l)}_{12}(T) \\ \rho^{(l)}_{21}(T) & \rho^{(l)}_{22}(T) \end{pmatrix} \otimes \begin{pmatrix} \rho^{(l)}_{11}(\bar{T}) & \rho^{(l)}_{12}(\bar{T}) \\ \rho^{(l)}_{21}(\bar{T}) & \rho^{(l)}_{22}(\bar{T}) \end{pmatrix}, \tag{27}$$

$$\rho^{(l)}_{ij}(T) = \int\limits_T\frac{d\tau}{2\pi}\left(\int\limits_0^\infty\int\limits_0^\infty dk\,dk'e^{ik\tau}\rho^{(l)}_{ij}(k, k')e^{-ik'\tau}\right), \tag{28}$$
$$i, j = 1, 2,$$

and similarly for $\rho^{(l)}_{ij}(\bar{T})$. The density-matrix block with $t \notin T$ in Eq. (27) is responsible for the outcomes beyond the observation time window. For this reason, one can again formally introduce the state $|?\rangle$ that is orthogonal to any polarization state and retain only the diagonal elements in matrix (27) in order to hold the general unit trace of the density matrix. In the basis $|e_0\rangle$, $|e_1\rangle$, $|?\rangle$, one has

$$\hat{\rho} = \sum_{l=1}^N p_l\hat{\rho}^{(l)}_e,$$

$$\hat{\rho}^{(l)}_e = \begin{pmatrix} \rho^{(l)}_{11}(T) & \rho^{(l)}_{12}(T) & 0 \\ \rho^{(l)}_{13}(T) & \rho^{(l)}_{22}(T) & 0 \\ 0 & 0 & \rho^{(l)}_{11}(T) + \rho^{(l)}_{22}(T) \end{pmatrix}. \tag{29}$$

The transmission capacity is then calculated using Eq. (14) [3–6].

We note that Eq. (20) describes the maximum (optimal) transmission rate of classical information for given transmission band ($\Delta k$) and time window ($T$). This expression is independent of the initial band splitting into $n$ parallel channels, because band narrowing $\Delta k/n$ in each channel will lead to the increase in the observation time as $nT$; hence, the product for the *optimal* form of the state does not depend on $n$ and depends only on the product of the total transmission band and the observation time (transmission rate) $(\Delta k/n)nT = \Delta kT$.

Thus, the explicit inclusion of spacetime into the problem of coding makes it possible to obtain the real-time transmission capacity of a quantum communication channel and clarifies the meaning of the expression obtained for the transmission capacity as an asymptotic quantity with allowance only for the properties of the space of states.

## REFERENCES

1. C. E. Shannon, Bell Syst. Tech. J. **27**, 397 (1948); Bell Syst. Tech. J. **27**, 623 (1948).
2. R. Gallagher, *Information Theory and Reliable Communication* (Wiley, New York, 1968; Sovetskoe Radio, Moscow, 1974).
3. A. S. Kholevo, Probl. Peredachi Inf. **8**, 63 (1972); Probl. Peredachi Inf. **15**, 3 (1979); Usp. Mat. Nauk **53**, 193 (1998); *Introduction to the Theory of Quantum Information* (MTsNMO, Moscow, 2002).
4. R. Jozsa and B. Schumacher, J. Mod. Opt. **41**, 2343 (1994).
5. P. Hausladen, R. Jozsa, B. Schumacher, *et al.*, Phys. Rev. A **54**, 1869 (1996).
6. B. Schumacher and M. D. Westmoreland, Phys. Rev. A **56**, 131 (1997).
7. N. N. Bogolyubov, A. A. Logunov, and I. T. Todorov, *Introduction to Axiomatic Quantum Field Theory* (Nauka, Moscow, 1969; Benjamin, New York, 1974); N. N. Bogolyubov, A. A. Logunov, A. I. Oksak, and I. T. Todorov, *General Principles of Quantum Field Theory* (Nauka, Moscow, 1987; Kluwer Academic, Dordrecht, 1990).
8. D. Slepian and H. O. Pollak, Bell Syst. Tech. J. **40**, 40 (1961).
9. W. H. Fuchs, J. Math. Anal. Appl. **9**, 317 (1964).

*Translated by R. Tyapaev*

# Doubly Phase-Matched Cascaded Parametric Wave Mixing of Ultrashort Laser Pulses

**D. A. Akimov[1], M. V. Alfimov[2], A. A. Ivanov[2], A. B. Fedotov[1, 3], T. A. Birks[4], W. J. Wadsworth[4], P. St. J. Russell[4], S. O. Konorov[1], O. A. Kolevatova[1], A. A. Podshivalov[3], and A. M. Zheltikov[1, 3], ***

[1] *Faculty of Physics, Moscow State University, Vorob'evy gory, Moscow, 119899 Russia*
**e-mail: zheltikov@top.phys.msu.su*
[2] *Center of Photochemistry, Russian Academy of Sciences, ul. Novatorov 7a, Moscow, 117421 Russia*
[3] *International Laser Center, Moscow State University, Vorob'evy gory, Moscow, 119899 Russia*
[4] *Department of Physics, University of Bath, BA2 7AY Bath, United Kingdom*

Received November 21, 2002

Doubly phase-matched cascaded parametric wave mixing of femtosecond laser pulses in tapered fibers is experimentally demonstrated. Fibers with an appropriately tailored dispersion profile allow simultaneous phase matching for two types of nonlinear-optical processes—third-harmonic generation and parametric four-wave mixing. Doubly phase-matched cascaded parametric interactions of ultrashort light pulses give rise to a manifold of new spectral components, expanding substantially the capabilities of the available laser sources of ultrashort pulses. © 2003 MAIK "Nauka/Interperiodica".

PACS numbers: 42.65.Ky; 42.65.Hw; 42.65.Wi; 42.81.Qb

Phase matching of light fields in nonlinear interactions is one of the key problems in nonlinear optics [1, 2]. Dispersion of nonlinear-optical materials gives rise to a mismatch of phase velocities of electromagnetic waves with different frequencies, thereby lowering the efficiency of nonlinear-optical interactions of light fields. Classical approaches to the solution of the phase-matching problem are based on the use of natural birefringence of nonlinear crystals [1, 2], additions compensating the phase mismatch in nonlinear-optical processes in gas media [3], and periodically poled crystals for quasi-phase matching [4, 5]. New phase-matching solutions employing artificial form birefringence [6, 7] and dispersion of photonic crystals [8, 9] are widely discussed and studied experimentally in the past few years.

Optical fibers substantially increase the length of nonlinear-optical interactions, enhancing the generation of new spectral components as a result of nonlinear-optical processes. Nonlinear-optical processes in optical fibers can be phase-matched by using the dispersion of guided modes [10]. Microstructure and tapered fibers [11–13] offer unique opportunities for phase-matching nonlinear interactions by dispersion tailoring. Such fibers also provide a high degree of light-field confinement in the fiber core, leading to high efficiencies of frequency conversion and spectrum transformation even for nanojoule ultrashort laser pulses [13–15].

In this paper, we will show that tapered fibers with an appropriately tailored dispersion profile allow two types of nonlinear-optical processes—third-harmonic generation (THG) and parametric four-wave mixing—to be simultaneously phase-matched. Such a double phase matching will be employed to enhance cascaded nonlinear-optical processes in a tapered fiber. Doubly phase-matched cascaded parametric wave mixing, as will be shown in this work, leads to the generation of a whole manifold of new spectral components, substantially expanding the capabilities of the available laser sources of ultrashort pulses for basic and applied research, including applications in the spectroscopy of ultrafast processes, optical metrology, absolute-phase measurements, biomedical optics, generation of even shorter light pulses, and control of their parameters.

Tailoring the dispersion of guided modes is the backbone of double phase matching in cascaded parametric wave mixing. The resulting dispersion profile should simultaneously phase-match two different nonlinear-optical processes. In this work, we employ tapered fibers to solve this problem. The taper-waist region of these fibers is characterized by a high refractive index step from the fiber core (which is usually made of fused silica) to the fiber cladding (air), resulting in a high degree of laser-radiation confinement in the fiber core [13, 14]. The wavelength corresponding to zero group-velocity dispersion can be tuned for such fibers by changing the taper-waist diameter (Fig. 1). Recent experimental studies [13, 14] have shown that tapered fibers radically enhance nonlinear-optical interactions, including supercontinuum generation. In contrast to hexagonally periodically poled crystals, permit-
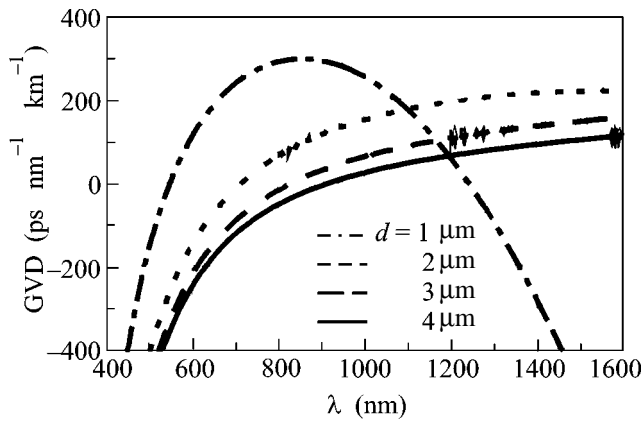
**Fig. 1.** Wavelength dependence of the group-velocity dispersion for fiber taper-waist regions with different taper-waist diameters $d$: (dash–dotted line) $d = 1$ μm, (dotted line) $d = 2$ μm, (dashed line) $d = 3$ μm, and (solid line) $d = 4$ μm.
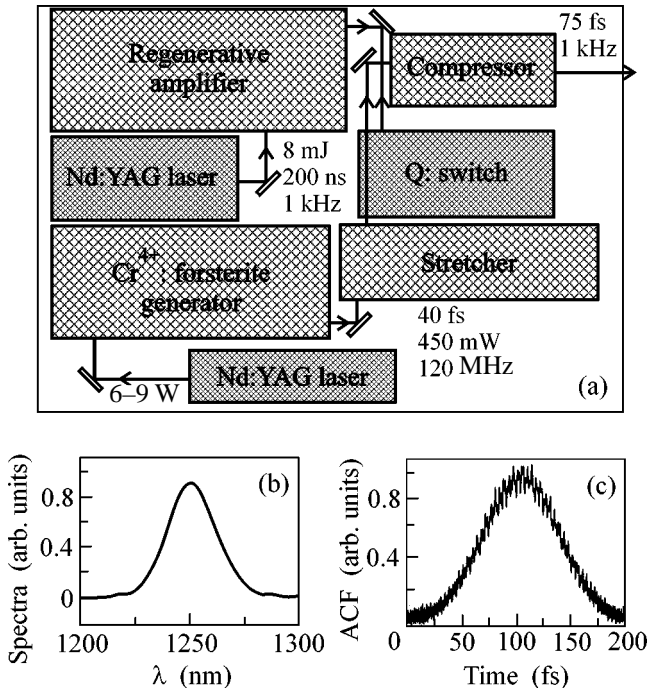


**Fig. 2.** (a) Diagram of the femtosecond Cr:forsterite laser system with a regenerative amplifier. (b) The spectrum and (c) autocorrelation trace of a laser pulse at the output of the master oscillator.

ting quasi-phase matching of noncollinear cascaded wave-mixing processes [16], tapered fibers, as will be shown below, can provide phase matching for several stages of cascaded nonlinear-optical processes in the collinear, waveguiding regime.

Let us illustrate now how phase matching can be simultaneously achieved for two types of nonlinear-

optical processes, namely, third-harmonic generation and parametric four-wave mixing $\omega_2 + \omega_1 = \omega_0 + 3\omega_0$, with $\omega_0$ being the frequency of pump radiation, giving rise to new spectral components with frequencies $\omega_1$ and $\omega_2$. Double phase matching implies that the propagation constants $\beta_0$, $\beta_1$, $\beta_2$, and $\beta_{TH}$ for the guided modes of light fields with frequencies $\omega_0$, $\omega_1$, $\omega_2$, and $3\omega_0$, respectively, should meet the relations $3\beta_0 = \beta_{TH}$ and $\beta_0 + \beta_{TH} = \beta_1 + \beta_2$. These equalities yield the following simple requirement on the propagation constants $\beta_0$, $\beta_1$, and $\beta_2$: $4\beta_0 = \beta_1 + \beta_2$.

The half-sum of the propagation constants of the spectral components with the frequencies $\omega_1$ and $\omega_2$ should be, thus, equal to twice the propagation constant of the guided mode of pump radiation. This relation indicates the possibility to achieve phase matching for the whole family of nonlinear-optical parametric processes, resulting in the generation of new spectral components. Geometrically, it is clear that one possible solution to this problem is a dispersion profile with the frequency of zero group-velocity dispersion (corresponding to the inflection point in the spectral dependence of the guided-mode propagation constant) lying around the second harmonic of pump radiation. Guided modes with such a dispersion would simultaneously phase-match third-harmonic generation and the wave-mixing process leading to the generation of spectral components with frequencies $\omega_1$ and $\omega_2$ lying bilaterally about the second harmonic of pump radiation.

Femtosecond pulses of 1.25-μm Cr:forsterite-laser radiation were employed as a pump in our experiments. The dispersion profile of a tapered fiber with a taper-waist diameter equal to 2 μm (the dotted line in Fig. 1) features zero group-velocity dispersion around 700 nm and is ideally suited for the double phase matching of the above-specified cascaded nonlinear-optical processes.

The laser system employed in our experiments (Fig. 2a) consisted of a $Cr^{4+}$: forsterite master oscillator, a stretcher, an optical isolator, a regenerative amplifier, and a compressor. The master oscillator, pumped with a fiber Nd:YAG laser, generated 30–50-fs light pulses with a repetition rate of 120 MHz. The central wavelength of this laser radiation was 1250 nm with a bandwidth of 26 nm (Fig. 2b) and a mean power of about 180 mW.

Horizontally polarized 30–50 fs pulses (Fig. 2c) were then stretched up to 700 ps in a grating stretcher (Fig. 2). Upon passing through a Faraday isolator and a λ/4 plate, the light pulses became vertically polarized. These pulses were then transmitted through a broadband polarizer to be injected in the regenerative amplifier at the moment of time corresponding to maximum population inversion, created by pump pulses with a repetition rate of 1 kHz. A switch was used to set a horizontal polarization of pulses injected into the cavity of the amplifier. An amplified pulse with an energy of

100 μJ was coupled out of the amplifier through the switch, triggered at the moment of time corresponding to optimal amplification. Radiation coming out of the amplifier was vertically polarized again. The amplified pulse was returned to the isolator along the same optical path. Radiation passing through the isolator in the backward direction experienced no change in its polarization, since polarization rotations introduced by the $\lambda/4$ plate and the Faraday isolator compensate for each other. The pulses coupled out of the isolator through the broadband polarizer were transmitted through a $\lambda/2$ plate and compressed to a 75-fs duration in a grating compressor. Approximately 50% of pulse energy was lost at this stage.

Radiation generated by the Cr:forsterite laser system was coupled into a tapered fiber fabricated from a standard telecommunication fiber (Corning SMF-28) with a core diameter of about 9 μm, cutoff wavelength of 1250 nm, and numerical aperture of 0.1. The technology of fiber tapering, described in detail in [13], involved drawing a heated fiber, leading to a decrease in the fiber cross-section area. Due to the small fiber diameter of the taper-waist region (Fig. 2) and the high refractive-index step from the fused silica core to the air cladding, laser radiation was strongly confined to the fiber core in the taper-waist region, enhancing nonlinear-optical processes. The tapered section of the fiber was placed in a dust-proof transparent plastic box. The length of the taper-waist region of the fiber was equal to 90 mm. Transition regions, connecting tapered and untapered fiber sections, had a length of 35 mm each. The core diameter in the taper-waist region for the fibers employed in our experiments was 2 μm. The group-velocity dispersion calculated for fiber taper-waist regions with different diameters as a function of the wavelength is presented in Fig. 1. The wavelength of fundamental radiation of the Cr:forsterite laser, as can be seen from Fig. 1, falls within the anomalous-dispersion area of a fiber with a 2-μm-diameter taper-waist region.

Pump radiation was delivered to the taper-waist region through a short section of untapered fiber with a length of about 1 cm. The beam of amplified $Cr^{4+}$:forsterite laser radiation was focused on the fiber end by an $8^\times$ objective with a numerical aperture of 0.2. We were able to vary the power of pump radiation within a broad range by changing the relative orientation of a polarizer and a polarization analyzer. The mean power of radiation in front of and behind the fiber was measured with a power meter. Up to 50% of laser radiation power was coupled into the fiber according to these measurements. A lens with a focal length of 10 mm collimated the beam coming out of the fiber. Radiation spatially dispersed by a spectrometer was then registered with an optical multichannel analyzer. The data read out from the analyzer were stored and processed by a computer.

Parameters of the tapered fiber employed in our experiments were chosen in such a way as to phase-match third-harmonic generation in one of the higher waveguide modes. Theoretical analysis of phase-matching conditions for third-harmonic generation in tapered and microstructure fibers extended to include the group delay of short light pulses was earlier performed in [17, 18]. Figure 3 displays the wavelength dependences of the phase mismatches for the generation of the third harmonic of 1.25-μm Cr:forsterite-laser radiation in different modes of the tapered fiber. These dependences indicate the possibility of achieving generalized phase matching (modified to include group-delay effects [17, 18]) for third-harmonic generation in higher modes of tapered fibers. This generalized phase matching, however, cannot be achieved for the third-harmonic generation process involving the fundamental modes of pump radiation and the third harmonic. The phase mismatch for this process is shown by the dash–dotted line in Fig. 3. Neither can phase matching be achieved with our fiber for the generation of the third harmonic in the $HE_{12}$ mode by the fundamental mode of the pump pulse (the dashed line in Fig. 3). However, the $HE_{13}$ mode of the third harmonic can be phase-matched with the fundamental mode of the pump pulse in the considered tapered fiber, as shown by the solid line in Fig. 3. Because of the group-velocity mismatch of the pump and third-harmonic pulses, phase matching is never achieved for the entire spectrum of the pump pulse. The spectrum of the third harmonic becomes asymmetric under these conditions. Such an asymmetry in the spectra of third-harmonic pulses was observed earlier in nonlinear experiments with microstructure [19] and tapered [18] fibers.

Tapered fibers with the parameters specified above provided a high efficiency of third-harmonic generation even when unamplified 30-fs pulses were used as a pump. The spectrum of the third harmonic featured a characteristic asymmetry (Fig. 3), related to group-delay effects. This result also agrees well with our theoretical predictions. The efficiency of third-harmonic generation with unamplified 30-fs Cr:forsterite-laser pulses, defined as the total energy of the third-harmonic pulse measured at the output of the fiber to the total energy of the fundamental pulse, was estimated as 0.05% under our experimental conditions. However, the efficiency of third-harmonic generation inside the fiber was much higher even in experiments with unamplified pulses of fundamental radiation. Since this study was mainly aimed at creating fibers for a cascaded generation of multiple spectral components, our fibers were not optimized for a maximum output of third-harmonic radiation generated in higher order guided modes. Much of the third-harmonic energy was lost in our experiments, because the cutoff wavelength of our fibers was, perhaps, too short for the $HE_{13}$ mode to be guided at the third-harmonic wavelength and because of strong mode coupling in the conical transition regions of the tapered fiber.
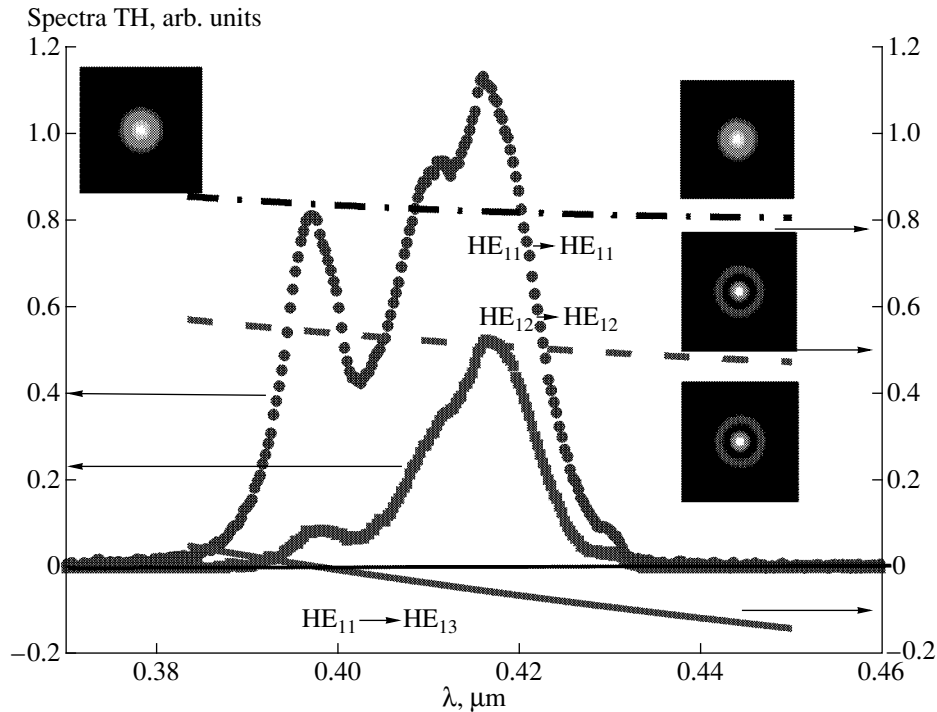
**Fig. 3.** Experimental spectra of the third harmonic produced in a tapered fiber by pulses of 1.25-μm Cr:forsterite laser radiation with an initial duration of 30 fs. The energy of pump laser pulses is (solid curve) 0.24 nJ and (dotted line) 0.32 nJ. Also shown are the values of $\Delta\beta_{m1}$, the effective phase mismatch for the $HE_{11}$ mode of the pump pulse and the $HE_{1m}$ mode of the third harmonic, calculated for a fiber consisting of a fused silica core with a diameter of 2.6 μm and an air cladding: (dash–dotted curve) $m = 1$, (dashed curve) $m = 2$, and (solid curve) $m = 3$. The insets show transverse intensity distributions of light field in $HE_{1m}$ modes ($m = 1, 2, 3$) of the tapered fiber, illustrating the transformation of the spatial mode corresponding to the $HE_{11} \longrightarrow HE_{1m}$ third-harmonic generation process.

Third-harmonic radiation was then involved in a cascade of nonlinear-optical interactions, accompanying the propagation of femtosecond pulses in the tapered fiber. To study these processes, we employed amplified 75-fs pulses of Cr:forsterite-laser radiation with an energy of 10–200 nJ. Figure 4a displays the visible part of the spectrum of radiation coming out of the fiber. Along with the intense spectral component corresponding to the third harmonic of pump radiation, this spectrum features clearly resolved maxima centered around 550 and 720 nm, arising due to cascaded nonlinear-optical processes. Generation of the 720-nm signal, observed in our experiments, can be qualitatively explained in terms of the results of numerical simulations [20] performed for cascaded four-wave mixing processes in microstructure fibers induced by a short pump pulse with a wavelength lying in the range of anomalous dispersion. The spectral component centered at 550 nm can be then attributed to a cascaded parametric interaction, with the frequency of this component, $\omega_2$, satisfying the relation $\omega_2 + \omega_1 = \omega_0 + 3\omega_0$, where $\omega_0$ is the frequency of pump radiation (the fundamental frequency of Cr:forsterite-laser radiation) and $\omega_1$ is the frequency of the 720-nm spectral component. The dispersion profile of our tapered fiber provided phase matching for this parametric process. Signals at

550 and 720 nm are, thus, produced through a doubly phase-matched cascaded parametric process involving third-harmonic generation as the first stage. As can be seen from the spectrum presented in Fig. 4a, the intensities of the 550- and 720-nm spectral components are comparable with the intensity of the third harmonic. The maximum efficiency of pump-radiation energy conversion into these spectral components achieved with 75-fs pump pulses having an energy of 200 nJ is estimated as approximately 4%.

The propagation of amplified femtosecond pulses with energies of 10–200 nJ in a tapered fiber with the parameters specified above is also accompanied by a transformation of the long-wavelength part of their spectra (Fig. 4b). As the energy of laser pulses increases, effects related to stimulated Raman scattering and soliton frequency shifts [20–22] become more and more efficient, leading to the growth in the intensity of long-wavelength spectral components. As can be seen from the results of experimental studies presented in Fig. 4b, the infrared part of the spectrum of output radiation stretches to the range of wavelengths exceeding 1600 nm. These experimental findings indicate that tapered-fiber-based components for the spectral transformation of ultrashort light pulses substantially expand the capabilities of femtosecond Cr:forsterite
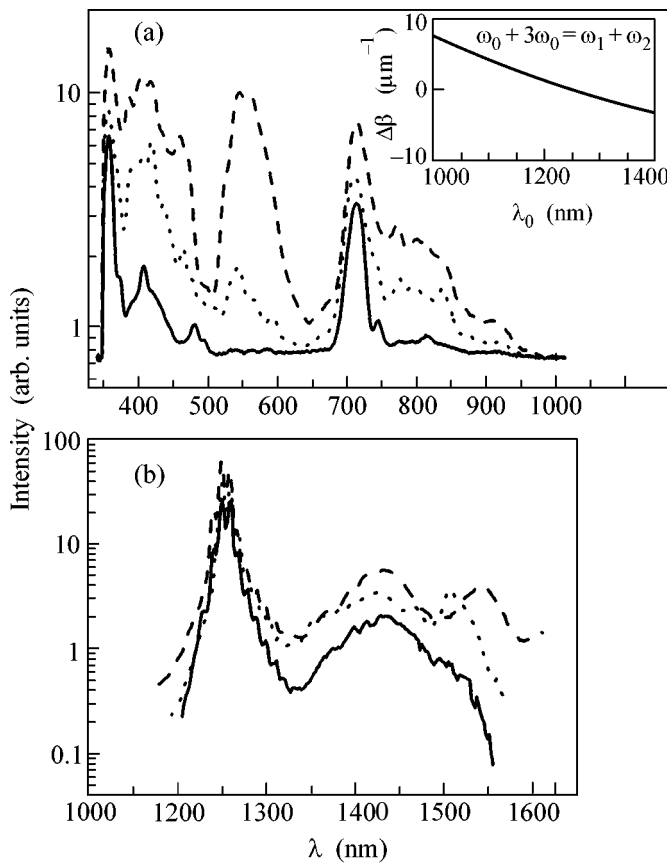
**Fig. 4.** Spectra of radiation at the output of a tapered fiber with a taper-waist diameter of 2 μm measured in the wavelength ranges of (a) 350–950 nm and (b) 1200–1600 nm. The energy of 75-fs Cr:forsterite-laser pulses coupled into the fiber is (solid line) 100 nJ, (dotted line) 150 nJ, and (dashed line) 200 nJ. The inset in Fig. 4a shows the mismatch of propagation constants $\Delta\beta$ for the waveguide modes involved in the parametric wave-mixing process $\omega_2 + \omega_1 = \omega_0 + 3\omega_0$ in a tapered fiber with a taper-waist diameter of 2 μm as a function of the pump wavelength $\lambda_0$.

lasers for telecommunication technologies, infrared spectroscopy, and biomedical applications.

Thus, the results of our experiments presented in this paper demonstrate the possibility to doubly phase-match cascaded parametric wave mixing of femtosecond laser pulses in tapered fibers. Fibers with an appropriately tailored dispersion profile allowed us to simultaneously phase-match two types of nonlinear-optical processes—third-harmonic generation and parametric four-wave mixing involving the third-harmonic pulse. Doubly phase-matched cascaded parametric interactions of ultrashort light pulses lead to the generation of a manifold of new spectral components, substantially expanding the capabilities of the available laser sources of ultrashort pulses for the solution of a broad class of fundamental and applied problems in spectroscopy, telecommunication technologies, coherent and quantum control, accessing the absolute phase of ultrashort pulses, optical metrology, and biomedicine.

## REFERENCES

1. S. A. Akhmanov and R. V. Khokhlov, *Nonlinear Optics* (VINITI, Moscow, 1964; Gordon and Breach, New York, 1972).
2. N. Bloembergen, *Nonlinear Optics* (Benjamin, New York, 1965; Mir, Moscow, 1966).
3. R. B. Miles and S. E. Harris, IEEE J. Quantum Electron. **9**, 470 (1973).
4. J. A. Armstrong, N. Bloembergen, J. Ducuing, and P. S. Pershan, Phys. Rev. **127**, 1918 (1962).
5. M. M. Fejer, G. A. Magel, D. H. Jundt, and R. L. Byer, IEEE J. Quantum Electron. **28**, 2631 (1992).
6. A. Fiore, V. Berger, E. Rosencher, *et al.*, Nature **391**, 463 (1998).
7. L. A. Golovan, V. Yu. Timoshenko, A. B. Fedotov, *et al.*, Appl. Phys. B **73**, 31 (2001).
8. G. D'Aguanno, M. Centini, M. Scalora, *et al.*, Phys. Rev. E **64**, 016609 (2001).
9. P. K. Kashkarov, L. A. Golovan, A. B. Fedotov, *et al.*, J. Opt. Soc. Am. B **19**, 2273 (2002).
10. G. P. Agrawal, *Nonlinear Fiber Optics* (Academic, Boston, 1989; Mir, Moscow, 1996).
11. J. C. Knight, T. A. Birks, P. St. J. Russell, and D. M. Atkin, Opt. Lett. **21**, 1547 (1996).
12. A. M. Zheltikov, Usp. Fiz. Nauk **170**, 1203 (2000) [Phys. Usp. **43**, 1125 (2000)].
13. T. A. Birks, W. J. Wadsworth, and P. St. J. Russell, Opt. Lett. **25**, 1415 (2000).
14. D. A. Akimov, A. A. Ivanov, M. V. Alfimov, *et al.*, Appl. Phys. B **74**, 307 (2002).
15. Special issue of the J. Opt. Soc. Am. B **19** (9) (2002), Ed. by C. M. Bowden and A. M. Zheltikov.
16. N. G. R. Broderick, G. W. Ross, H. L. Offerhaus, *et al.*, Phys. Rev. Lett. **84**, 4345 (2000).
17. A. N. Naumov and A. M. Zheltikov, Opt. Express **10**, 122 (2002).
18. D. A. Akimov, A. A. Ivanov, A. N. Naumov, *et al.*, Appl. Phys. B (in press).
19. A. N. Naumov, A. B. Fedotov, A. M. Zheltikov, *et al.*, J. Opt. Soc. Am. B **19**, 2183 (2002).
20. A. V. Husakou and J. Herrmann, J. Opt. Soc. Am. B **19**, 2171 (2002).
21. S. Coen, A. Hing Lun Chau, R. Leonhardt, *et al.*, J. Opt. Soc. Am. B **19**, 753 (2002).
22. J. Herrmann, U. Griebner, N. Zhavoronkov, *et al.*, Phys. Rev. Lett. **88**, 173901 (2002).

*Translated by A. Zheltikov*